Design Methodology and Materials for Additive Manufacturing of Magnetic Components

Yi Yan

Dissertation submitted to the faculty of the Virginia Polytechnic Institute and State University in partial fulfillment of the requirement for the degree of

Doctor of Philosophy

in

Materials Science and Engineering

Guo-Quan Lu, Chair

Khai D. T. Ngo

Louis J. Guido

Alex O. Aning

William T. Reynolds

March 22nd, 2017

Blacksburg, VA

Keywords: Design methodology, additive manufacturing, low-temperature curable, magnetic components, magnetic paste, nanosilver paste, power electronics integration

Design Methodology and Materials for Additive Manufacturing of Magnetic Components

Yi Yan

ABSTRACT

Magnetic components such as inductors and transformers are generally the largest circuit elements in switch-mode power systems for controlling and processing electrical energy. To meet the demands of higher conversion efficiency and power density, there is a growing need to simplify the process of fabricating magnetics for better integration with other power electronics components. The potential benefits of additive manufacturing (AM), or more commonly known as three-dimensional (3D) printing technologies, include shorter lead times, mass customization, reduced parts count, more complex shapes, less material waste, and lower life-cycle energy usage—all of which are needed for manufacturing power magnetics. In this work, an AM technology for fabricating and integrating magnetic components, including the design of manufacturing methodology and the development of the feedstock material, was investigated.

A process flow chart of additive manufacturing functional multi-material parts was developed and applied for the fabrication of magnetic components. One of the barriers preventing the application of 3D-printing in power magnetics manufacturing is the lack of compatible and efficient magnetic materials for the printer's feedstock. In this work, several magnetic-filled-benzocyclobutene (BCB) pastes curable below 250^{o}C were formulated for a commercial multi-material extrusion-based 3D-printer to form the core part. Two magnetic fillers were used: round-shaped particles of permalloy, and flake-shaped particles of Metglas 2750M. To guide the formulation, 3D finite-element models of the composite, consisting of periodic unit cells of magnetic particles and flakes in the polymer-matrix, was constructed. Ansoft Maxwell was used to simulate magnetic properties of the composite. Based on the simulation results, the pastes consisted of 10 wt% of BCB and 90 wt% of magnetic fillers—the latter containing varying amounts of Metglas

from 0 to 12.5 wt%. All the pastes displayed shear thinning behavior and were shown to be compatible with the AM platform. However, the viscoelastic behavior of the pastes did not exhibit solid-like behavior, instead requiring layer-by-layer drying to form a thick structure during printing. The key properties of the cured magnetic pastes were characterized. For example, bulk DC electrical resistivity approached 10^7 Ω·cm, and the relative permeability increased with Metglas addition, reaching a value of 26 at 12.5 wt%. However, the core loss data at 1 MHz and 5 MHz showed that the addition of Metglas flakes also increased core loss density.

To demonstrate the feasibility of fabricating magnetic components via 3D-printing, several inductors of differing structural complexities (planar, toroid, and constant-flux inductors) were designed. An AM process for fabricating magnetic components by using as-prepared magnetic paste and a commercial nanosilver paste was developed and optimized. The properties of as-fabricated magnetic components, including inductance and DC winding resistance, were characterized to prove the feasibility of fabricating magnetic components via 3D-printing. The microstructures of the 3D-printed magnetic components were characterized by Scanning-electron-microscope (SEM). Results indicate that both the winding and core magnetic properties could be improved by adjusting the formulation and flow characteristics of the feed paste, by fine-tuning printer parameters (e.g., motor speed, extrusion rate, and nozzle size), and by updating the curing profile in the post-process.

The main contributions of this study are listed below:

1. Developed a process flow chart for additive manufacturing of functional multi-material components. This methodology can be used as a general reference in any other research area targeting the utilization of AM technology.

2. Designed, formulated and characterized low-temperature curable magnetic pastes. The pastes are physically compatible with the additive manufacturing platform and have applications in the area of power electronics integration.

3. Provided an enhanced understanding of the core-loss mechanisms of soft magnetic materials and soft magnetic composites at high frequency applications.

Design Methodology and Materials for Additive Manufacturing of Magnetic Components

Yi Yan

GENERAL AUDIENCE ABSTRACT

Magnetic components such as inductors and transformers are typically the largest circuit elements in switch-mode power systems for controlling and processing electrical energy. To meet the demands of higher conversion efficiency and power density, there is a growing need to simplify the process of fabricating magnetics for better integration with other power electronics components. The potential benefits of additive manufacturing (AM), or more commonly known as three-dimensional (3D) printing, include shorter lead times, mass customization, reduced parts count, more complex shapes, less material waste, and lower life-cycle energy usage—all of which are needed for manufacturing power magnetics. In this work, an AM technology for fabricating and integrating magnetic components, including the design of manufacturing methodology and the development of the feedstock material, was investigated.

A process flow chart of additive manufacturing functional multi-material parts was developed and applied for the fabrication of magnetic components. One of the barriers preventing the application of 3D-printing in power magnetics manufacturing is the lack of compatible and efficient magnetic materials for the printer's feedstock. Therefore, several magnetic-filled-benzocyclobutene (BCB) pastes were formulated and characterized for a commercial multi-material extrusion-based 3D-printer to form the core parts.

To demonstrate the feasibility of fabricating magnetic components via 3D-printing, several inductors of differing structural complexities were designed. An AM process for fabricating magnetic components by using as-prepared magnetic paste and a commercial nanosilver paste was developed and optimized. Results indicate that both the winding and core magnetic properties could be improved by adjusting the formulation and flow characteristics of the feed paste, by fine-tuning printer parameters, and by updating the curing profile in the post-process.

ACKNOWLEDGEMENTS

This work is supported by National Science Foundation (NSF) (under Grants No. 1231965 and No. 1507314), Texas Instruments, Institute for Critical Technology and Applied Science (ICTAS) and the High-Density Integration (HDI) mini-consortium of the Center for Power Electronics Systems (CPES) at Virginia Tech.

It is an honor for me to express my utmost gratitude to my advisor, Dr. Guo-Quan Lu. His incredible depth of knowledge, coupled with his rigorous approach to research, inspired me throughout my PhD study and will continue to motivate me in the future.

I am very grateful to my other committee members, Dr. Khai D.T. Ngo, Dr. Louis J. Guido, Dr. Alex O. Aning, and Dr. William Reynolds, for serving on my committee and offering their valuable advice and guidance.

My very special thanks goes to Karl Gifford and all the other colleagues who work at the Hyrel 3D company for their great suggestions and technical support on operating the 3D printer.

I am also very grateful to my fellow students and other colleagues: Dr. Yiying Yao, Dr. David Berry, Dr. Kewei Xiao, Dr. Hanguang Zheng, Dr. Zhemin Zhang, Li Jiang, Han Cui, Weizhen Sun, Shan Gao, Jacob Monzel, Robert Acken, Ting Ge, Lanbing Liu, Chao Ding, Shengchang Lu, Kaidi Yan (and many others), for their useful suggestions, friendship, encouragement, and help.

Finally, I am sincerely grateful to my parents. They have always unconditionally supported and encouraged me with their best wishes. Thank you, both, for your endless affection and patience throughout these many years.

Table of Contents

LIST OF FIGURES

LIST OF TABLES

CHAPTER 1. INTRODUCTION

1.1. Background

1.1.1. Developing trends of power electronics integration

The evolution of power electronic systems is being increasingly driven by the need for higher overall efficiency, higher power density, and smaller size [1-7]. The growing industrial importance of these factors has spurred the development of a variety of converters. Consider, for example, the widely-used point-of-load (POL) converter. Increasingly high-power density demands, coupled with the limited real estate of the motherboard, reinforce the importance of making these converters significantly smaller than in the past [8]. Fig. 1-1 shows the power density of today's POL products as a function of output current [9]. The integrated POLs illustrated in this figure can achieve 700-1000 W/in^3 power density—but with considerably less current (< 5A) than capsulated and discrete POLs. The power density of the POL is reduced as the current increases, which occurs because the core size of the inductor in a POL product must be very bulky to store the significant level of energy needed for high-current applications. Furthermore, the large inductor current also requires large winding to reduce winding loss. As indicated in Fig. 1-1, the passive components—and especially the magnetic components—occupy a considerable footprint on the motherboard of the POLs for high-current applications. Generally speaking, the bulky and high-profile magnetic components prevent further successful integration of power electronics systems [9, 10].

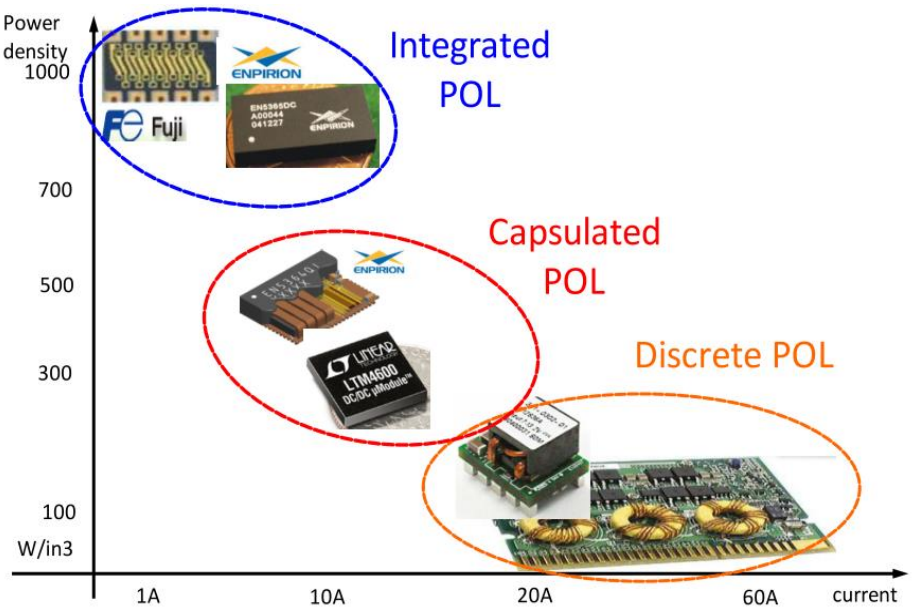

Fig. 1-1. Power density of today's POL products as a function of output current[9].

1.1.2. Integration of magnetic components in power electronics

Magnetic components such as inductors and transformers are used in power conversion for filtering and energy storage/transfer in many of today's dc/dc converters, which are typically the largest components. Indeed, it is not uncommon for the magnetic parts to occupy more than 50% of a product's total volume. Several of these components can be seen in a state-of-the-art power supply shown in Fig. 1-2. Therefore, a way of integrating smaller magnetic components into devices, while still enabling high power density and high efficiency power electronics, remains a goal of scientists and engineers.

Typically, to increase the integration capability of magnetic devices and achieve high-power density in a given power electronics system, two things have to happen simultaneously [10, 11]. The first is a significant increase in the switching frequency to reduce the size and weight of the magnetics, and the second is to integrate the magnetics with active components to realize the needed power density. For current semiconductor

technology, very fast devices are available. For example, wide-band-gap (WBG) devices (SiC and GaN) can be switched at high frequency up to tens of megahertz [12-16]. However, the limiting factor is the packaging technology.

Currently, the packaging technology associated with power electronic converters is based on assembling pre-manufactured discrete components. The power semiconductor devices, capacitors, inductors, and transformers are manufactured as discrete components and then connected to the circuit board. Nowadays, magnetic cores and electrical conductor windings that make up magnetic components are fabricated separately in multiple, complex steps. Furthermore, lengthy interconnections between the discrete components pose the risk of introducing parasitic electrical resistance, capacitance, and inductance that can cause detrimental electrical noise and inefficiency [17, 18]. This would be even more problematic if one wished to take advantage of WBG devices by switching them at higher frequencies [19]. In short, magnetic integration remains a challenge in the field of PE.

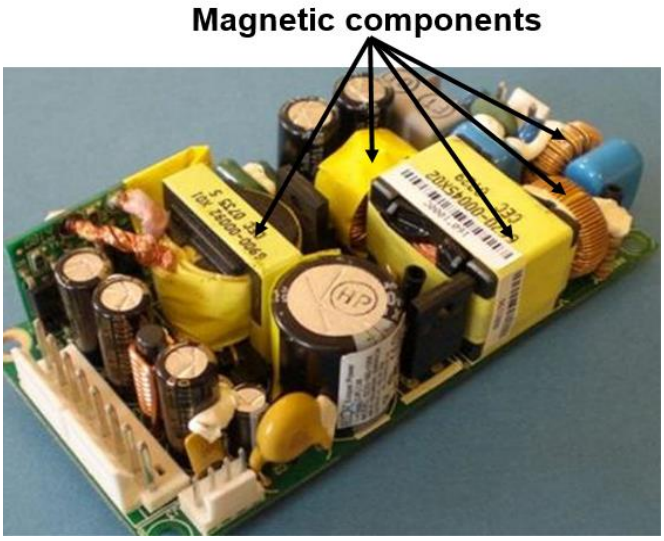

Fig. 1-2. Magnetic components occupying 30%-50% of a power supply.

1.2. Conventional manufacturing techniques for power magnetics

The choice of manufacturing method for magnetic components will have a significant impact on their integration modes. Conventional manufacturing techniques for high-frequency (tens of kilohertz to a few megahertz) power magnetics are reviewed in this section. The magnetic core for high frequency applications is commonly classified into three categories: iron-powdered cores, amorphous & nanocrystalline laminations, and soft ferrites. A survey of the literature revealed that traditional methods of fabricating these magnetic cores mainly involve subtractive methods or molding/casting processes. The state-of-the-art high-frequency magnetic materials and their specific fabrication techniques are discussed in detail in the following sections:

1.2.1. The state-of-the-art high-frequency magnetic materials

The ever-increasing demand for miniaturization in power transformers and inductors is heightening the need to develop magnetic core materials with low energy loss and high flux density, permeability, and operating frequency. Currently, the commercially available and widely used magnetic cores for high-frequency applications in industry are commonly classified into three categories: iron-powdered cores, amorphous & nanocrystalline laminations, and soft ferrites. These three categories of power magnetic materials feature distinct operational characteristics in different power electronics applications. Table 1-1 lists the properties and possible working frequency range for these three types of magnetic materials [20-22].

Table 1-1. Categories and properties of high-frequency application magnetic core materials.

Magnetic core materials	B_{sat} (T)	H_c (Oe)	μ_i	ρ (Ω•cm)	f (MHz)
Iron-powdered cores	0.75 – 1.5	0.003 – 0.35	~10^2 – 10^4	~10^{-5}	< 0.5
Amorphous & nanocrystalline laminates	0.75 – 0.9	0.007 – 0.03	~10^7	~10^{-4}	< 1
Soft ferrites	0.25 – 0.5	0.04 – 0.25	~10 – 10^3	~10^4 – 10^7	<10

Among all these materials, Fe-based powder cores and amorphous & nanocrystalline laminations, which exhibit high initial permeability and saturation magnetization, typically operate below 1 MHz because of high eddy current losses. In the megahertz frequency range, ferrites are often the top choice because of their low core loss density; for example, MnZn ferrites typically operate below 5 MHz, and the NiZn ferrite is essentially the only material that can be used at frequencies as high as 10 MHz. However, soft ferrites suffer from low saturation magnetization and rapidly decreasing permeability under DC bias.

In addition to these commercially available magnetic core materials, there are significant research efforts directed at developing new magnetic materials for high-frequency and integration applications. Based on the idea of reducing eddy-current loss in order to increase core resistivity, a number of new technologies have been developed. For example, cores fabricated from multilayer laminates of CoNiFe films separated by a metal-oxide insulating layer were prepared via electroplating, which were shown to have low eddy-current loss up to 10 MHz and high peak flux density up to 0.9 T [23]. Several researchers have used polymer resins to insulate and bond magnetic particles to form

magnetic-filled polymer matrix composites [24-27]. In another report, magnetic particles were embedded in oxide-insulating matrix phases to form CoZrO granular films [28]. Currently, however, the generalized process for making these high-resistive powder cores is typically quite complex, requiring either a long time (in the case of fabricating electroplated multilayer laminates) or high pressure (in the case of fabricating magnetic-polymer composites). In addition to complex fabricating processes, the high cost associated with these approaches represents another important factor that impedes the broader commercial applications of these newer magnetic materials. It must also be noted that the magnetic components come from the commercially available and low-cost core materials and electrical conductor windings have to be fabricated separately in multiple, complex steps.

1.2.2. Manufacturing techniques

The three broad categories of commercially available high-frequency magnetic core materials (iron-powdered cores, amorphous & nanocrystalline laminations, and soft ferrites) are typically fabricated by one of four main manufacturing techniques:

- **Powder Metallurgy (PM) —** Iron-powdered cores and soft ferrite cores are usually made by this method. PM has been recognized as a cost-effective method of producing high volumes of consistent parts for magnetic applications [29, 30]. PM offers distinct advantages that include high material utilization, precise material control, and the ability to produce relatively complex shapes. Fig. 1-3 illustrated a flow chart for the PM process. As shown in Fig. 1-3, the process involves introducing a powder premix to a die cavity, compacting the powder with a pressure of over 700-MPa [31, 32], ejecting the compact from the die, and sintering the compact at over 600^{o}C for iron-

based powder cores [33], and over 1000°C for MnZn or NiZn ferrite cores at atmospheric pressure and under a carefully controlled environment [34-37]. The premix generally consists of either a pure or pre-alloyed metal or ferrite powder, lubricants to facilitate compaction, and any additives to be alloyed during the sintering operation.

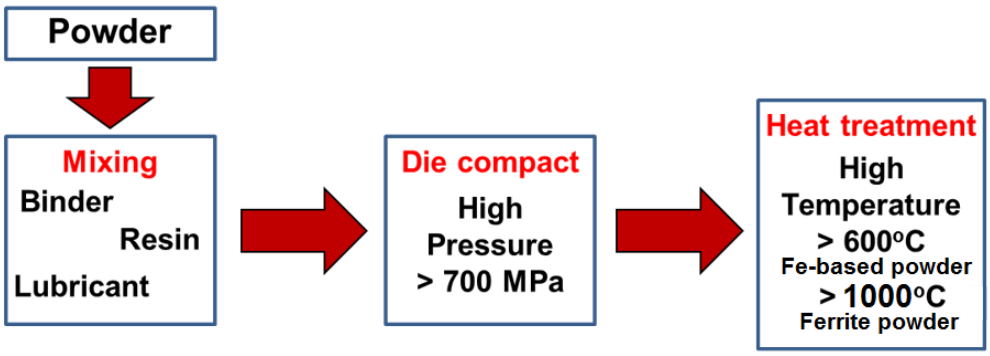

Fig. 1-3. Process flow chart of powder metallurgy process.

- **Metal Injection Molding (MIM) —** The MIM method is employed to make powder or soft ferrite cores into more complex structures [38]. Fig. 1-4 illustrates the flow chart of the MIM process. Specifically, this approach involves combining magnetic powders with binders to produce the "feedstock" mix that is injected as a liquid into a hollow mold using plastic injection molding machines. The "green part" is cooled and de-molded in the plastic molding machine. Next, a portion of the binder material is removed through the use of solvents, a thermal furnace, a catalytic process, or a combination of these methods. The resulting material is fragile and porous—in a condition known as the brown stage. The brown part is then sintered to form the high-density magnetic core. The powder used in the MIM process features an average particle size of less than 5 μm, which is much smaller in comparison to the analogous powder size used in the PM process [39]. Sintering in MIM is almost always performed

at high temperatures—namely, over 1350°C [40]. Therefore, higher densification and better homogeneity in the diffused state during sintering can be achieved due to the small powder size and high sintering temperature in the MIM process [41].

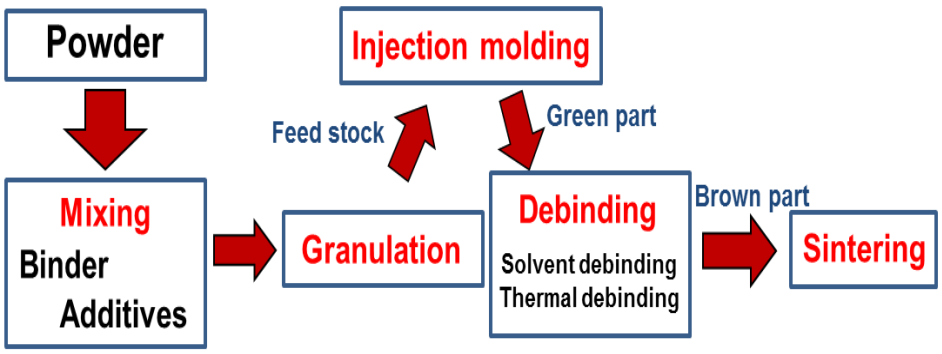

Fig. 1-4. Process flow chart of metal injection molding.

- **Low-temperature Co-fired Ceramic (LTCC) Technology —** The LTCC ferrites are fabricated according to a well-described method [42-44]. A LTCC ferrite material is actually NiCuZn ferrite particles mixed with binders to form a ferrite slurry. The slurry is screen printed on a tape through the use of a blade to form the thin flexible LTCC tape. The LTCC tape functions as the base material for the LTCC system. The material system includes physically and chemically compatible dielectric materials and conductor materials, which can be stacked together in various shapes, pressed, and then co-fired in an oven to create a hard ferrite structure. Compared with traditional ferrite materials such as either MnZn or NiZn ferrite, LTCC ferrite can be sintered at temperatures lower than 900°C with almost the same permeability and core loss density; however, it has much more flexibility for building integrated magnetic components on the PE circuits [45-47]. Fig. 1-5 shows the schematic of the LTCC process.

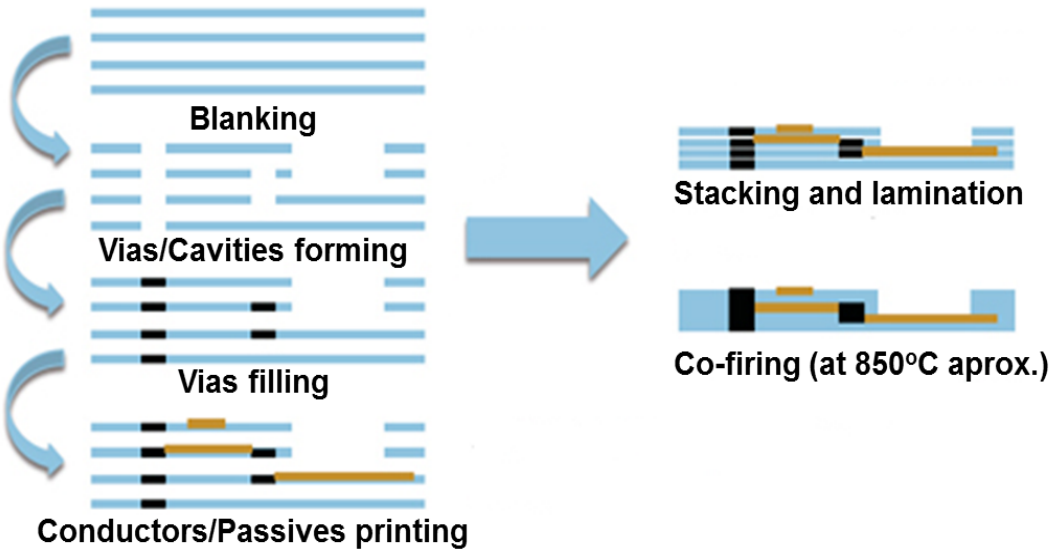

Fig. 1-5. Schematic of low temperature co-fired ceramic process.

- **Rapidly Quenched Technology —** Amorphous & nanocrystalline laminations are fabricated somewhat differently—principally because amorphous metals do not have the same crystalline structure as other magnetic materials [48, 49]. Specifically, all the atoms in an amorphous metal are randomly arranged. This unique microstructure makes the electrical resistivity of amorphous metals three or four times higher than those of conventional iron or iron-nickel alloys. Additionally, the magnetic loss of amorphous metals tends to be lower than other known crystalline alloys, making them good candidate core materials for incorporation in inductors or transforms that are intended for use in a power converter system operating at high frequency.

  The amorphous metallic alloys are made by a variety of techniques—all of which involve the rapid solidification of the alloying constituents from the gas or liquid phases. Fig. 1-6 shows that the amorphous alloys are prepared by cooling the liquid configuration at about million degrees per second. This extremely rapid cooling essentially prevents the atoms from rearranging into a stable crystalline form. As a

result, a metastable amorphous structure forms. Because of the absence of a distinct crystalline structure, amorphous alloys are magnetically soft. Usually, an amorphous metallic strip is formed with a thickness of approximately 20μm. Annealing amorphous alloys can form nanocrystalline alloys. The annealing temperatures for forming the nanocrystalline alloys typically ranges from 500 to 600°C [50, 51].

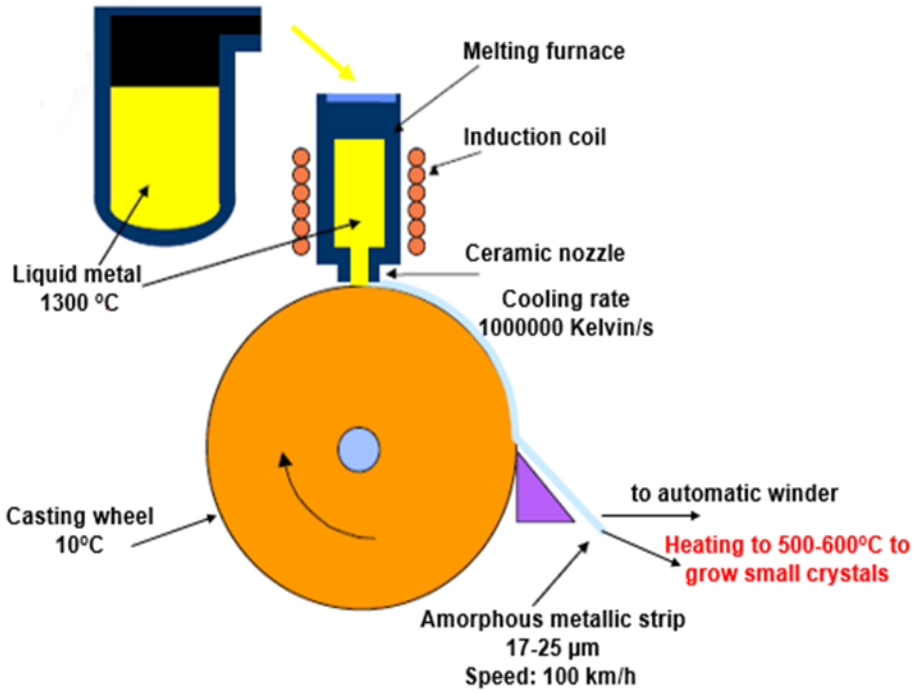

Fig. 1-6. Schematic of rapidly quenched process.

After the magnetic cores are fabricated via the above-mentioned techniques, there are three conventional methods for combining the magnetic core and the winding to form inductors or transformers: (1) conventional wire wound technology, which shown in Fig. 1-7 (a) [52]; (2) flexible printed circuit winding inserted in the planar cores, illustrated in Fig. 1-7 (b) [53]; and (3) embedding the core into the PCB winding, as shown in Fig. 1-7 (c) [54].

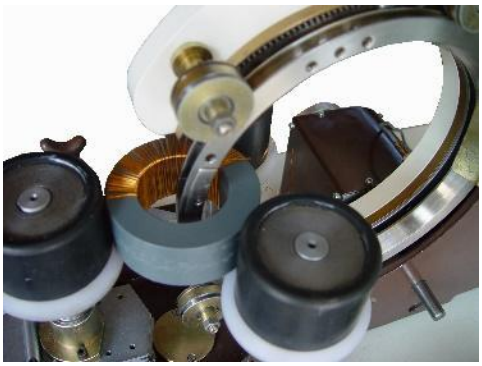

(a)

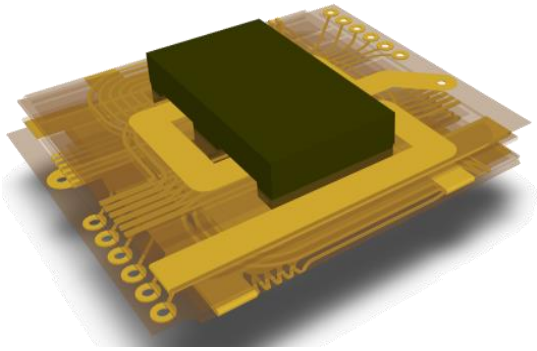

(b)

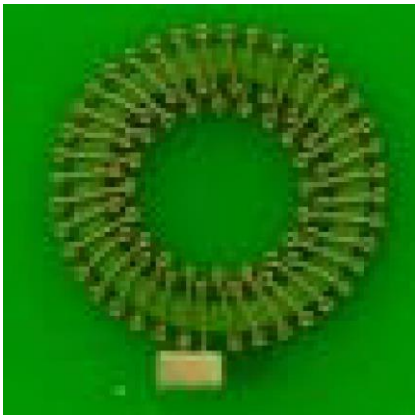

(c)

Fig. 1-7. Examples of magnetic components with different types of winding: (a) wire wound toroid core; (b) planar core with flexible printed circuit winding; (c) magnetic core embedded in PCB winding.

The drawback of each of these manufacturing approaches for combining discrete magnetic cores and windings is that they give rise to bulky and discrete components, which reinforces the need to design magnetic components more innovatively [55, 56]. As shown in Fig. 1-8, design approaches can be optimized to efficiently use magnetic materials in order to reduce their size. For example, the "constant-flux" inductor shown in Fig. 1-8 (a) is configured with spiral windings embedded in the magnetic core; this design approach requires precise control of the different widths, combined with consistent spacing between each turn of the spiral, to generate uniform flux in the core and thus increase power density [57]. Importantly, an inductor designed in this way can be two times lower in height

compared to conventional products. In Fig. 1-8 (b) [58], all of the winding posts are buried in the magnetic core, thereby generating more uniform flux and ultimately increased efficiency. Fig. 1-8 (c) shows the design of an over-molded inductor, whereby the magnetic material serves as both the inductor and the encapsulant. Unfortunately, the intricate configurations and geometries of these inductors pose challenges in fabricating them using conventional approaches.

In contrast, these novel structures can be easily fabricated via the additive manufacturing (AM) process using some non-functional materials such as plastic materials or alumina powders. Thus, to improve power conversion efficiency and the power density of a PE system, there is a need for manufacturing technologies that enable ease of fabrication and the straightforward integration of magnetic components.

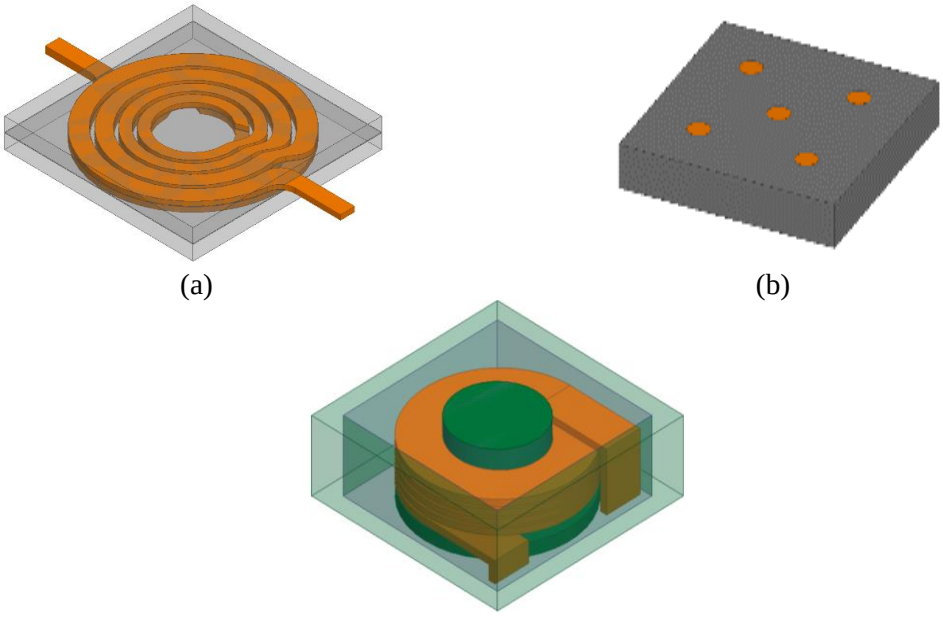

Fig. 1-8. Innovative magnetic designs for power density improvement: (a) constant-flux inductor; (b) five-phase integrated inductor; (c) over-molded inductor.

1.3. Overview of additive manufacturing technologies

Additive manufacturing or three-dimensional (3D) printing is a layer-by-layer process of making products from a digital model [59]. AM technologies were originally developed to work with polymeric materials, waxes, and paper laminates in order to create visualization models for products as they were being developed, since models can be much more helpful than drawings or renderings in fully understanding the intent of the designer when presenting a conceptual design. Thus, the AM technology can also be viewed as a "rapid prototyping" process at the onset of a project [60]. Following this initial purpose of simple model making, additive manufacturing has evolved over time as materials, manufacturing accuracy, and the overall quality of the output have improved. Today, AM is being used with more functional materials, including composites, metals, and ceramics. Moreover, the accuracy of the formed models has significantly improved so much so that results are being built into tolerance parameters required for assembly purposes. Therefore, improvements in the quality of the output, coupled with improved material properties from the AM technologies, signifies a much closer link to the final product. In recent years, the development of innovative, advanced AM techniques has significantly progressed, with more and more categories of 3D printers based-on different AM technologies coming out, thereby yielding increasingly enhanced industry applications [61].

1.3.1. Categories of additive manufacturing technologies

There are numerous ways to classify AM technologies [62] —for example, according to the type of raw material input. Using this parameter, AM technologies can be divided into six categories.

- **Liquid Polymer Systems —** The first commercial 3D-printing system to be invented was the liquid photopolymer system [63, 64]. Specifically, stereolithography (STL) is the term used to describe AM when liquid polymer systems are utilized to create 3D-objects. The schematic of the system is shown in Fig. 1-9. This process uses liquid photopolymer resin as the printing material and only can print one material at a time. Subsequently, this 3D-printing system uses UV light to cure the resin layer-by-layer, as the platform submerges itself deeper in the printing chamber until the design is completed. The uncured resin offers support to maintain the shape of the printing object, after which the liquid polymer is drained from the vat, leaving the solid model behind.

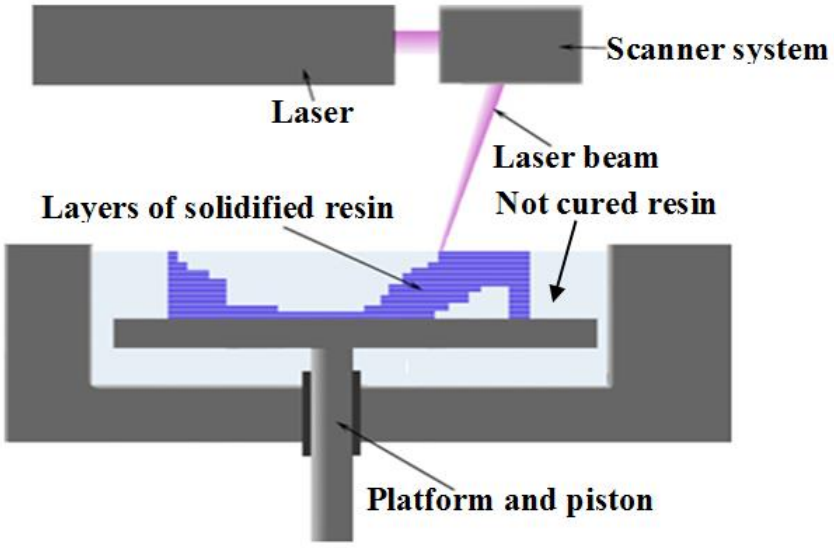

Fig. 1-9. Schematic of liquid photopolymer system.

- **Discrete Particle Systems —** This technique applies a binder, glue, or laser to a powder bed to provide an adhesive force between powder particles when printing layer-by-layer [65-68]. The primary limitation of this approach is that it can only process one material at a time. Several types of 3D printers belong to this system. For example, the

schematic shown in Fig. 1-10 illustrates the printing process for a binder jetting 3D printer, which belongs to the discrete powder system. The binder jetting machine will distribute a layer of powder onto a build platform, after which a liquid bonding agent is applied through inkjet print heads that bonds the particles together. The build platform is then lowered and the next layer of powder is applied on top. By repeating the process of laying out powder and bonding, the parts are built up in the powder bed. This process does not require any support structures, and the discrete powder system can work with almost any material that is available in powder form.

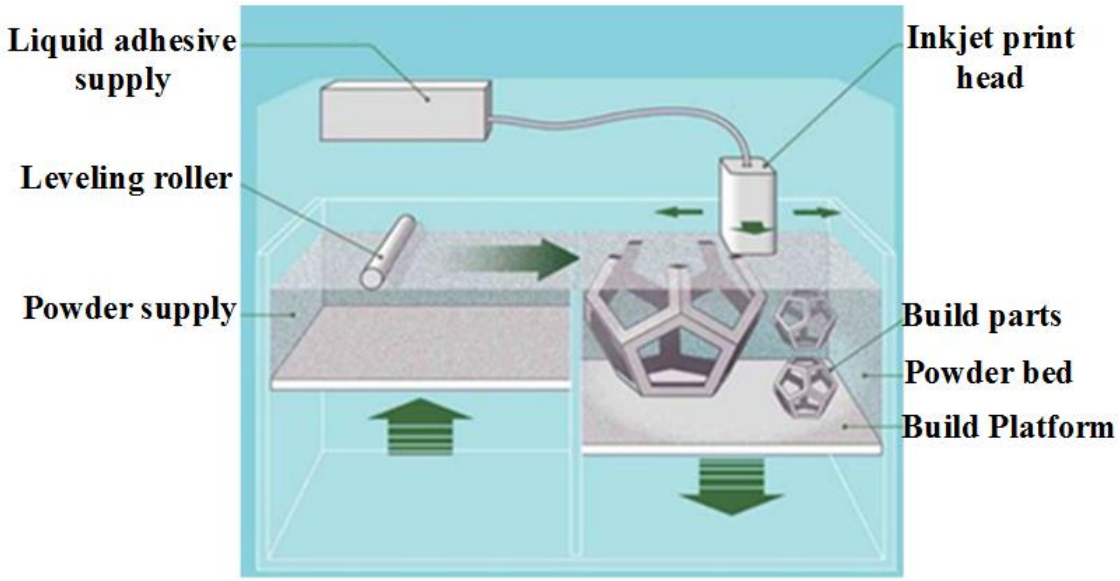

Fig. 1-10. Schematic of binder jetting system.

- **Solid Sheet Systems —** The solid sheet system is one of the earlier AM technologies to be developed, and was originally known as the Laminated Object Manufacturing (LOM) system from Helisys, USA [69]. The schematic of the sheet lamination process is shown in Fig. 1-11. This technology uses a laser to cut out profiles from sheet paper or metal that is delivered from a continuous roll, which form the layers of the final

product. Layers are bonded together using a heat-activated resin that is coated on one surface of the paper or metal. A hatch pattern cut into the excess material allows the user to separate away waste material and reveal the part [70]. It must be noted that this system can only process one material at a time [71].

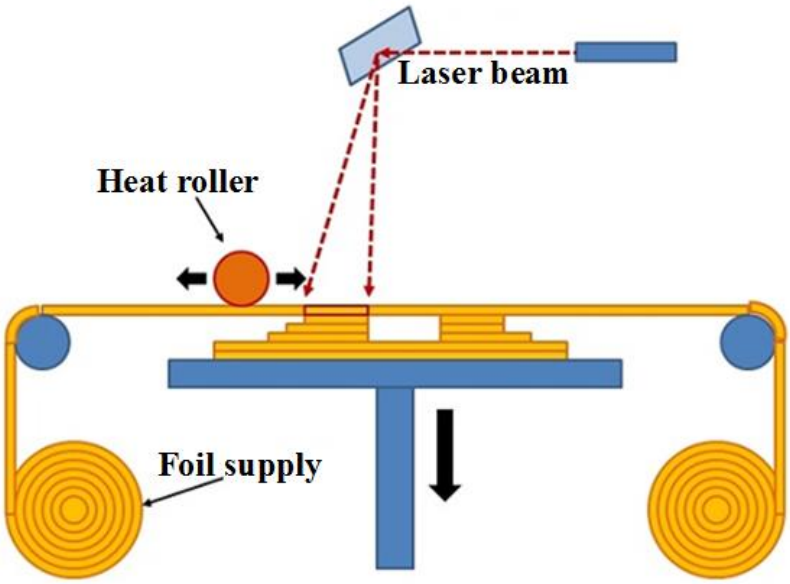

Fig. 1-11. Schematic of sheet lamination system.

- **Ink Material Systems —** The ink material system is able to directly print material structures, typically utilizing a UV curable ink [72-74]. The schematic of this system is shown in Fig. 1-12. This system is capable of combining different print materials within the same 3D-print model. Multiple print heads apply the material simultaneously to create each layer, followed by exposure to UV light to cure the layer. These layers build up one at a time in an additive process to create a 3D model. Fully cured models can be handled and used immediately without additional post-curing. Along with the selected model materials, a gel-like support material facilitates successful printing of complicated geometries. Support material can be removed by hand or through the use

of a high-powered water jet system.

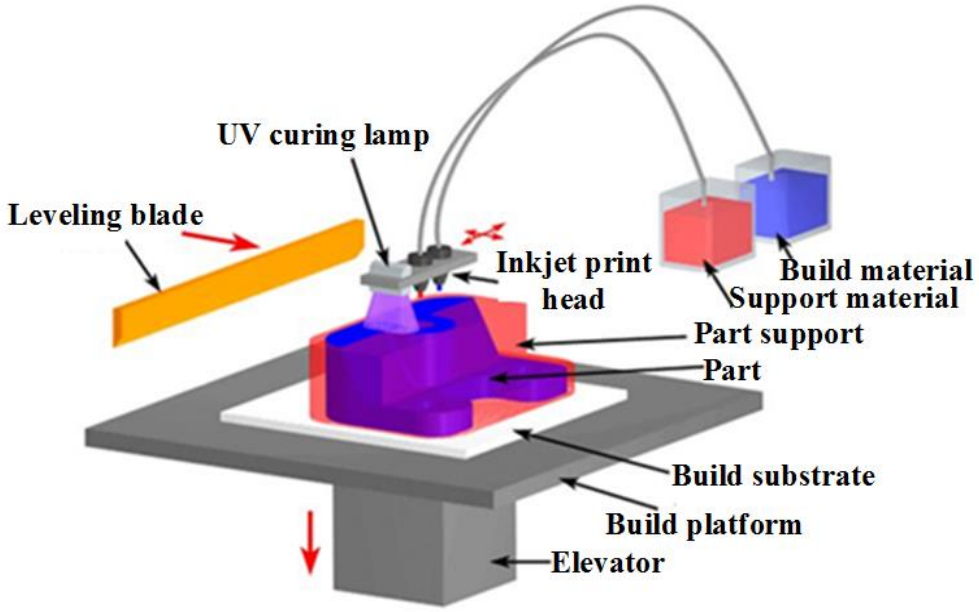

Fig. 1-12. Schematic of ink jetting system.

- **Molten Material Systems —** Molten material systems are defined by the use of a pre-heating chamber that raises the material temperature to melting point so that it can flow through a delivery system [75]. The most well-known method for accomplishing this process is through the use of the Fused Deposition Modeling (FDM) system developed by Stratasys [76]. A schematic of the system is shown in Fig. 1-13. This approach uses an extrusion technique to deliver the material through a nozzle in a controlled manner. Two extrusion heads are often used so that support structures can be fabricated from a different material to facilitate the cleaning and removal of structures [77].

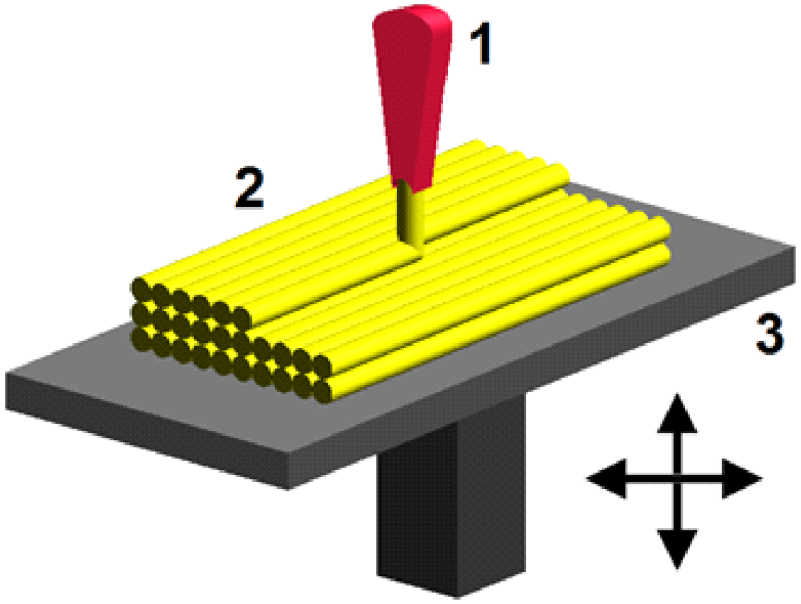

Fig. 1-13. Fused deposition modeling system: (1) nozzle ejecting molten material; (2) deposited material (modeled part); (3) controlled movable table.

- **Paste Material Systems —** The paste material system is another type of extrusion technique. The deposition of material in this system is syringe-based, which can extrude both high- and low-viscosity materials [78, 79]. A schematic of this paste material system is shown in Fig. 1-14. Syringe-based printers extrude material through a tip attached to a syringe barrel, where the pressure on the piston can be controlled. Examples of materials printed with this type of printer are very flexible—for example, silicones, biomaterials including cells, edible frosting, and conductive polymers can all be feed materials [80, 81]. An object composed of several types of materials can be constructed during a single printing run by simultaneously using multiple syringe barrels. The resolution of the printing mechanism depends on the nozzle size, the printed material properties, and the accuracy and resolution of the stepper motors.

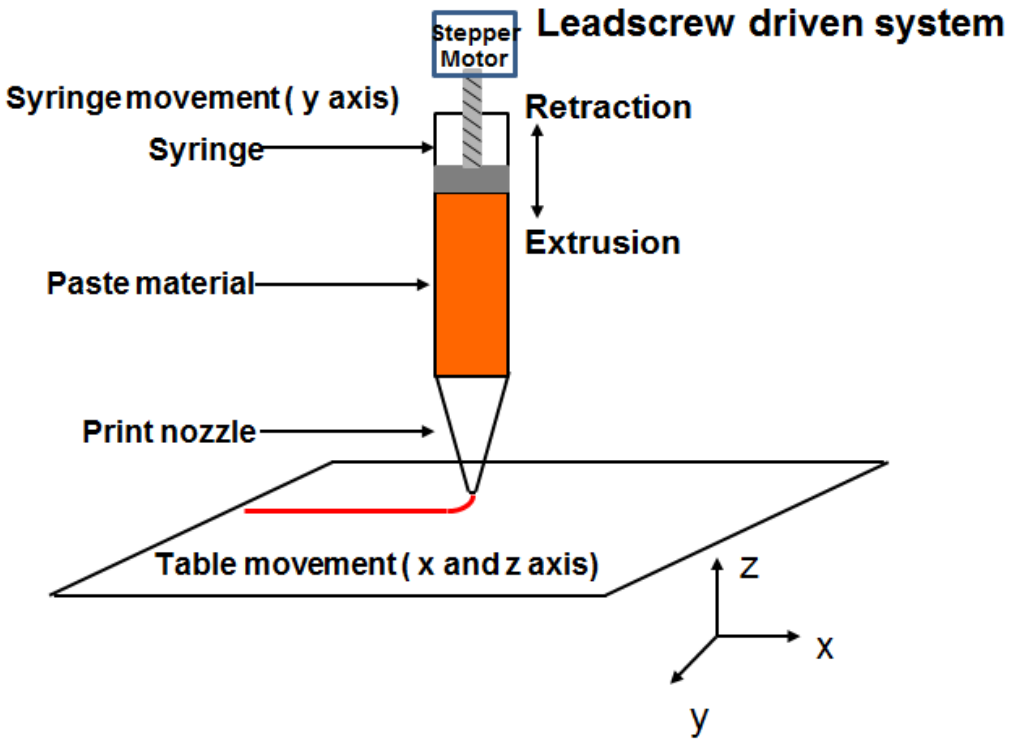

Fig. 1-14. Schematic of paste deposition system.

1.3.2. Research in additive manufacturing technologies in power electronics

Increasingly, the AM technology is being applied to a wide variety of industrial processes, as exemplified in Fig. 1-15 [82, 83]. The Department of Energy (DOE) anticipates that additive processes will eventually be 50% more efficient in terms of energy usage in comparison to today's 'subtractive' manufacturing processes.

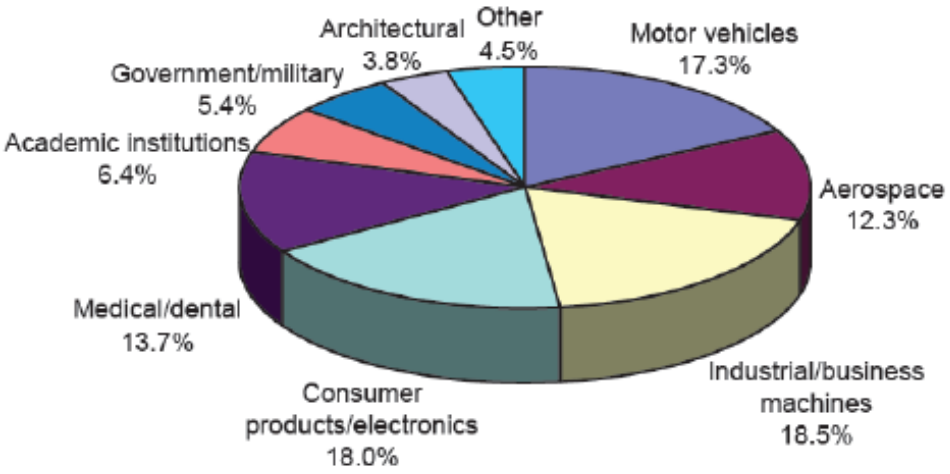

Fig. 1-15. Industries served by AM manufacturers and service providers.

Recently, a number of researchers have explored the application technology of AM in power electronics. For example, studies conducted at Oak Ridge National Laboratory (ORNL) in 2014 [84] reported a 3D-printed aluminum heat sink and a plastic lead frame for a 10-kW power inverter, followed in 2016 [85] with a ferrite E-core with a relative permeability of about 2; Wei Liang *et al*. [86] 3D-printed a plastic structure as a mold for making a unique sterling-silver inductor; Proto-pasta [87] introduced an iron-powder-filled polylactic-acid (PLA) filament for use with a FDM 3D printer to make magnetic cores with relative permeability of about 1.5; Yunqi Wang *et al.* [88] developed a NiZn-ferrite-filled acrylonitrile-butadiene-styrene (ABS) filament for a FDM printer with relative permeability of about 2; and Jyun-Jhong Kai *et al.* [89] used the selective laser sintering (SLS) printing process with a FeSiCr alloy powder to form a toroid core with magnetic properties better than silicon steel.

The key benefits of AM—including shorter lead times, mass customization, reduced parts count, more complex shapes, less material waste, and lower life-cycle energy use—

reinforce its potential for fabricating and integrating magnetic components. It must be noted, however, that magnetic components contain two types of materials: metal and magnetic. Although 3D-printing is ideal for making complex and intricate structures, fabricating parts containing different types of materials presents a formidable challenge in advancing AM technology. Indeed, to date there are no published reports of successfully utilizing 3D-printing to form magnetic components that incorporate both magnetic and metal materials.

1.4. Motivation and Objectives

1.4.1. Motivation for this Investigation

The interest in fabricating smaller converters featuring high power density and high efficiency is now challenging conventional fabrication and integration processes for the magnetic components. Accordingly, available AM techniques have been evaluated with the goal of simplifying manufacturing techniques and improving the integration capability of power magnetics. AM techniques have evolved rapidly as applications have progressed from rapid prototyping to the production of end-use products. Additive equipment can now use metals, polymers, composites, or other powders to "print" a range of functional components, layer by layer, including complex structures that cannot be manufactured by other means. Therefore, 3D-printing has the potential to further improve high-density magnetic integration and enable mass-production — if the design of both the manufacturing methodology and functional materials can be developed for the technology. The feasibility of using AM techniques to fabricate magnetic components must be further explored.

The current design methodology for AM technologies overlooks the impacts of the varieties and varied properties of printing materials, which results in an iterative process adjustment between material input and printed functional parts. It is critical to develop a design methodology for fabricating functional multi-material parts with AM technologies. Thus, a novel design technology approach has been applied in fabricating magnetic components for power electronics integration.

The essential magnetic components include the magnetic core and metal windings, which implies that the AM technique of choice must be capable of processing hybrid materials. For the metal feedstock, different types of raw material input include metal filaments for a FDM printer, metal inks for an ink-jet printer, and metal paste for a paste-extrusion printer. While for the magnetic feedstock, limited magnetic materials can be found; more importantly, none of them are compatible with currently available metal feedstock materials. Therefore, another motivation for this research is to develop a type of magnetic material that is compatible with metal feedstock materials—ultimately for use in additive manufacturing. Another important aspect of producing magnetic components via 3D-printing is optimizing the process of utilizing AM techniques to process metal and magnetic materials simultaneously. As such, the performance of the 3D-printed magnetic components must be thoroughly characterized to evaluate the designed methodology.

1.4.2. Objectives of the research

Based on the motivation discussed above, the objectives of this investigation are listed below:

1. Develop a process flow chart for utilizing additive manufacturing technology in the area of power electronics to realize high-density magnetic components

fabrication and integration.

2. Design, formulate, and characterize a type of low-temperature curable magnetic paste for the AM platform.
3. Fabricate magnetic components with both winding and magnetic core.
4. Characterize the performance of 3D-printed magnetic components for power electronics applications.

1.5. Summary of dissertation organization

Following this introductory chapter, Chapter 2 discusses a design methodology for fabricating functional multi-material parts with AM technologies. A process flow chart of 3D-printed magnetic components was developed. Accordingly, this chapter includes a review of the additive equipment for fabricating magnetic components and the materials selection for the printer feedstock. A paste extrusion-based 3D printer from Hyrel 3D company was utilized for this investigation due to its ease and flexibility of co-processing multiple materials. A commercially available, low-temperature (< 250^{o}C) sinterable nanosilver paste invented in our lab was evaluated and used as a conductive winding feedstock for the printer. Due to the lack of commercially available magnetic pastes, an approach was proposed for fabricating low-temperature (< 250^{o}C) curable magnetic pastes utilizing soft magnetic fillers mixed with a polymer binder. The selected magnetic fillers used in the paste formulation were round-shaped particles of permalloy and flake-shaped particles of glassy-alloy. The selected thermoset polymer was Cyclotene 3022, Benzocyclobutene (BCB).

Chapter 3 describes the methods of design, formulation, and characterization of low-temperature curable magnetic pastes. Specifically, 3D finite-element models of the paste

consisting of periodic unit cells of magnetic particles and flakes in the polymer matrix were constructed. Ansoft Maxwell was used to simulate the magnetic properties of the paste. Then, flowable pastes with varying amounts of Metglas up to 12.5 wt% in the magnetic fillers were prepared. The rheological properties of the paste were characterized. To evaluate the performance of the cured pastes, toroid paste cores were fabricated, which were injection-molded and cured at 250^{o}C. Subsequently, the resistivity and magnetic properties (i.e., complex permeability and core loss density) of the cores were measured. The microstructures of the cores were examined by scanning-electron-microscopy (SEM) to explain the performance of the cured pastes.

Chapter 4 demonstrates the feasibility of 3D-printing magnetic components and presents the characterization results of the 3D-printed magnetic components. Magnetic components with differing levels of complexity, including planar inductor, toroid inductor and constant-flux inductor, were designed. The formulated soft magnetic paste was used as a feed material for printing the magnetic core, and a commercial nanosilver paste was used for printing the winding. We then investigated the extrusion mechanisms of the Hyrel 3D-printer and optimized the printing processes to achieve the desired structures. All of the 3D-printed magnetic components were characterized for their properties, including inductance and dc winding resistance. The microstructures of the winding and core were examined to determine their magnetic properties and suggest areas for improvement.

Chapter 5 summarizes the main conclusions of this dissertation and proposes potential future work.

CHAPTER 2. DESIGN METHODOLOGY AND MATERIALS SELECTION

2.1. Introduction

Currently, the design methodology for AM technologies, as shown in Fig. 2-1 [90], neglects the impacts of the varieties and varied properties of the printing materials, instead emphasizing the printed complex structures. This methodology will result in the iterative adjustment process between and material input and final printed parts when it is applied in fabricating functional multi-material parts. Therefore, it is critical to develop a design methodology for fabricating functional multi-material parts with AM technologies, which can then be applied toward the fabrication of magnetic components.

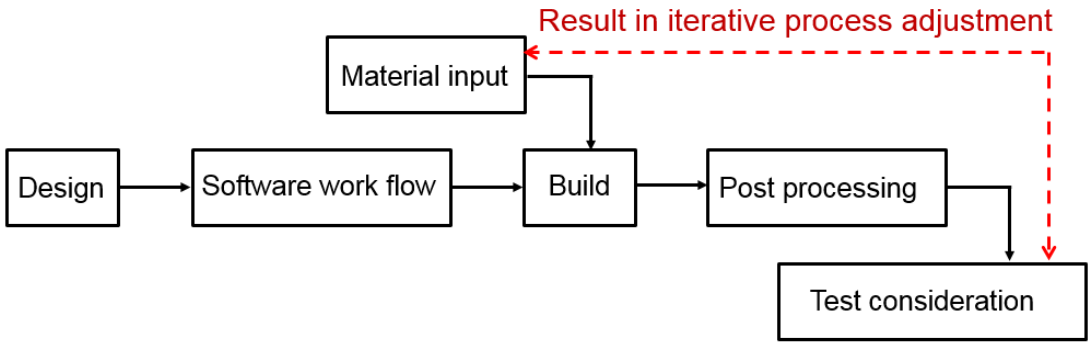

Fig. 2-1. Current Flow chart of additive manufacturing process.

This chapter firstly describes a process flow chart for 3D-printing functional multi-material parts, after which it addresses how this flow chart is applied toward the fabrication of magnetic components. Guided by the flow chart, this chapter illustrates the additive equipment and functional materials for fabricating magnetic components, the associated experimental techniques, and materials selection processes.

A commercially available, multi-material, paste-extrusion 3D printer, which has the capability of processing hybrid material systems and offer more flexibility in feed

materials, was selected to fabricate the magnetic components. The commercially available functional materials, including metal paste and magnetic paste, were evaluated to serve as feedstocks for the printer. The processing and performance requirements for the 3D printer and the PE applications were thoroughly evaluated. A commercial nanosilver paste was selected to be the winding feedstock and subsequently evaluated. Currently, however, there is no magnetic paste that could serve as the magnetic feedstock to form the core part of the magnetic components. Accordingly, this chapter also includes a description of a potential approach for developing a soft magnetic composite/paste, which could serve as the magnetic feedstock to form the core. Finally, a discussion of the magnetic fillers and polymer binder utilized in this investigation is included.

2.2. Process flow chart of 3D-printing functional multi-material parts

In order to apply the AM technology in processing magnetic components, a process flow chart of 3D-printing functional multi-material parts was developed, which is shown in Fig. 2-2. The varieties and properties of the input materials are carefully considered in this flow chart. The process of adjusting the input materials begins by considering how to maximize the quality of the final functional parts. Shown in Fig. 2-3 is the application of the process flow chart to fabricate magnetic components. For fabricating the magnetic components, the additive equipment should have the capability of processing at least two materials simultaneously. The metal and magnetic materials should be prepared for the feedstocks of the 3D printer. Based on the flow chart, the following sections will describe the equipment techniques and materials selection for this study.

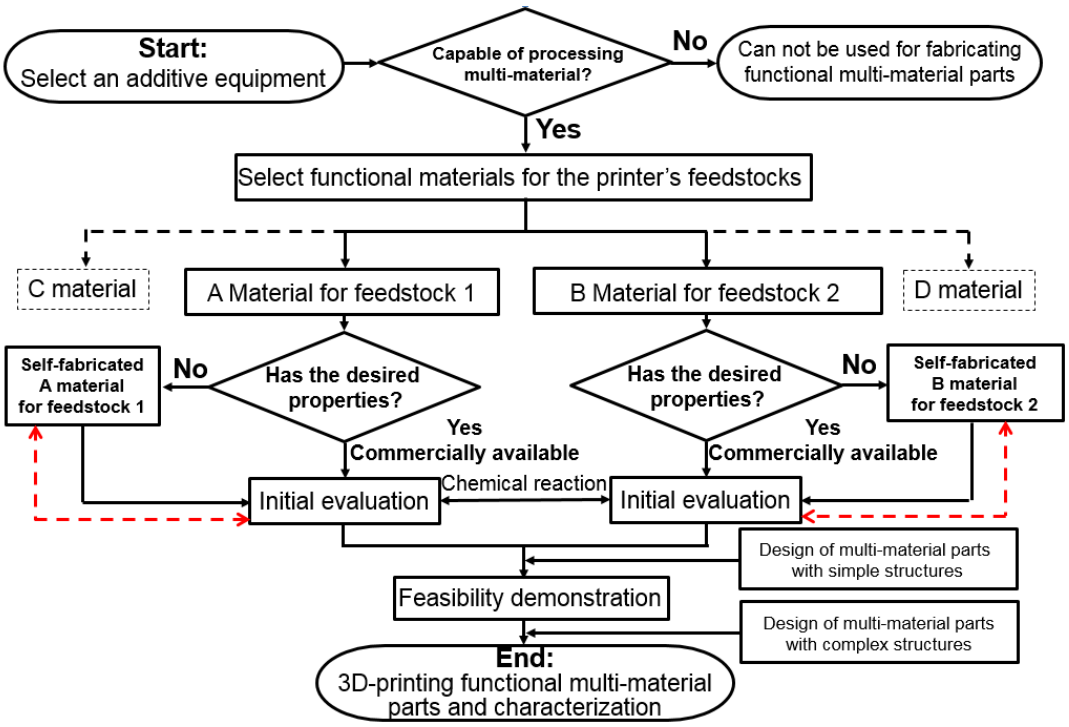

Fig. 2-2. Process flow chart for additive manufacturing functional multi-material parts.

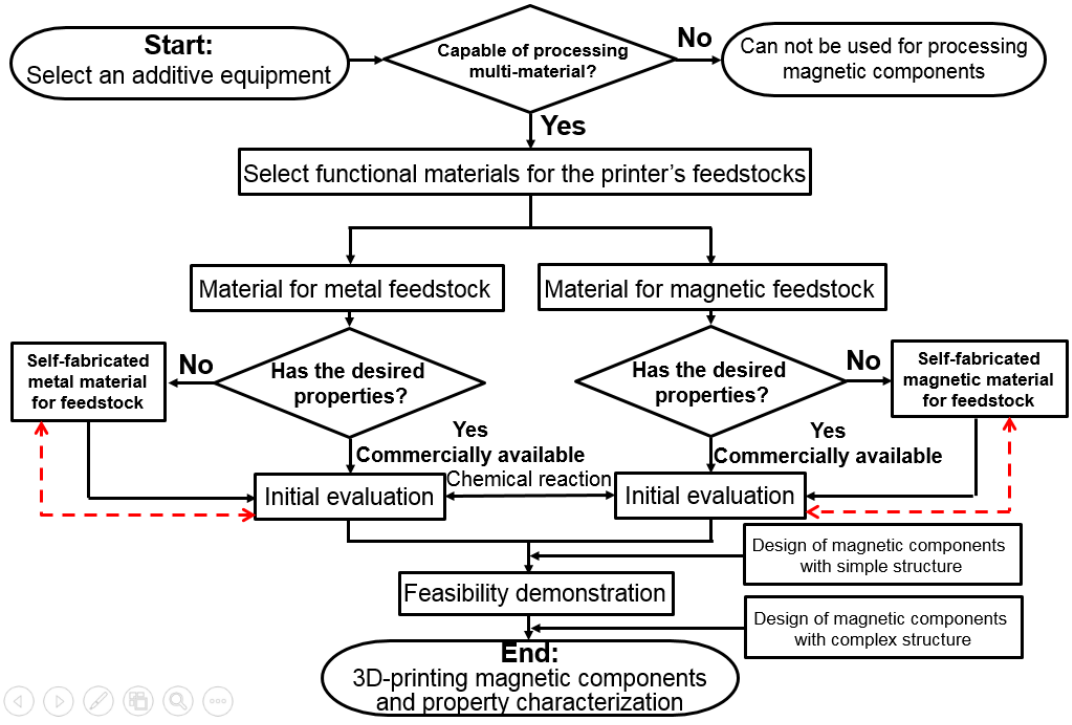

Fig. 2-3. Process flow chart for additive manufacturing magnetic components.

2.2.1. Additive equipment selection for magnetic components

A PE magnetic component is made up of at least two types of inorganic materials: an electrically insulating magnetic material and an electrically conducting winding. Recall that there are three types of AM technologies that can potentially be used to fabricate magnetic components: the ink material systems, the molten material systems, and the paste extrusion systems. A commercial ink-based AM technology designed for making electronic circuits is not suitable for the PE application since it prints thin films of a few micrometers thick at a time and then uses a laser beam for sintering. This process, however, is prone to cracking the thicker films required for a PE magnetic component [91]. With respect to the other commercial filament-based AM technologies, the properties of currently available metal and magnetic filaments do not lend themselves to practical application in the area of PE. Moreover, properties such as the relative permeability of the magnetic filament cannot easily be modified or improved.

The paste extrusion system has the capability to build parts layer-by-layer by putting down thin films (tens of micrometers thick) one after the other, after which a low-temperature sintering or curing process is used to complete the part. This type of AM technology has been used by scientists to make human organs, such as ears [92, 93]. Moreover, the feed materials for paste material systems can offer more flexibility with respect to selection of feed materials in comparison to molten material and ink-jet systems. The paste form or colloidal form of metal, ceramic, or magnetic powders in organic oligomers, binder, and solvents can be printed by the paste extrusion 3D-printer. Additionally, use of paste as the feed material reduces waste, lowers the equipment cost, and simplifies the parts construction process. The paste-based additive process can also be

readily scaled-up to manufacture a multi-material, multi-functional system by inserting multiple paste materials into a feed-cartridge assembly. Therefore, a multi-extruder paste extrusion 3D printer is an excellent candidate to handle both metal and magnetic paste materials with the goal of fabricating power magnetics.

In this investigation, we utilized the Hyrel system 30M multi-extruder paste-extrusion 3D printer shown in Fig. 2-4 to fabricate the magnetic components [94]. The Hyrel system 30M can print over a 200×230 mm area and achieve feature sizes below 50 μm by using a lead-screw driven system. It has a feed-cartridge assembly with four extruders (only three are shown in the figure) that can print four different paste materials stored in syringes. This process platform offers the potential for further integration of a power electronics circuit via the concurrent manufacturing of capacitive, magnetic, and resistive components.

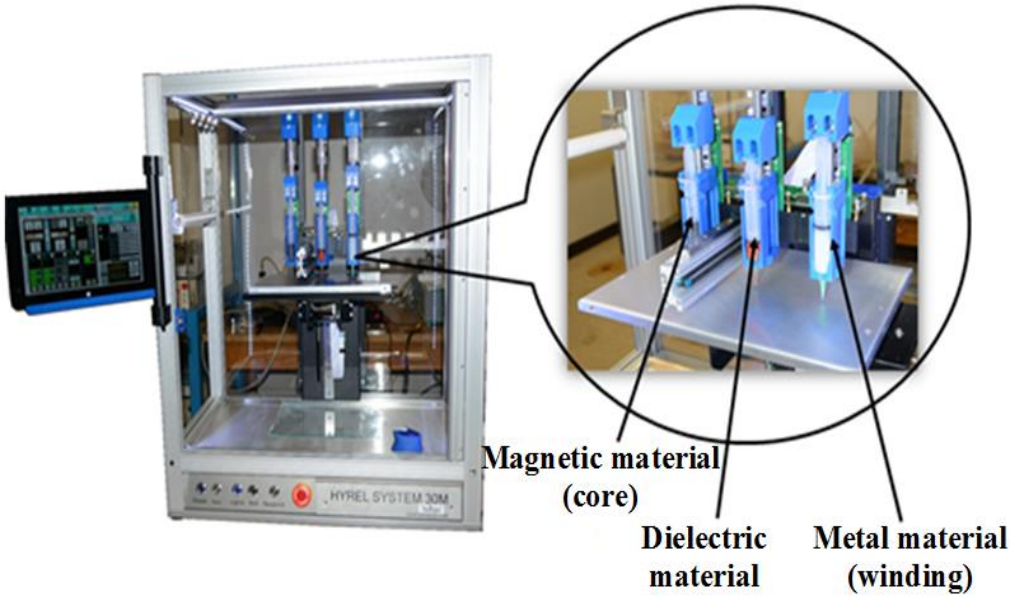

Fig. 2-4. Hyrel 30M multi-extruder paste-extrusion 3D printer with syringe dispersing heads.

2.2.2. Material selection for metal feedstock

- **Desired Properties of Metal Paste —** In order to select a compatible and high performance metal paste for the paste-extrusion system, as well as form the winding part of the magnetic components for PE applications, there are some important processing and performance properties required for the metal paste and the densified metal, respectively. In the case of the former, the desirable processing properties for a metal paste material include the following: (a) it should display shear thinner behavior so that the paste can flow through fine nozzles without clogging [95], (b) the viscoelastic behavior of the paste should respond as a solid material would to enable printing of self-supporting features [96], (c) the metal paste material should facilitate pressure-less processing to form the 3D structure, (d) the metal paste must be able to be processed by the 3D printer at temperatures below 250^{o}C for easy integration in PE circuits, and (e) it must remain crack free when a single layer print thickness is larger than 100μm. With respect to the desired performance properties of the print metal, it should have electrical resistivity close to 1.7×10^{-6} Ω·cm to compete with current pure copper winding, it should feature thermal conductivity higher than 100 W/m•K, and it should be operable at temperatures higher than 100^{o}C to accommodate actual manufacturing conditions. Finally, good adhesion between the printed metal and the magnetic or dielectric materials is expected—for instance, shear strength greater than 10MPa.
- **State-of-the-art Metal Paste for the 3D Printer —** Currently, several commercial metal or conductor paste/ink materials are available for extrusion-type 3D printers. The properties of selected metal paste or ink materials are listed in Table 2-1 [97-104]. The

properties of the nanosilver paste from NBE Tech, LLC (originally invented in our facilities) demonstrate its efficacy to serve as the winding material. Specifically, this material can be sintered at temperatures below 250^{o}C, resulting in excellent thermal and electrical properties [105], and the crack-free single layer print thickness is larger than 100 μm. Some inks comprised of nanoparticle silver or copper (see Table 2-1) also have good electrical conductivity; however, most of these inks are only able to print conductive films less than 10 μm thick and need a UV curing system to complete the structure. Additionally, magnetic components in most power electronic circuits require winding thicknesses of at least tens of microns to reduce winding loss. Therefore, nanosilver paste from NBE Tech, LLC was selected as the feedstock for the winding material in this study.

- **Initial Evaluation of the Selected Metal Paste —** To evaluate the extrusion feasibility and printed performance of the paste, several experiments were conducted. Fig. 2-5 shows that the nanosilver paste can be adapted to the 3D printing platform and extruded out to form a winding structure. The nanosilver paste can achieve a crack-free 3D-printed single layer thicker than 200 μm. Table 2-2 lists the electrical resistivity of the 3D-printed winding after the low-temperature sintering process. Currently, the electrical resistivity of low-temperature sintered 3D-printed winding is about three times higher than that of pure silver wire.

Table 2-1. Characteristics of selected metal pastes or ink materials

Material	**Processing temperature**	**Single layer print thickness**	**Resistivity (Ω·cm)**
Nano-silver ink (AgCite™)	Low temperature sintering (~ 250°C)	< 2.5 μm	2.8×10^{-6}
Nano-copper Ink (Gwent group)	Special laser curing	< 10 μm	9×10^{-6}
Graphene Ink (Northwestern University)	high-intensity pulsed xenon lamp to anneal the printed graphene	< 10 μm	$\sim10^{-3}$
Silver flake polymer paste (DuPont CB028)	Room temperature drying UV curing	< 20 μm	$\sim10^{-3}$
Voxel8 Silver paste (Voxel8, Inc.)	Low temperature sintering (<250°C)	> 100 μm	5×10^{-5}
Nanosilver paste (NBE Technologies, LLC)	Low temperature sintering (< 250°C)	>100 μm	5×10^{-6}
Copper-tin paste ORMET circuits.inc	Low temperature curing (< 210°C)	< 50 μm	5×10^{-5}
Copper paste Northwestern University	High temperature curing (> 600°C)	< 50 μm	Not available
Gallium-indium Slurry North Carolina State University	Room temperature drying	Not available	$\sim10^{-3}$

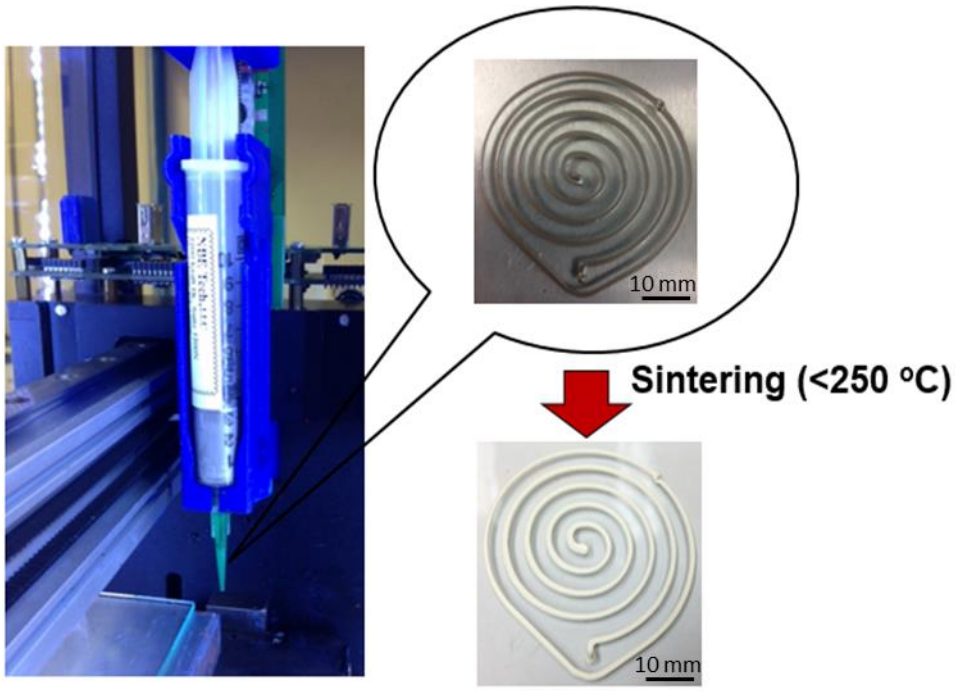

Fig. 2-5. Commercial nanosilver paste from NBE Tech, LLC for paste-extrusion 3D printer.

Table 2-2. Electrical resistivity of low-temperature sintered 3D-printed winding in comparison to bulk silver.

Materials	**Electrical resistivity (10^{-6} Ω·cm)**
250°C sintered 3D-printed silver winding	4.8
Pure silver wire	1.6

2.2.3. Material selection for magnetic feedstock

- **Desired Properties of Magnetic Paste —** There are also several critical processing and performance properties for the magnetic paste if the overall process is to succeed. In addition to the processing properties that were previously outlined for the metal

paste, the desired performance properties of the printed magnetic core should feature a relative permeability at the range from 10 to 50. A printed core with such characteristics can serve as an inductor core material at working frequencies up to 1-MHz. Also, the operating temperature of the printed core should be higher than 100^{o}C to accommodate actual operational conditions for power magnetics.

- **State-of-the-art Magnetic Paste for the 3D Printer —** Unfortunately, there is no commercially available magnetic paste or ink for extrusion type 3D printers. Additionally, there is limited published research documenting the use of magnetic paste/ink in a paste-extrusion AM platform. The properties of the two known published paste or ink materials are listed in Table 2-3 [100, 106]. The magnetic ink developed at Georgia Tech is used for RF high-frequency applications. However, the relative permeability of the cured ink is less than 3, which is too low to serve as a core material for power magnetics. Also, it is only able to print magnetic films less than 50 μm thick and requires a UV curing system to complete the structure. The other magnetic paste developed by Northwestern University is able to print thick structures with a layer-by-layer curing process. The printed structure can be dried at room temperature, however, it requires a high-temperature (> 600^{o}C) sintering process in a well-controlled hydrogen atmosphere to form the final part. Therefore, this process is incompatible with the use of metal paste and not suitable for PE integration. Therefore, development of compatible and high performance magnetic pastes is critical for the 3D-printing of magnetic components.

Table 2-3. Characteristics of magnetic pastes or ink materials published in the literature.

Material	Processing temperature	Single layer print thickness	Relative permeability
Ferromagnetic ink (Georgia Tech)	UV curing	< 50 μm	< 3
3D-printable powder-based liquid inks (Northwestern University)	Room temperature during for green part; High temperature (600°C) sintering in H_2 to form the final part.	> 100 μm	N/A

2.3. Potential method for developing a magnetic paste

In order to guide the fabrication of the magnetic paste, a process sub-flowchart was developed. As shown in Fig. 2-6, a viable low-temperature curable magnetic paste should have good magnetic properties and be able to be shaped at low temperature (< 250°C). Moreover, the other properties, including rheological properties and chemical reactions with the metal paste, should also be considered when fabricating the magnetic paste.

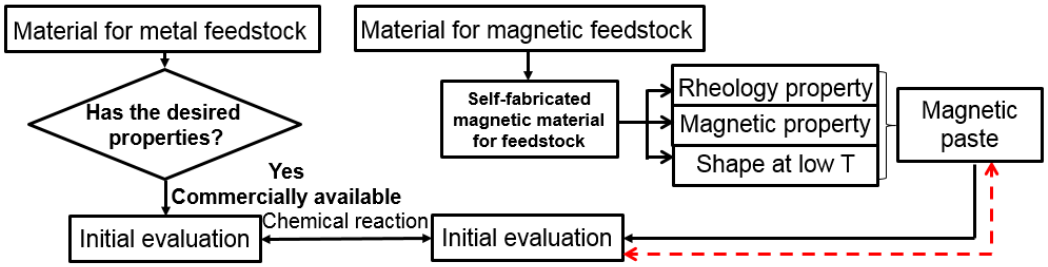

Fig. 2-6. Process sub-flowchart of fabricating magnetic paste.

Based on the sub-flowchart, accordingly, a composite of soft magnetic particles and a polymer binder could potentially achieve the desired properties. The magnetic particles

can provide the magnetic properties, while selection and design of the polymer coating enables one to tune the shaping temperature and rheological properties. Ideally, the polymer coating will bond with the metal paste at low temperature and not affect the properties of any of the pastes.

Actually, the idea of using soft magnetic composites consisting of magnetic particles in a non-magnetic insulating matrix for power electronics applications is not new. In fact, references to this approach first appeared more than 100 years ago [107, 108]. It is particularly important that the metal-based magnetic materials serve as the filler portion in the composite—mainly because metal-based magnetic materials exhibit high initial permeability and saturation magnetization, but are limited to a few hundred kilohertz due to high eddy current losses. Mathematically, the total core loss, W, can be represented by the following equation [109]:

$$W = W_e + W_h = (k_1 B_m^2 t^2 / \rho) f^2 + k_2 B_m f \tag{2.1}$$

where W_e is the eddy current loss, W_h is the hysteresis loss, f is the frequency, B_m is the excited magnetic flux density, ρ is the resistivity, t is the thickness of the magnetic material, k_1 and k_2 are the coefficients to the weight and volume of the magnetic powders. As shown in equation (2.1), one way to reduce the eddy current loss is to increase the resistivity of the magnetic material, which resulted in the idea of insulating the metal-based magnetic fillers. In so doing, the insulated magnetic composites can take advantage of high relative permeability, high magnetic saturation, and a high operating frequency range—but with low eddy current losses.

Generally speaking, insulating coatings can be classified into two main categories: inorganic and organic coatings [108]. Inorganic coatings can be subdivided into several categories: metallic oxide coatings (such as Fe_2O_3 [110]), phosphate coatings (zinc phosphate, iron phosphate and manganese phosphate [111]), and sulfate coatings [112]. Organic coatings can be divided into two categories: thermoplastic coatings and thermosetting coatings. There are two important conditions for using organic coatings for composites: (1) the rheology properties of the composite have to be determined according to the rheological properties of the coatings [113], and (2) the curing temperature of the composite must be lower than 300^{o}C. Therefore, to formulate a magnetic paste with desired processing properties, the organic coating should be used as an insulator matrix for the magnetic fillers.

2.4. Materials selection for magnetic paste formulation

The physical and magnetic properties of the magnetic pastes can be tailored by the choice of polymer matrix, as well as magnetic particle composition, size, and concentration [114]. To further clarify the development of a magnetic paste with desired properties, the following sections discuss the magnetic filler and polymer matrix utilized in this investigation.

2.4.1. Selection of magnetic filler

The magnetic filler selection should consider three aspects: filler material, filler size, and filler shape:

- **Filler Material —** The choice of filler material is critical to the magnetic properties of the magnetic paste—mainly hysteresis loss and relative permeability. Additionally, the

magnetic filler must combine as many as possible of the following characteristics at moderate cost:

1. Low hysteresis losses (Hc);
2. High electrical resistance (ρ);
3. High permeability at low field strength (μ_i);
4. High saturation value (B_{sat});
5. No aging effect;
6. Uniform magnetic characteristics.

Two types of metal-based soft magnetic materials have the potential to be filler materials: (1) ferromagnetic materials based on Fe and Ni, and (2) a metallic-glass magnetic material [115]. Both of these compounds provide high initial permeability, low hysteresis loss, and high saturation magnetization for high frequency applications. These materials offer other advantages, including good corrosion resistance and low magnetostriction.

- **Filler Size —** The relationship between coercivity and magnetic particle size is shown in Fig. 2-7. Transitioning from single-domain to multi-domain, the coercivity of magnetic particles reaches a maximum. For larger particle sizes, the coercivity is lowered as the particle subdivides into domains. After reducing the particle size below a critical value, the magnetization can randomly flip directions under thermal fluctuations at room temperature. The averaged magnetization is zero, and thus the particle exhibits zero hysteresis/coercivity. This phenomenon is called superparamagnetism, wherein the material shows a magnetic response similar to that of paramagnetic materials, but with a much higher susceptibility [116]. Therefore,

smaller particle sizes are preferred for soft magnetic composites due to the shrinking of eddy current loop area and, hence, the reduction of eddy current loss within the particles. As a result, a higher permeability and reduced loss is observed in magnetic composites of decreased particle size [117]. However, if the particle size were in nano-scale, the solid loading of the fillers would be limited to 10 weight percent due the large surface area of the nano-size particles [118]. The low solid loading will decrease the relative permeability of the magnetic paste. Therefore, in this work the particle size of the fillers is limited to micron-size due to considerations of the relative permeability of the magnetic paste.

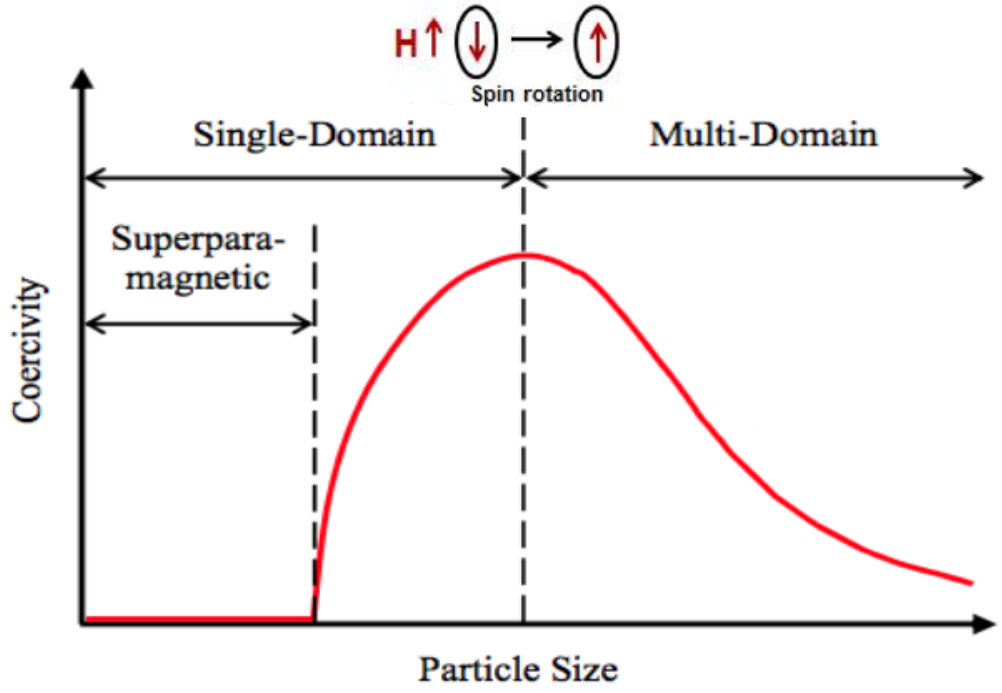

Fig. 2-7. Coercivity dependence of magnetic particle size.

- **Filler Shape —** The filler shape is also a very important factor that can affect the magnetic properties of the paste. Assuming that there is only one kind of magnetic filler

with a certain shape in the composite, the relative permeability of the composite can be represented by the following equation:

$$\mu_r(\Phi) = 1 + B\Phi^2 \tag{2.2}$$

where μ_r is the relative permeability of the composite, Φ is volume fraction of the filler, range from 30 to 60 percent, B is a coefficient depends on the shape of the magnetic filler. Therefore, shape is a significant factor that can impact the resulting properties of the magnetic composite—making the shape of magnetic fillers a critical consideration. It should also be noted that it is possible to achieve higher magnetic permeability values for a magnetic paste by using complex filler particles, meaning that the filler particles have dissimilar shapes and sizes [119]. Fiske et al. [120] pointed out that the maximum theoretical packing fraction of a composite can be altered by using particles with different shapes or size distributions. One reason for this relationship is that high-aspect-ratio particles reduce the maximum theoretical packing fraction (i.e., the maximum number of particulates that can be incorporated into a composite), while at the same time reducing the percolation threshold. In addition, asymmetrical particles can give rise to higher magnetization than symmetrical particles. Hashin and Shtrikman [121] described the limits for magnetic permeability for a densely-packed composite consisting of coated spheres. They provided a way to tailor a magnetic composite by incorporating flexible flakes and spherical particles. If the flexible flakes are large in comparison to the spherical particles and feature greater magnetic permeability, the flakes can act as if they are "coating" the spherical particles, thereby enhancing magnetic permeability. Fiske et al. [122] also investigated composites made with two

different distinct particles with varying aspect ratios, sizes, and magnetic permeabilities embedded into a polymeric binder. The researchers reported that the influence of introducing high-permeability particles had a greater impact on the enhanced permeability of the hybrid composites in comparison to utilizing high loading levels of the individual fillers. Therefore, to make a magnetic paste with desired magnetic properties for PE applications, magnetic fillers with different shapes were used in this work.

Based on the various factors detailed above, both a permalloy and a metallic-glass magnetic material were selected for this investigation—specifically, to take advantage of their high initial permeability, low hysteresis loss, and high saturation magnetization. A permalloy powder with an average particle size of 12 μm was purchased from ESPI Metals. The properties of the powder are shown in Table 2-4, while Fig. 2-8 presents the SEM images of the powder. A roll of glassy alloy ribbon of 2705M was obtained from Metglas, Inc. (Conway, SC); its properties are listed in Table 2-4. The ribbon, which was approximately 25 μm thick, was ground into flakes through the use of a 6770 SPEX Sample Prep Freezer/Mill Cryogenic Grinder. The milled flakes were then sieved to a length and width ranging from 75 to 250 microns. The grinding process had no effect on thickness. A SEM image of the flakes is shown in Fig. 2-9.

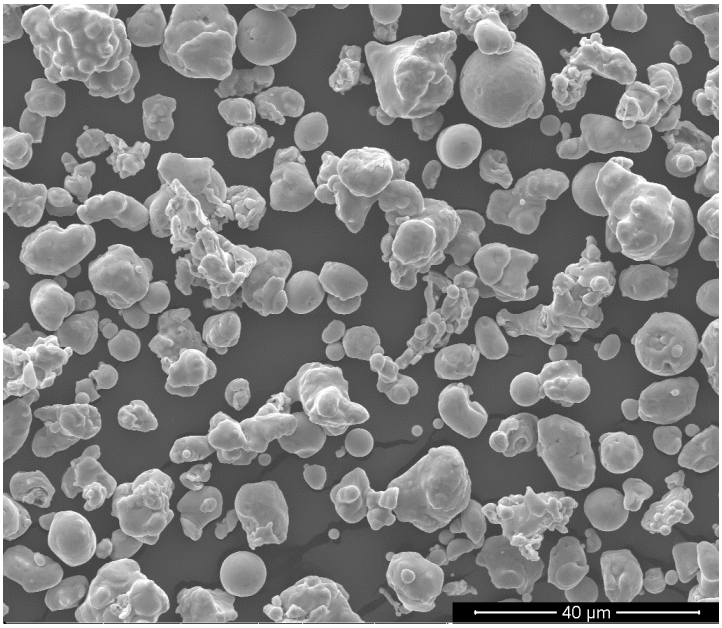

Fig. 2-8. A SEM image of the permalloy powder showing an average particle size of about 12 µm.

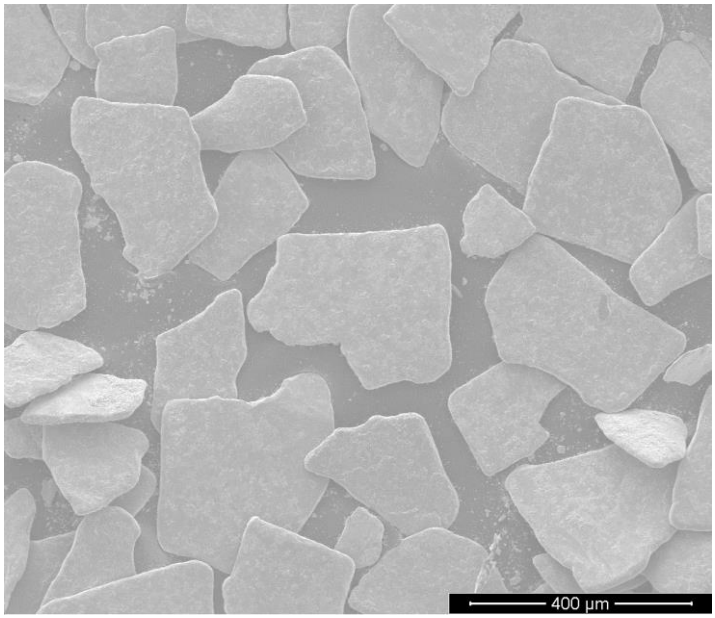

Fig. 2-9. A SEM image of Metglas flakes showing the particle sizes range from 75 µm to 250 µm.

Table 2-4. Properties of selected magnetic fillers.

Magnetic core materials	B_{sat} (T)	H_c (Oe)	μ_i	ρ ($\Omega \cdot$cm)
Permalloy 80 (Average Particle size 12μm)	0.75	0.015	75000	5.8×10^{-5}
Glassy alloy Ribbon (2705M, Thickness 25μm)	0.77	0.012	290000	1.36×10^{-4}

2.4.2. Selection of polymer matrix

As mentioned previously, the characteristics of organic coatings, which include both thermosetting coatings and thermoplastic coatings, are well suited to form the magnetic paste for extrusion-based systems. In comparing the two types, thermosetting coatings are more stable and widely used as insulators for soft magnetic composites in PE applications in comparison to thermoplastic coatings. Indeed, a thermoset polymer is quite stable when exposed to hostile environments. Moreover, once cured, a composite/paste cannot be dissolved, reprocessed, or compression/injection molded. On the other hand, most thermoplastics cannot easily be coated uniformly and continuously onto small iron particles; additionally, thermoplastic coatings are more easily damaged at higher temperatures. Therefore, selecting a thermoset polymer instead of a thermoplastic polymer minimizes the adverse effects of temperature variations on the magnetic and mechanical properties of composites. A variety of thermoset polymers, including epoxy-resins, acrylic esters, polyesters, epoxy-polyesters, and polyurethanes, are widely used as insulating materials for soft magnetic composites[108].

Based on this information, thermoset polymers were selected to serve as binders for

the magnetic fillers utilized in this investigation. In addition, in order to achieve the desired properties of the magnetic paste, the thermoset polymer matrix material had to feature a number of essential parameters: 1) high resistivity to reduced eddy current loss between particles, 2) shear thinner behavior to facilitate the flow property of the paste, 3) quick and on-demand solidification to secure the particles, and 4) low-volume shrinkage after solidification to maintain shape. Based on these property considerations, the thermoset polymer, Cyclotene-3022, Benzocyclobutene (BCB) obtained from Dow Chemical Company, was selected. This polymer is a high-performance dielectric coating, which has been used for high-density microelectronic circuits for quite some time.

The interest in BCB polymer coatings for use in magnetic pastes is due to two important features [123-125]: ease of processing and low dielectric constant/dissipation factor, detailed as follows.

The first requirement is ease of processing by thermal polymerization (< 250^{o}C), which negates the use of catalysts or hardeners, and produces no water or other by-product. Note that BCB polymers are derived from monomers having the structure (a) (Fig. 2-10), in which the R portion may be varied. Thermal stability in the BCB family is determined to a large extent by the R group. On heating to 200°C or higher, the cyclobutene portion of the molecule rearranges, first forming a transient intermediate, o-quinodimethane (structure (b), Fig. 2-10) which, because of its highly reactive double bonds, then reacts with similar molecules or with other unsaturated groups to form a highly cross-linked, high-molecular-weight polymer.

In cyclotene, the R group is a tetramethyl divinyl siloxane (DVS), as shown in structure (c) of Fig. 2-10. The polymerization process is purely an addition type; thus,

unlike polyimides, no water or other by-products are produced. Bis-benzocyclobutene coatings are sold as solutions of BCB oligomers (partially polymerized B-staged) in mesitylene or xylene solvent. Upon evaporation of the solvent and heating in nitrogen between 200 to 250°C, the B-staged material continues to polymerize. An optimum cure schedule is one hour at 250°C, at which point the cyclotene achieves 95% polymerization and results in a hard, transparent coating. It is important that the cyclotene be cured in a dry nitrogen or vacuum. If cured in air it oxidizes, forming anhydride and/or carbonyl groups, as shown in Fig. 2-11, and turns yellowish-brown in appearance.

The second requirement is low dielectric constant (2.7) and low dissipation factor (0.0008), which enhances the stability of these electrical properties over a wide temperature and frequency range, rendering them useful for very high frequency applications. The dielectric constants of BCB range from 2.6 to 2.8 and are relatively flat even in a high GHz region and at temperatures up to 200°C. Dissipation factors are also low (0.0008 to 0.002) and stable over the same frequency range. Fig. 2-12 compares these properties with those of a polyimide. Other electrical properties reported for BCB are volume resistivity of 1×10^{19} Ω·cm and breakdown voltage of 3.0×10^{6} V/cm.

In summary, the advantages of the BCB thermoset polymer include ease of processing, low dielectric constant, and good thermal stability—all of which make it quite suitable to serve as the insulator component in the paste.

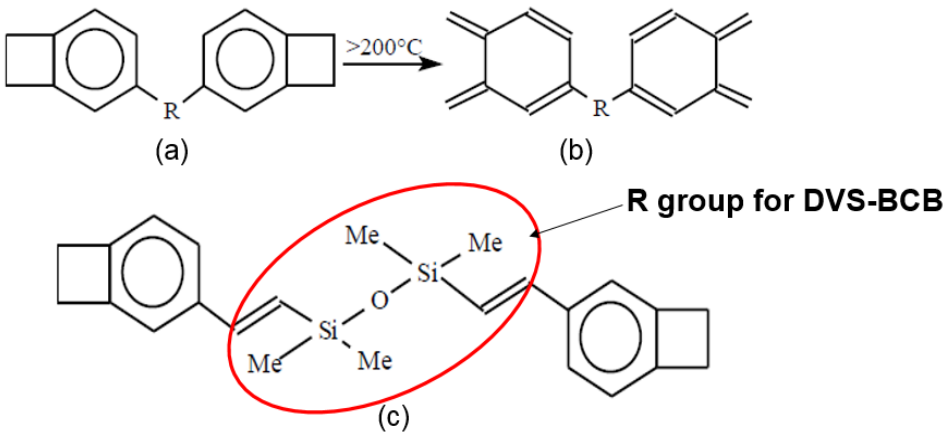

Fig. 2-10. Molecular structures for BCB monomers, (a) BCB monomer, (b) o-Quinodimethane intermediate, and (c) DVS-BCB monomer.

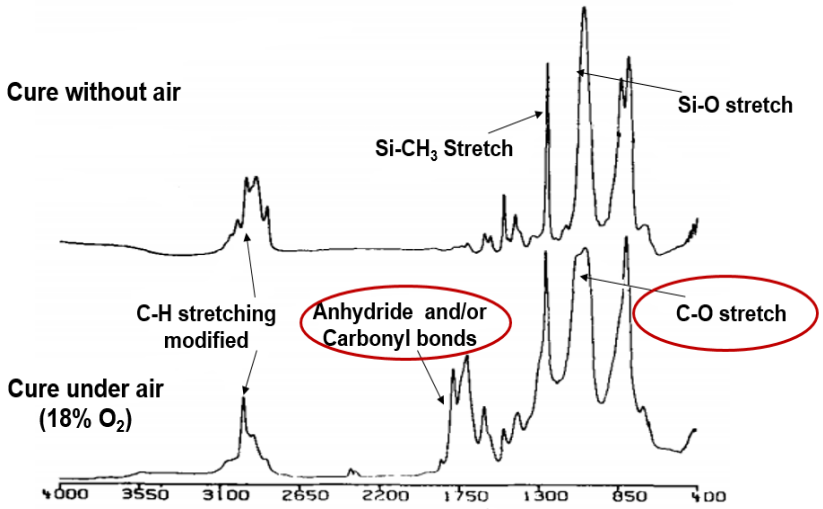

Fig. 2-11. FTIR spectra of BCB cured in the presence and the absence of air.

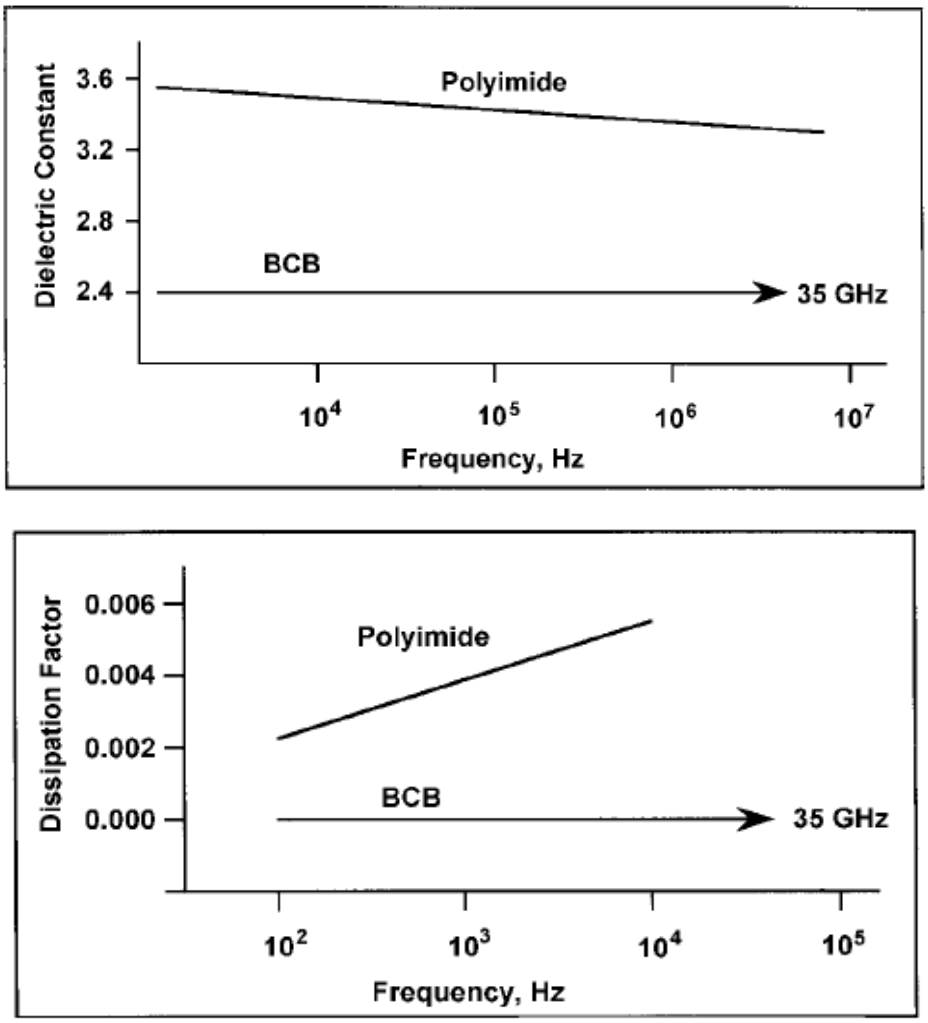

Fig. 2-12. Electrical properties of BCB (Cyclotene) and polyimide as a function of frequency[124].

2.5. Summary

A process flow chart for additive manufacturing of functional multi-material components was developed. This methodology can be used as a general reference in any other research area targeting the utilization of AM technology. In this study, the methodology was applied in fabricating magnetic components. Based on the flow chart, a commercial, multi-material, paste-extrusion 3D-printer was selected to demonstrate the

feasibility of fabricating magnetic components. To obtain the metal feedstock for the printer, commercially available metal pastes and inks were evaluated for their capability of serving as the winding portion of the 3D-printed magnetic components. A nanosilver paste, which earlier had been invented in our lab, demonstrated that it was physically compatible to the 3D-printer and thus was selected for use in this study. Additionally, there is no commercially available magnetic paste as yet identified for use with the printer. It should also be noted that the properties of the magnetic paste currently under research make it unsuitable for PE applications. Thus, the development of a soft magnetic composite/paste that could serve as a magnetic feedstock to form the core part represents a critical aspect of this investigation.

In order to fabricate the magnetic paste for the 3D printer's feedstock, a process sub-flowchart was developed. The soft magnetic composite should contain magnetic fillers and a polymer binder to achieve the desired properties for the 3D printer. To synthesize a paste featuring these desired magnetic properties, available magnetic fillers were evaluated with respect to their particle size, shape, and magnetic properties. Both of the round-shaped particles of permalloy and flake-shaped particles of glassy-alloy were selected. The permalloy round particles (Permalloy-80) with an average size of 12 μm were purchased. The glassy-alloy flaked particles were obtained by grinding the 2705M ribbon. The milled flakes featured a length and width ranging from 75 μm to 250 μm, and a thickness of around 25 μm. The thermoset polymer, Cyclotene 3022, Benzocyclobutene (BCB) obtained from Dow Chemical Company, was selected as the polymer binder for the paste. Benzocyclobutene is widely used in the electronics industry due to its ease of processing (< 250°C), low dielectric constant (2.7), and good thermal stability. The design,

formulation and characterization of the magnetic paste were investigated and results are described in the following chapter.

CHAPTER 3. DESIGN, FORMULATION AND CHARACTERIZATION OF MAGNETIC PASTES

3.1. Introduction

Development of a compatible and efficient magnetic paste is the only factor preventing fabrication of power magnetics using a paste-extrusion 3D printer. Based on the selected magnetic fillers and polymer binders discussed in Chapter 2, this chapter describes the specific design, formulation, and characterization procedures for low-temperature curable magnetic pastes.

As detailed herein, polymer BCB and two soft magnetic fillers of varying shapes—namely, round-shaped permalloy particles and flake-shaped Metglas particles—were used to formulate the pastes. To guide the formulation process, 3D finite-element models of the magnetic-filled-polymer matrix composite were constructed. Ansoft Maxwell simulation software was used to simulate the composite magnetic properties [126]. Based on the simulation results, several formulations of the composite with varying amounts of Metglas flakes added to the permalloy particles were prepared in the form of a paste. The rheological properties of all the pastes were evaluated. The magnetic pastes also were cured to enable characterization of key properties, including electrical resistivity, complex permeability, and high-frequency core loss density. Microstructures of the cores were also characterized by SEM for further improvement on the magnetic properties.

3.2. Design of low-temperature curable magnetic pastes

As shown in equation (2.2), the magnetic properties of the paste are related to the shape and weight percentage of the magnetic fillers. Therefore, optimal magnetic properties of the paste can be tailored by varying the shape and weight percentage of magnetic fillers. To guide the paste formulation, magnetic properties of the composite were simulated by FEA (Finite-Element-Analysis) using Maxwell equations.

3.2.1. Finite-element modeling and Maxwell simulation

To design the appropriate composite formulation, we had to determine the correct ratios of magnetic to polymer, and Metglas to permalloy. Subsequently, 3D FE models of scaled-down versions of the composite in the toroid shape were built, and Ansys Maxwell simulation software was used to simulate the composite magnetic properties. Fig. 3-1 shows two examples of the structural models analyzed by the FE Maxwell simulation method: (a) a quarter of the toroid core containing 90 weight percent of permalloy particles without any addition of Metglas flakes, and (b) a quarter-core model containing 90 weight percent magnetic fillers of which 12.5 wt% were composed of the Metglas flakes. The permalloy powder, which was made up of round-shaped particles with approximated average particle diameter of 12 μm, by one consisting of two sizes of octagon-shaped particles, one 12 μm, and the other 6 μm. The larger particles of permalloy were assumed to occupy a body-centered-cubic lattice, while the smaller particles were positioned at the face centers of the cube. The gap between the nearest magnetic particles was adjusted to match the weight percent of the magnetic fillers in the composite. The Metaglas flakes were assumed to have one size at 8 μm x 190 μm x 25-μm thick. The flakes were inserted

into the composite model by cutting or truncating the octagon-shaped permalloy particles.

For Maxwell simulation, an external winding around the core models was applied and a sinusoidal voltage excitation was set at 1 MHz with an amplitude of 0.1 mV. The magnetic properties of the magnetic fillers, such as their relative permeability and core loss density were obtained from Handbook of Magnetics, Inc.[127] and the datasheet provided by Metlglas Inc.[128]. For BCB, we assumed its relative permeability to be 1.0 with zero loss

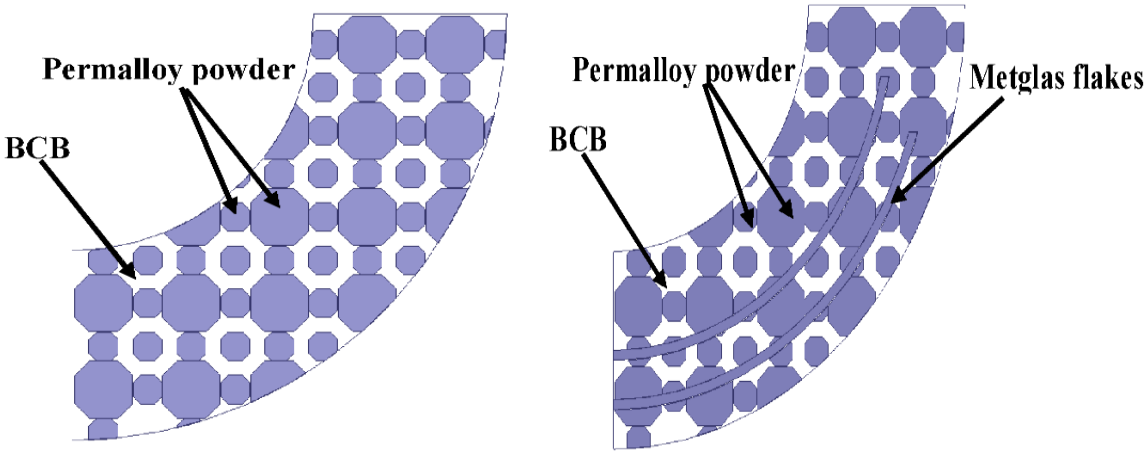

(a) (b)

Fig. 3-1. Structural models of (a) a quarter of toroid core built for simulating the magnetic properties of permalloy-filled-BCB-matrix composite; and (b) a quarter of toroid core with both permalloy particles and Metglas flakes.

3.2.2. Simulated magnetic properties of composite FE models

Fig. 3-2 shows a plot of the effective relative permeability of a composite FE model versus the weight percent of the permalloy particles without addition of the Metglas flakes. The curve takes on the shape of a "hockey stick," with a rapid rise in permeability as the magnetic content reaches beyond 91 wt%. Fig. 3-3 shows the effect of adding Metglas flakes on permeability. Specifically, the addition of 12.5 wt% of flakes in the magnetic fillers (or 11 wt% of the total weight of the composite) increased the relative permeability

of the core by over two times, in comparison to analogous findings for the core with only permalloy. This outcome is not surprising if one examines the flux lines in the composite core shown in Fig. 3-4. The flux pattern shows that the flakes, which were assumed to align with the magnetic field, served as short circuits for the magnetic flux, resulting in lower reluctance—and thus higher effective relative permeability. Without the flakes, the flux lines have to cut through a large number of BCB gaps in between the permalloy particles, resulting in substantially higher reluctance and lower relative permeability. However, higher effective relative permeability means higher average flux density in the core, which is mostly due to high flux carried by the Metglas flakes. As the core loss density increases with flux density, one would expect that the composites with Metglas flakes would evidence higher core loss density. The simulation results in Fig. 3-4 show that most of the energy loss comes from the flakes. Therefore, selecting magnetic flake materials with the desired aspect ratio, high relative permeability, and low core loss density would facilitate the formulation of a composite magnetic core with high effective relative permeability as well as low core loss density.

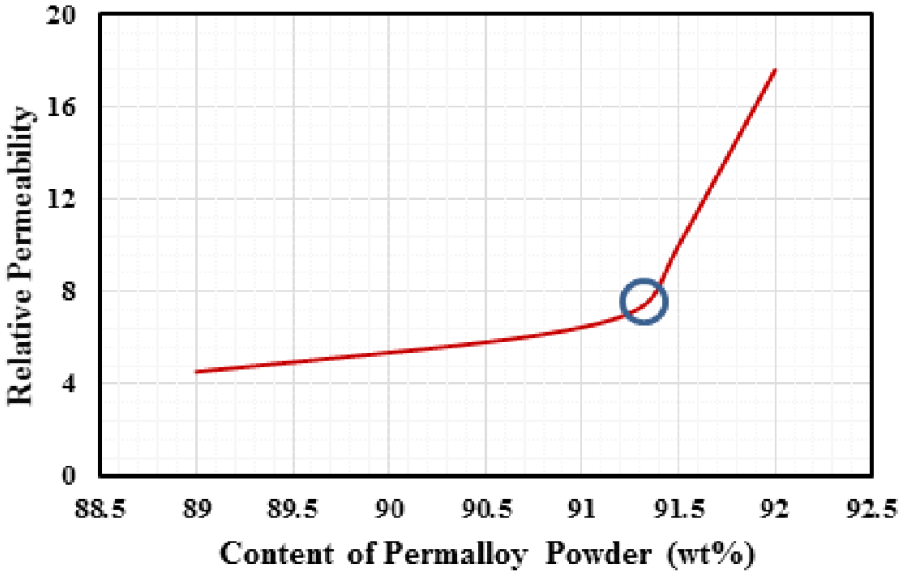

Fig. 3-2. Simulated results of the effective relative permeability of permalloy-BCB composite FE models.

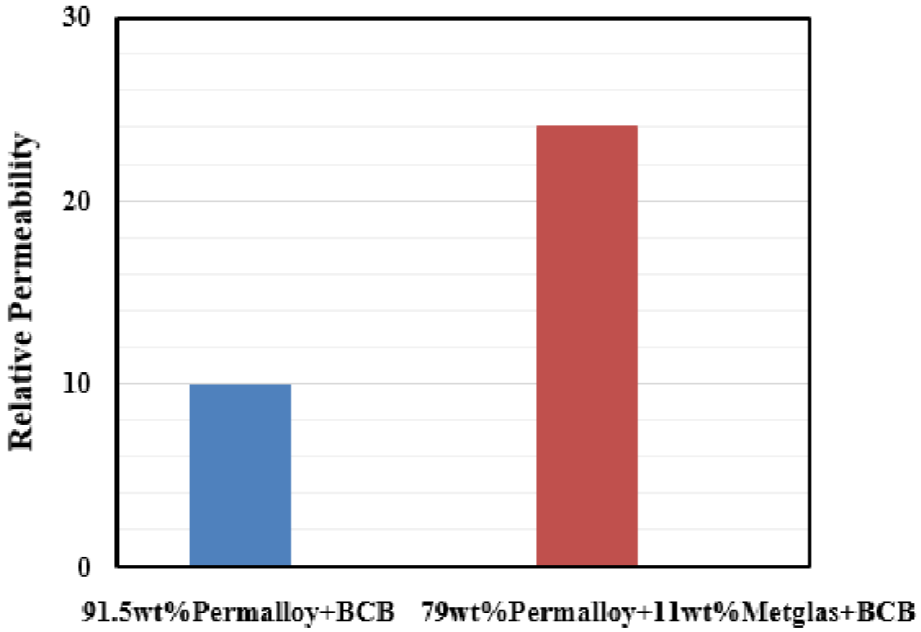

Fig. 3-3. Simulated results on the relative permeability of the magnetic core without and with Metglas flakes.

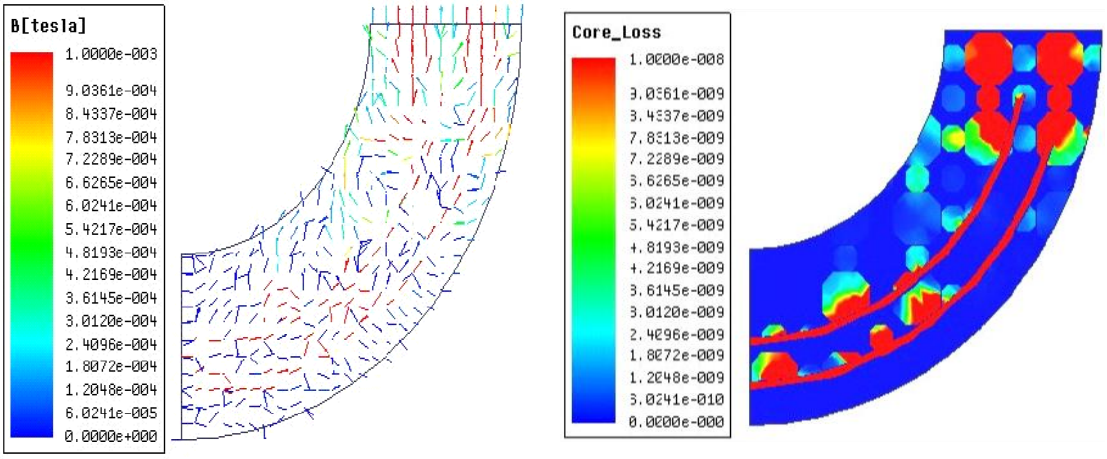

(a) (b)

Fig. 3-4. Simulated flux lines and core loss densities at 1 MHz for the BCB-matrix-permalloy-Metglas core: (a) simulated flux lines and (b) simulated core loss density distribution at 1-MHz.

3.3. Formulation of low-temperature curable magnetic pastes

The investigation was designed to determine the most effective way of coating magnetic particles with polymers—with three main approaches considered [108]: (1) dispersing the particles in a solution of the polymer dissolved in a solvent and driving off the solvent, (2) polymerizing the polymer in site on the surface of the particles, and (3) coating the particles in a fluidized bed with the polymer dissolved in an appropriate solvent. For this study, the first approach was selected.

3.3.1. Formulation of magnetic pastes

Based on simulation results, magnetic pastes were formulated with 10 weight percent of BCB to ensure close packing of the magnetic fillers and sufficient mechanical strength for handling. Of the various magnetic fillers, mixed permalloy particles and Metglas flakes—with the latter at varying percentages of 0 wt%, 5 wt%, 10 wt%, and 12.5 wt%. Since this investigation was only concerned with making paste shapes via a pressure-less

curing process, it was important to formulate flowable pastes by adding other organic components, such as dispersants and solvents, to create uniform suspensions of the magnetic fillers in the organic system. Fig. 3-5 illustrates the major ingredients in a paste formulation. A uniform suspension of the magnetic fillers is crucial for achieving high packing density of the composite after solvent removal and cross-linking of the thermoset polymer. To evaluate the extrusion feasibility of the paste, it was inserted into a 10cc syringe and then affixed to the 3D printer. Fig. 3-6 provides an illustration of printing the as-prepared paste into a toroid shape.

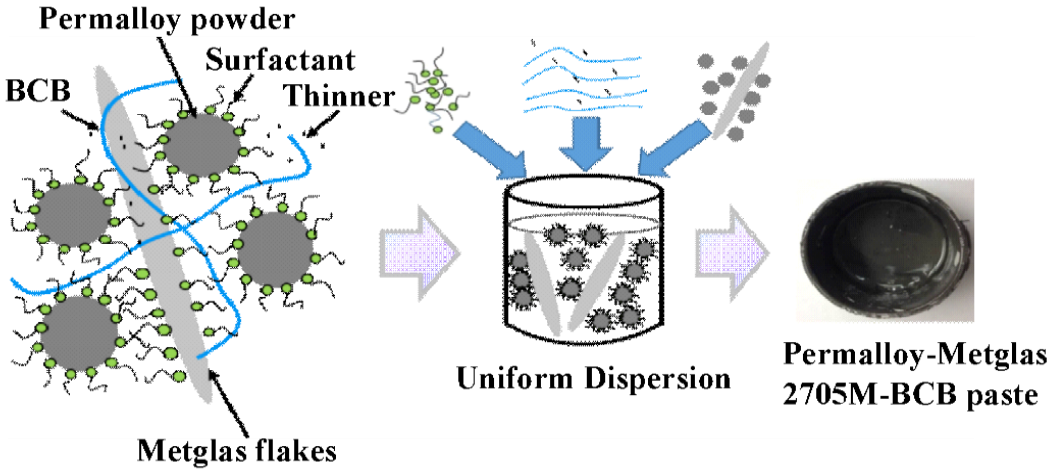

Fig. 3-5. A schematic illustrating the major ingredients comprising a flowable magnetic paste.

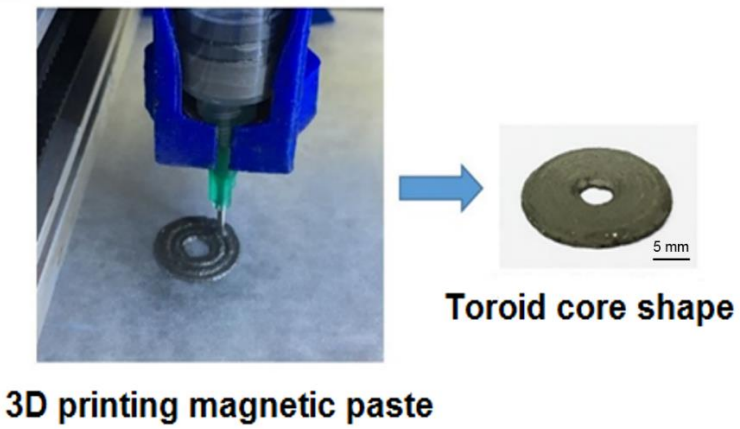

Fig. 3-6. Demonstration of a 3D-printed toroid core shape from the magnetic paste.

3.3.2. Preparation procedures of cured cores

In order to characterize the key magnetic properties of the cured pastes—principally bulk DC electrical resistivity, complex permeability, and core loss density—toroid cores of the pastes were fabricated. Fig. 3-7 shows the process flow for preparing toroid samples. Specifically, magnetic pastes were poured into toroid molds, and then dried and cured by heating at a rate of 1°C/min to 250°C for 30 minutes in a programmable muffle furnace. The as-cured cores had the following dimensions: outer diameter = 20 mm; inner diameter = 14.9 mm; height = 6 mm.

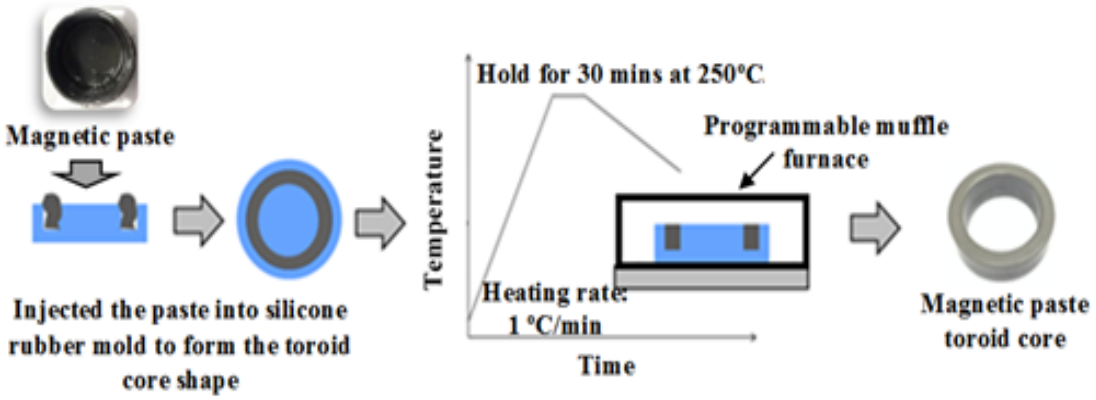

Fig. 3-7. Process flow for fabricating the magnetic paste toroid core.

3.4. Characterization of as-prepared pastes and cured cores

In order to optimize the properties of the magnetic pastes, their properties had to be characterized, including the rheological properties of the paste, as well as the electrical and magnetic properties of the cured toroid cores. The microstructures of the cured cores were also investigated to understand the performance of the paste and improve their properties.

3.4.1. Characterization techniques

- **Oscillatory and Rotational Rheometer —** The equipment shown in Fig. 3-8 was used to measure the complex shear rheology across all material types. The machine is sufficiently sensitive to measure the viscosity of dilute polymer solutions, and yet robust enough to measure the viscoelasticity of high modulus polymers or composites. In this work, the equipment was used to evaluate the viscosity behavior as a function of shear rate, as well as the viscoelastic behavior of the pastes. The paste sample is loaded into the gap of a measuring plate specifically designed to impose simple shear flow when rotated. The measuring system is supported by a virtually frictionless air-bearing pillar, and driven by an ultra-low inertia motor, which is coupled to an ultra-high precision position encoder. The sample and measuring system are also temperature controlled. The rheological characteristics of the paste, including viscosity vs. shear rate, moduli vs. angular frequency, can be determined via a direct readout by the equipment.

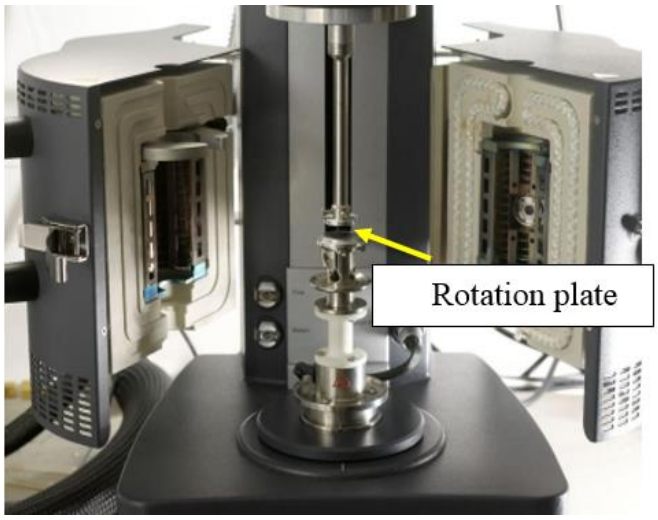

Fig. 3-8. Oscillatory and rotational rheometer.

- **Pico-ammeter/DC Voltage Source —** This equipment was used to measure the DC electrical resistivity of the cured toroid cores. As shown in Fig. 3-9, a toroid core sample holder was designed to connect to the machine. The toroid core sample was coated with silver epoxy on both sides to serve as terminals for the resistance measurement. DC electrical resistivity of the core can be calculated out according to the equation (3.*1*), where l and A is the thickness and contact area of the toroid core, V is the measured voltage and I is the measured current.

$$\rho = \frac{VA}{Il} \tag{3.1}$$

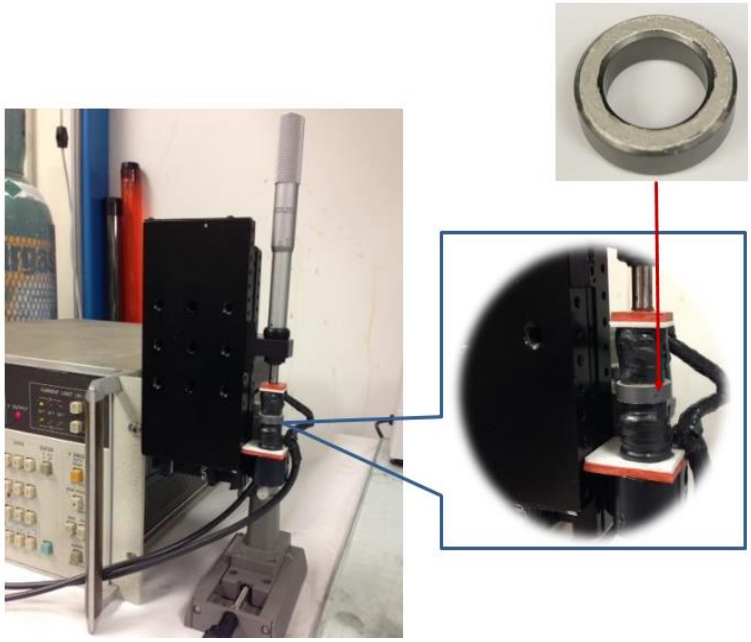

Fig. 3-9. Pico-ammeter/DC voltage source and self-made toroid core sample holder.

- **High Precision Impedance Analyzer —** This apparatus was used to measure complex permeability, including the real part (μ') and the imaginary part (μ"), of the cured cores. Conventionally, magnetic relative permeability is measured by winding wires around

a magnetic core and deriving the effective permeability from its inductance, which is a tedious and time-consuming method. Recall that the intended use of the paste is in power electronics converters, with switching frequencies between several kHz and a few MHz switching frequencies. Thus, in this work, a precision impedance analyzer (4294A; Agilent) featuring a toroid core test fixture (16454A; Agilent) was used to measure the complex permeability of the paste toroid cores (Fig. 3-10). The toroid core in the test fixture becomes an ideal, single-turn inductor, with no flux leakage. Therefore, complex permeability findings can be derived from the measured inductance of the sample loaded fixture. This measurement technique has a wide frequency from 40 Hz to 110 MHz, and the built-in software of the impedance analyzer enables direct readouts of complex permeability.

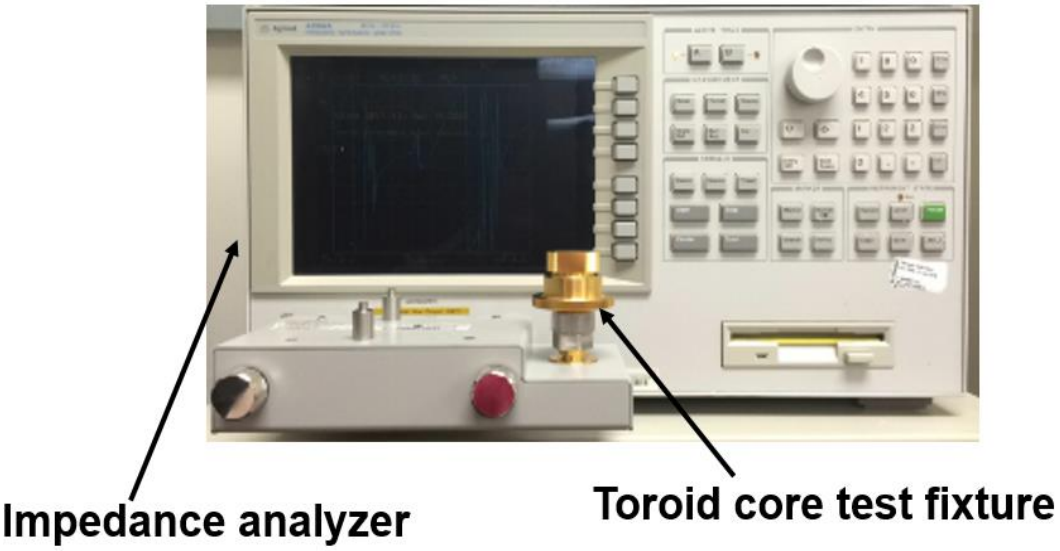

Fig. 3-10. A precision impedance analyzer (4294A; Agilent) with a toroid core test fixture (16454A; Agilent).

- **High Frequency Core-loss Measurement Set Up —** Fig. 3-11 shows the high frequency core-loss measurement developed by the Center of Power Electronic

Systems (CPES). In selecting a core material for use in a power electronics converter, engineers are particularly interested in the material's core loss density or power loss per-unit-volume at usually much higher levels of magnetic fields, which is governed by the switching operations of the converter. Accordingly, the experimental setup utilized herein was designed for this purpose. In order to measure core-loss density, a two-winding method is regarded as the classical method, and thus is widely used [129-132]. This method can minimize measurement errors by excluding data associated with winding loss. However, it has limited sensitivity due to phase discrepancy [133]. One method for overcoming the issue of phase discrepancy is to add a capacitor resonating with the core [134, 135]; but this resonant method requires fine-tuning the resonant capacitor at a given frequency to minimize the winding-loss error. A cancellation method described in the literature [136, 137] combines both the two-winding method and the resonant method; nonetheless, it still requires fine-tuning the cancellation component to lower error from mismatched impedance. In this work, an improved cancellation method was employed [58, 138], which allows for accurate measurement of core-loss density without fine-tuning the cancellation component. We were able to measure each of the core-loss density values at high frequency in a setup that employs a high-power RF amplifier for measurements at high magnetic field excitation.

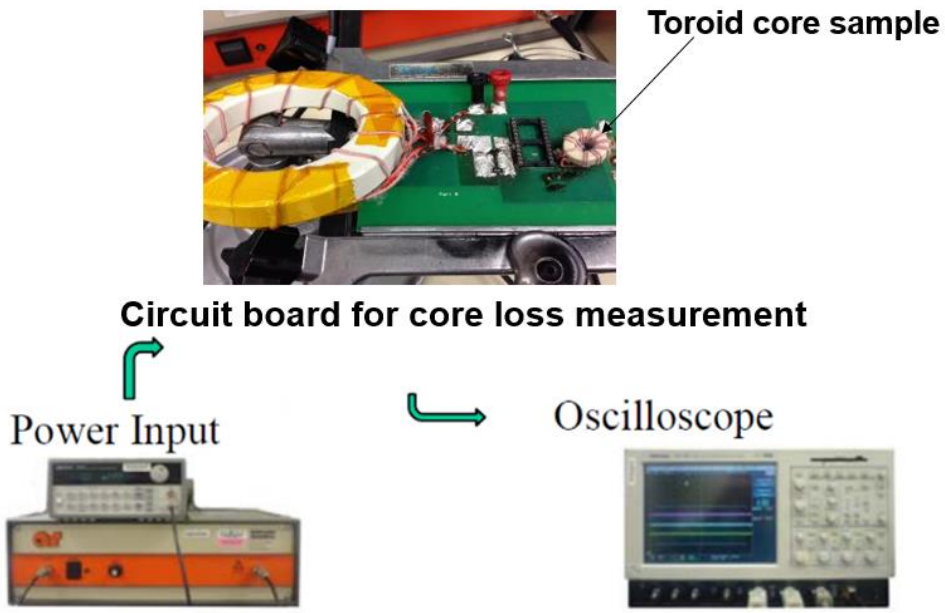

Fig. 3-11. High frequency core-loss measurement developed by the Center of Power Electronic Systems (CPES).

3.4.2. Rheology properties of the pastes

In order to evaluate the processing capabilities of the as-prepared pastes for the AM platform, their rheological properties had to be characterized—including their viscosity behavior as a function of shear rate and viscoelastic behavior:

- **Viscosity vs. Shear Rate —** Fig. 3-12 shows plots of the viscosity of the pastes dependent on the shear rate. All the pastes displayed the shear thinner behavior. Note that for the same magnetic filler loading, the addition of Metglas flakes increases the viscosity of the paste, which is mainly governed by size and shape of filler particles. The reason for the high loading (usually over 60 wt%) is that the filler can modify the rheological behavior of the host polymer due to the fact that the polymer-polymer interactions change to filler-polymer interactions, which reduce the mobility of the polymer [113, 139]. Therefore, a polymer with a significant amount of filler can display much higher viscosity than the pure polymer. When the fillers in the composite are

varied in terms of shape and size, the rheological behavior will become even more complex. The friction between the same fillers, the friction between the different fillers, and the friction between filler and polymer will affect the mobility of the host polymer. The larger specific surface area of the particles, the higher friction force will be obtained between the filler and the polymer. For magnetic pastes, the large surface area of the Metglas flakes can reduce the mobility of the polymer dramatically, and then increase the viscosity of the pastes.

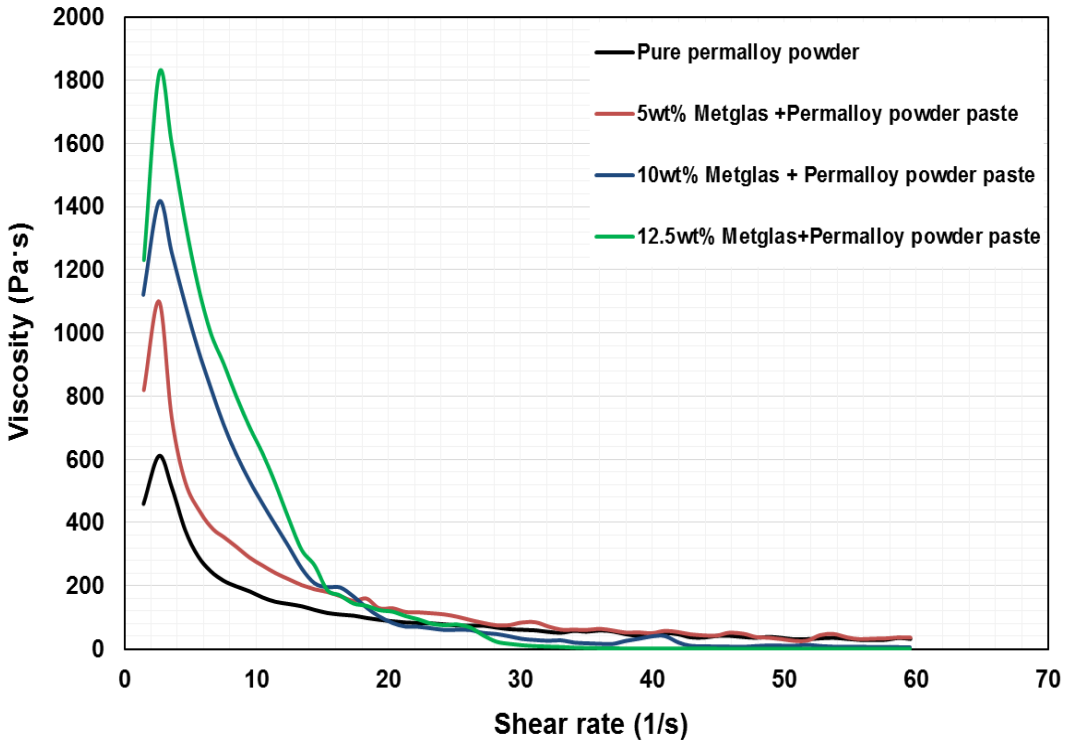

Fig. 3-12. Viscosity of the magnetic pastes dependent on the shear rate.

- **Complex Modulus vs. Angular Frequency —** Fig. 3-13 shows plots of the angular frequency dispersions of the complex modulus obtained for the magnetic pastes. The addition of Metglas flakes can increase both the storage and loss modulus of the pastes. The loss modulus increased much faster than the storage modulus, eventually

approaching the storage modulus. However, it must be noted that none of the pastes exhibited solid-like behavior. Therefore, the magnetic paste will require a layer-by-layer drying approach to form a thick structure during the printing process.

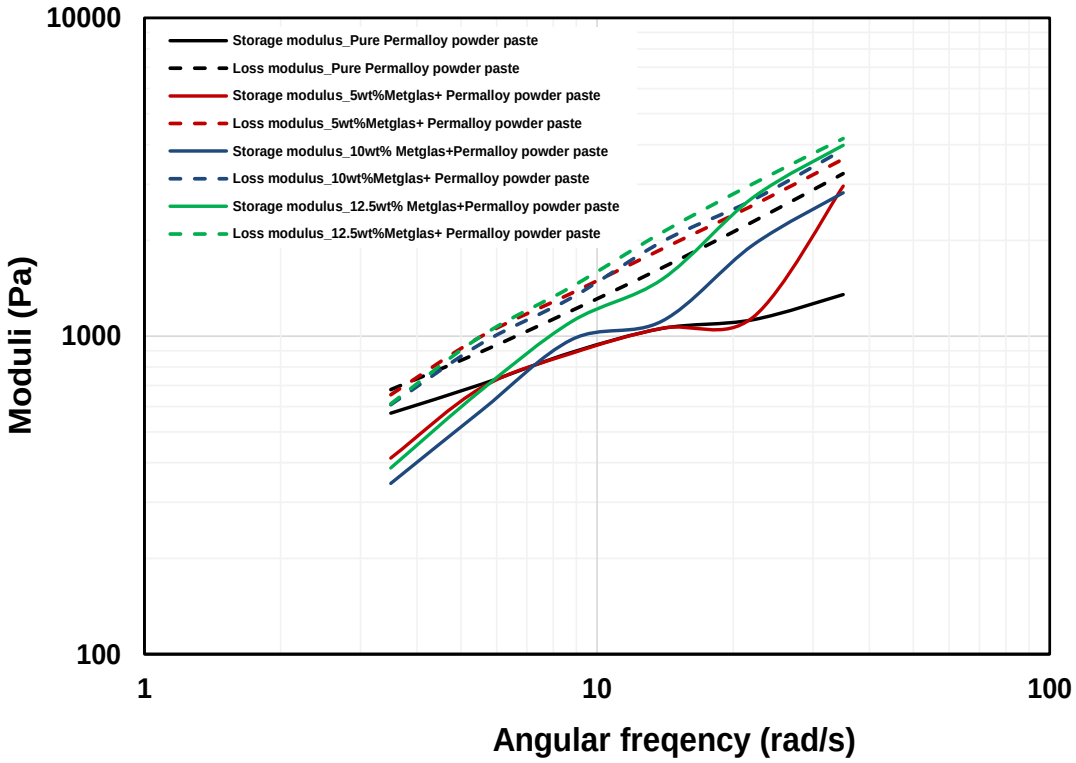

Fig. 3-13. The angular frequency dispersions of the complex modulus of the magnetic pastes.

3.4.3. Properties of the cured cores

One important reason for conducting a thorough characterization of the cured cores from the magnetic pastes is to evaluate the magnetic performance of the pastes for power electronics applications. The primary magnetic properties of interest in this study are the complex permeability and core loss density of the cured cores. Additionally, the DC electrical resistivity of each core was measured, which can indicate the extent of eddy current loss associated with the pastes.

- **Complex Permeability —** Fig. 3-14 illustrates complex permeability dispersion spectra for the BCB-matrix-permalloy core and the BCB-matrix-permalloy-Metglas cores. In contrast to the permalloy-BCB core, which displayed a steady permeability level of 10 beyond 80 MHz, all the other cores containing varying percentages of Metglas flakes had their μ' of permeability starting to fall between 1 MHz and 10-MHz. The composite core with more Metglas addition had a narrower bandwidth due to higher eddy current loss. The μ" of the cores increased with increasing addition of Metglas flakes in the composites. Nevertheless, the addition of Metglas flakes facilitated an increase in the μ' of the composite core, e.g., to 26 at a few MHz with 12.5 wt% Metglas flakes. These findings are consistent with simulation results.

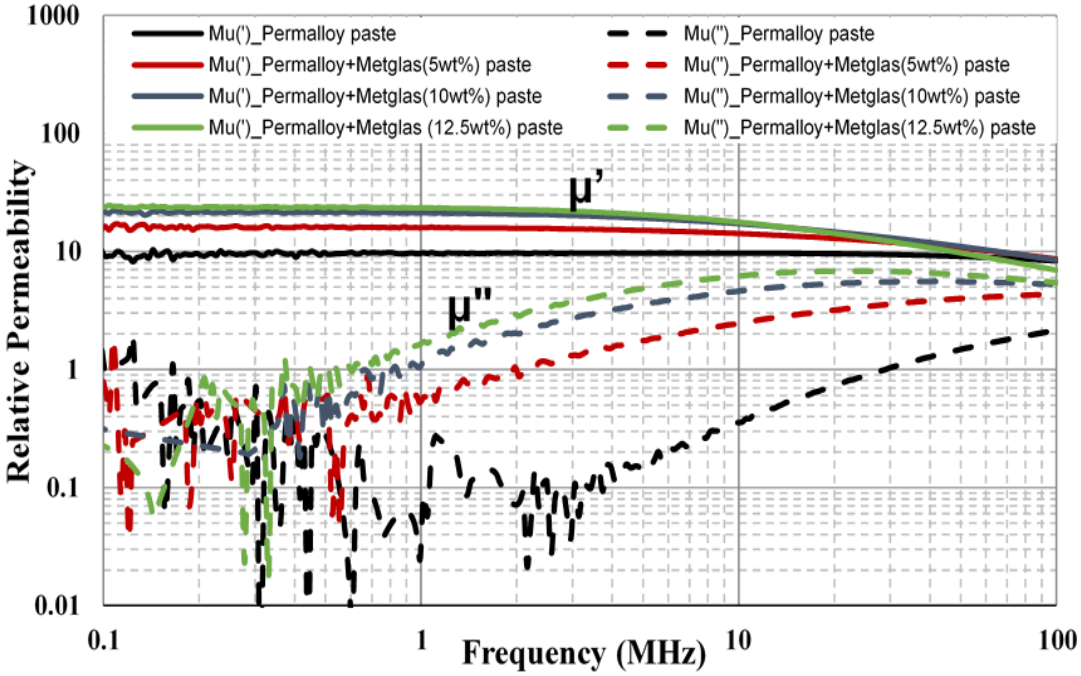

Fig. 3-14. Complex permeability dispersion spectra of BCB-matrix-permalloy core and BCB-matrix-permalloy-Metglas cores.

- **Core Loss Density —** The imaginary parts (μ”) of the complex permeabilities of the magnetic cores shown in Fig. 3-14, which were determined by an impedance analyzer. This technique measure the energy loss mechanisms in the magnetic materials at low levels of alternating magnetic field excitation because of the limited power capability of the instrument. Fig. 3-15 displays the room-temperature core loss density plots of the magnetic cores measured at 1 MHz and 5 MHz at high excited flux density. For each core, the core loss density at 5 MHz was much higher, nearly ten times higher than that at 1 MHz, which is consistent with equation (2.1). The cores with added Metglas flakes exhibited higher core loss density, which also increased with higher Metglas content. This finding is also consistent with the simulation results.

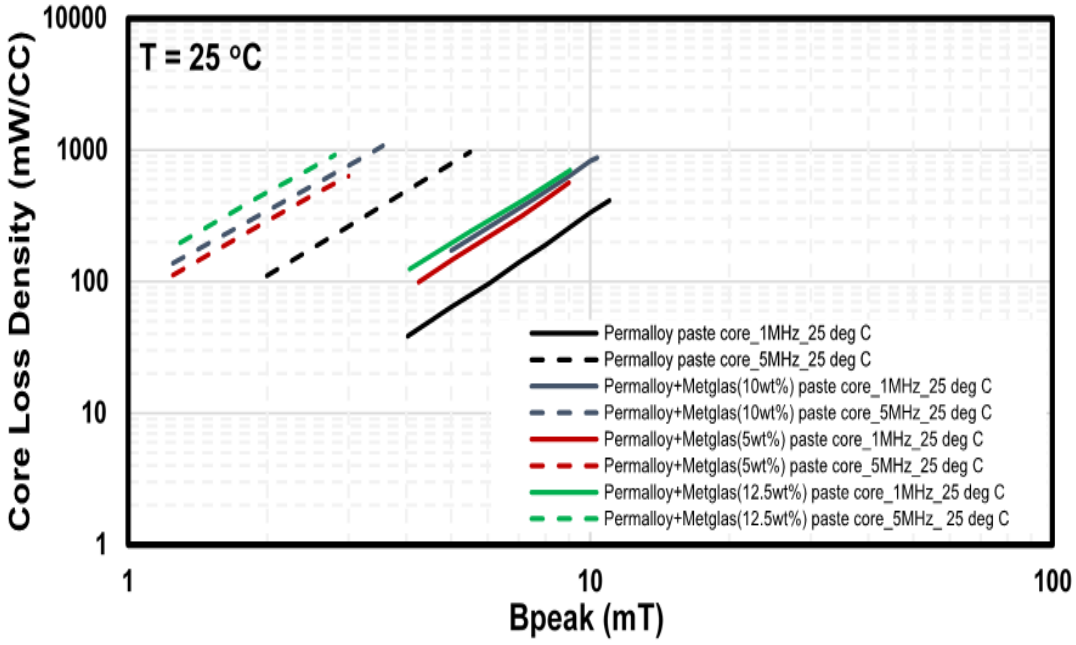

Fig. 3-15. Room-temperature core loss density plots of the fabricated toroid cores measured at 1 MHz and 5 MHz.

- **Bulk DC Electrical Resistivity —** According to equation (3.1), the bulk DC electrical resistivity of all the as-prepared cores were calculated; resulting values were found to be up to 10^7 Ω·cm. The bulk DC electrical resistivity value of the cores is the same order of magnitudes of the soft ferrites.

3.4.4. Microstructure of the cured cores

Shown in Fig. 3-16 (a) and (b) are cross-sectional SEM images of the magnetic cores without and with Metglas flakes, respectively. Fig. 3-16 (c) and (d) show the EDS mappings of the two microstructures, confirming the round particles as permalloy and the flakes as Metglas. The magnetic fillers were well dispersed in the polymer, which means that between the particles there were distributed "air" gaps filled by the polymer, which are depicted as the dark regions in the micrographs. Thus, even though the permalloy and Metglas both feature large low-frequency permeability, the effective low-frequency permeability of the magnetic paste is significantly lower because of the distributed "air" gaps.

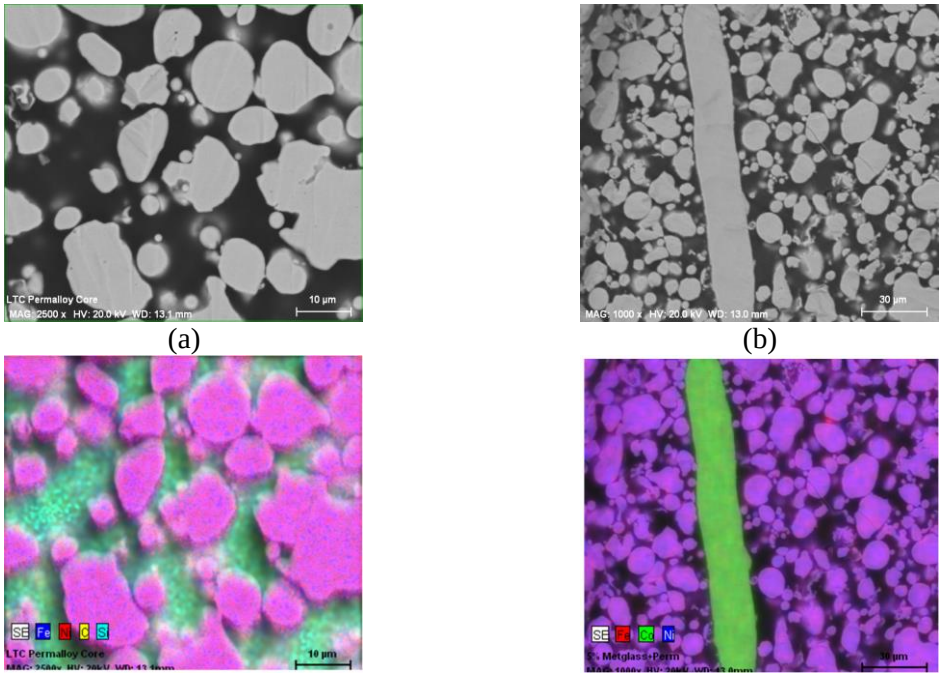

(a) (b)

(c) (d)

Fig. 3-16. Cross-sectional SEM micrographs and EDS mappings of the toroid cores without and with Metglas flakes: (a) core without Metglas flakes; (b) core with Metglas flakes; (c) EDS mapping of the core without Metglas flakes; and (d) EDS mapping of the core with Metglas flakes.

These gaps also serve the role of insulating the electrically conductive magnetic particles. It must be noted, however, that high resistivity magnetic pastes still exhibit high core-loss density when compared with soft ferrite cores. Electrical resistivity values for both the bulk DC of the paste cores and the commercial soft ferrite core, such as 4F1 core [140], are almost the same—specifically, up to 10^7 Ω·cm. In contrast, the core-loss density values for the paste cores were approximately 100 times higher than analogous results for the ferrite cores at 5 MHz at the same excitation flux density.

To explain this phenomenon, the eddy current loss associated with iron-based soft magnetic composites should be investigated. Recall that eddy current losses are caused by eddy currents that are induced in any conductive material by an alternating magnetic flux

[141]. The eddy current losses (W_e) are linearly frequency dependent. It is well known that there are two different paths for eddy currents in soft magnetic composites, as shown in Fig. 3-17 [142]: intra-particle (typical for materials with well insulated particles) and inter-particle (for materials with non-insulated particles).

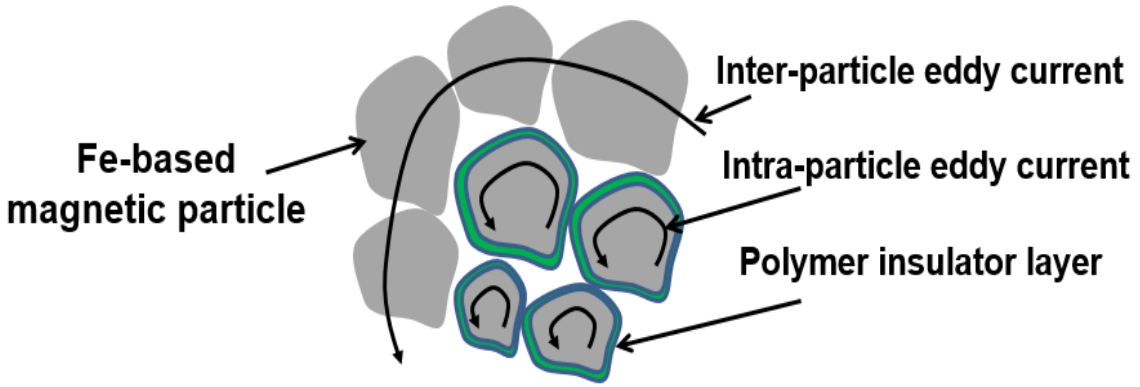

Fig. 3-17. Inter-particle and intra-particle eddy currents in soft magnetic composites.

For the inter-particle eddy current, the paths of the current are concentric curves lying in the cross-section perpendicular to the magnetic induction. The inter-particle eddy current losses p_e^{Inter} can be expressed as equation [143, 144]:

$$P_e^{Inter} = \frac{\pi d_{eff} B_m^2}{\beta \rho_R} f^2 \tag{3.2}$$

where d_{eff} is the effective dimension for eddy current (for bulk material prepared by casting d_{eff} is the thickness of the sample), B_m is the maximum induction, f is the frequency, ρ_R is the specific resistivity and β is the geometrical coefficient of the magnetic filler. Conversely, intra-particle eddy current loss p_e^{Intra} can be expressed as equation (3.3) [145], which for sinusoidal magnetic induction leads to the expression like in equation (3.4) [146].

In equation (3.4), where d is the particle diameter and ρ_R is the specific resistivity of the magnetic filler.

$$P_e^{Intra} = \frac{d^2}{40\rho_R}\left(\frac{dB}{dt}\right)^2 \tag{3.3}$$

$$P_e^{Intra} = \frac{(\pi d B_m)^2}{20\rho_R} f^2 \tag{3.4}$$

Therefore, for the as-prepared magnetic paste, the polymer "gaps" can reduce the inter-particle eddy-current loss. This outcome may partially explain why the permalloy-BCB composite core had a low core loss density at 5MHz. For the composite cores containing Metglas flakes—which were quite large (> 75 μm in length and width) and thick (25 μm), as well as being significantly misaligned to the magnetic field direction —the intra-flake eddy-current loss was still a significant contribution to the core loss density. Therefore, by utilizing thinner flakes and better aligning them to the magnetic field, one would likely achieve a composite with higher relative permeability and lower core loss density.

3.5. Summary

Magnetic pastes with BCB as the adhesive matrix, and permalloy round-shaped particles and Metglas flakes as the magnetic fillers, were designed, formulated and characterized for AM platform and PE integrations. Formulation of the composite material was guided by Maxwell simulation of the finite-element models of the composite. Flowable pastes of the magnetic materials were fabricated by mixing the magnetic fillers with varying amounts of Metglas flakes added to permalloy particles and an organic composition consisting of BCB, organic dispersant, and solvent. The pastes displayed shear

thinner behavior that can be extruded out smoothly by the 3D printer. However, the viscoelastic behavior of the pastes was not solid-like; in other words, it would require a layer-by-layer drying process to form a thick structure during the printing process. Toroid cores were made by drying and curing the pastes at 250^{o}C without hot pressing. The magnetic fillers were uniformly dispersed in the BCB polymer, which served as the "air" gaps between the magnetic particles. These gaps drastically lowered the low-frequency permeability of the paste cores, but also reduced its core loss density at MHz frequencies. The addition of Metglas flakes significantly increased the paste permeability up to several MHz. Because the flakes used in this study were somewhat large and thick, the paste cores with Metglas flakes also displayed higher core-loss density values.

CHAPTER 4. ADDITIVE MANUFACTURING OF MAGNETIC COMPONENTS

4.1. Introduction

As noted in Chapter 1, one potential way to increase power density and simplify the process of fabricating and integrating magnetic components in PE circuits is to use AM technologies to fabricate the magnetics. However, based on the process flow chart, the primary barrier to this approach relates to current manufacturing shortcomings—namely, the lack of compatible and efficient magnetic materials for a printer's feedstock. In response, an approach for developing a low-temperature curable magnetic paste for an AM platform was described in Chapter 2. In Chapter 3, a series of these magnetic pastes was designed, formulated and characterized. The as-prepared pastes are known to be physically compatible with the 3D printer, and the cured paste cores were shown to exhibit desirable magnetic properties for application in the area of power electronics.

As detailed in this chapter, also based on developed the process flow chart was described in Chapter 2, the magnetic components fabricated by a using multi-material paste-extrusion 3D-printer will be demonstrated and characterized. A magnetic paste infused with 12.5 wt% Metglas flakes was used as the magnetic core feedstock for the printer, and a commercial nanosilver paste was used as a conductive winding feedstock for the printer. The extrusion mechanisms of the 3D printer were analyzed to achieve the printed structure with acceptable tolerance. Several inductors featuring a number of structural variations (e.g., planar, toroid, and constant-flux inductors) were designed and fabricated. The properties of as-fabricated magnetic components, including inductance and DC winding resistance, were characterized to prove the feasibility of fabricating magnetic

components via the 3D-printing technology. Microstructures of the 3D-printed magnetic components were characterized by SEM for further improvements in magnetic properties. Both the winding and core magnetic properties can be improved by adjusting the formulation and flow characteristics of the feed paste, as well as by fine-tuning specific printer parameters—such as motor speed, extrusion rate, and nozzle size—as well as by modifying the curing profile in the post-process.

4.2. Structure design of magnetic components

To demonstrate the feasibility of 3D-printing magnetic components, several inductors with different levels of complexity were designed to evaluate the capability of this manufacturing technology.

4.2.1. Planar inductor

Fig. 4-1 shows the planar inductor with simple design: a spiral winding on top of a magnetic plate. This shape is designed for initial evaluation of printing both magnetic and metal pastes, including the basic capability of the 3D printer for processing multi-materials, and the printer's line and layer resolutions. The designed planar inductor had the following dimensions: diameter of the core = 20 mm; thickness of the core = 0.4 mm; winding width = 0.8 mm; winding thickness = 0.2 mm.

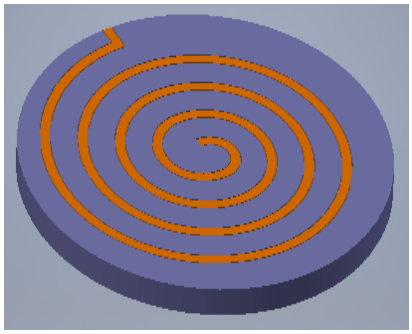

Fig. 4-1. Design of planar inductor for 3D-printing.

4.2.2. Toroid inductor

At present, almost all toroid inductors used in PE circuits are fabricated in a specific way: first by making the cores using a metal casting and/or powder processing, and then combining the cores with a winding of metal traces or wires. To demonstrate that the 3D printer can easily process certain magnetics that are difficult to manufacture using traditional methods, we designed a toroid inductor for later printing. As shown in Fig. 4-2, the inductor has eight turns of winding, with a portion of the winding buried inside the core — with the latter serving as a supporting material during the printing process. The designed toroid inductor had the following dimensions: outer diameter of the core = 20 mm; inner diameter of the core = 12 mm; thickness of the core = 0.6 mm; winding width = 0.8 mm; winding thickness = 0.2 mm.

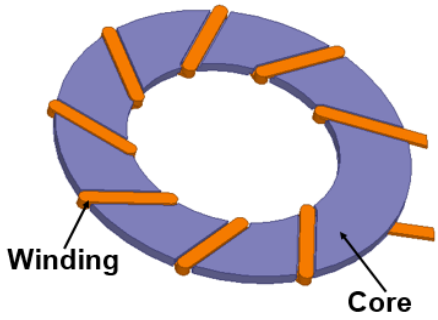

Fig. 4-2. Design of toroid inductor for 3D-printing.

4.2.3. Constant-flux inductor

As indicated in Chapter 1, the “constant-flux” concept is leveraged to achieve high magnetic-energy density, which leads to (a) better utilization of the core material, and (b) a reduction in the volume of the inductor. As illustrated in Fig. 4-3, two versions of the constant-flux inductor were designed for 3D-printing: (a) is configured with spiral

windings embedded in the magnetic core, and (b) is configured with square windings embedded in the magnetic core. Both configurations require precise control of the different widths and space uniformity between each turn of windings. The parameters for these two constant-flux inductor designs are listed in Table 4-1 and Table 4-2, respectively.

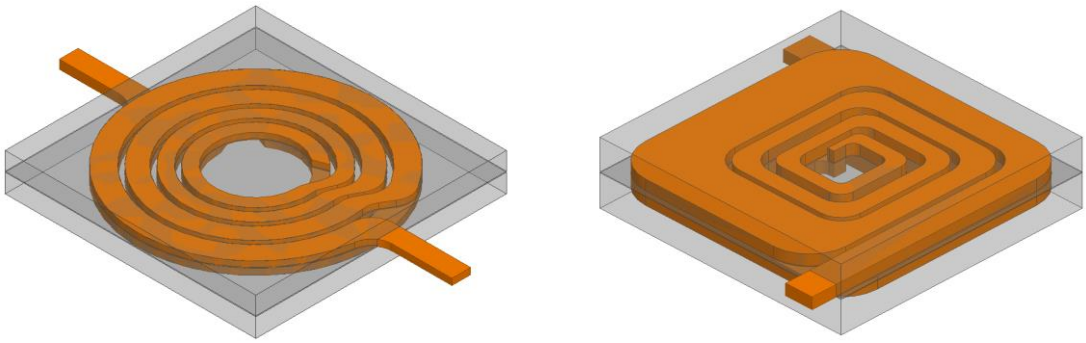

(a) (b)

Fig. 4-3. Geometry of design versions of constant flux inductor with different winding structure: (a) spiral windings and (b) square windings.

Table 4-1. Designed dimensions of constant-flux inductor with spiral windings.

Winding number	Outer radius of winding	Inner radius of winding
j = 1	9.2 mm	7.6 mm
j = 2	7.2 mm	5.8 mm
j = 3	5.4 mm	4.4 mm
j = 4	4 mm	3 mm
Winding space	0.4 mm	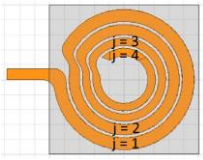
Winding thickness	1 mm	
Core length	20 mm	
Core thickness	4.5 mm	

Table 4-2. Designed dimensions of constant-flux indicator with square windings.

Winding number	Winding width	
j = 1	2.2 mm	
j = 2	1.6 mm	
j = 3	1.2 mm	
j = 4	1 mm	
Winding space 1	0.8 mm	
Winding space 2	0.4 mm	
Winding space 3	0.4 mm	
Winding thickness	1 mm	
Core length	20 mm	
Core thickness	4.5 mm	

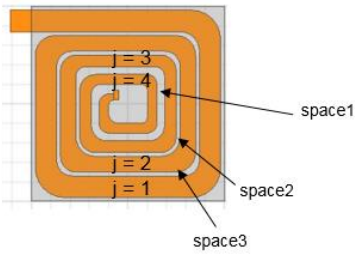

4.3. Fabrication of magnetic components with the 3D printer

The Hyrel System 30M printer is equipped with a lead-screw driven system. The extruder mechanisms of the 3D-printer consist of a plunger driven by a lead-screw connected stepper motor and a syringe. The paste flow is regulated by controlling the plunger movement; it starts (or stops) extrusion by generating (or releasing) force on the plunger. Theoretically, the printer should accommodate any material that can be smoothly extruded out of a syringe for fabrication purposes [147, 148]. In practice, however, the print quality (dimensional accuracy and surface roughness of each layer) depends on printing parameters such as motor speed, extrusion rate, nozzle size, and the rheological properties of the chosen paste material. Therefore, to print magnetic components with acceptable line and layer resolutions, the extrusion mechanisms of the Hyrel 3D printer must be determined before using formulated soft magnetic and commercial nanosilver pastes as the feed materials. Only then can the functional materials be used to fabricate the as-designed magnetic components.

4.3.1. Extrusion mechanisms description

The printing process associated with an extrusion-based printer can be divided into two basic stages: steady-state and transient stages. The steady-state extrusion stage occurs when a continuous filament is being printed at a constant extrusion rate. The transient stage, which includes the material extrusion stage and material retraction stage, occurs when the flowrate changes—usually during the onset and cessation of extrusion [149].

At the start of a print (before the x, y, or both motors begin to move) instructions are given to the extruder to dispense a fixed amount of paste to fill the gap between the syringe nozzle and the build plate, as seen in Fig. 4-4 (a). After the gap is filled, the x, y, or both motors start to move at a speed set by the user, while the extrusion stepper motor is controlled to dispense material at a specified rate that produces a desired print thickness. Fig. 4-4 (b) shows a schematic showing the printing stage. At the end of a printing run, to prevent any dripping of the print material, the extrusion motors follows another set of instructions to retract the excess paste outside of the syringe, as shown in Fig. 4-4 (c).

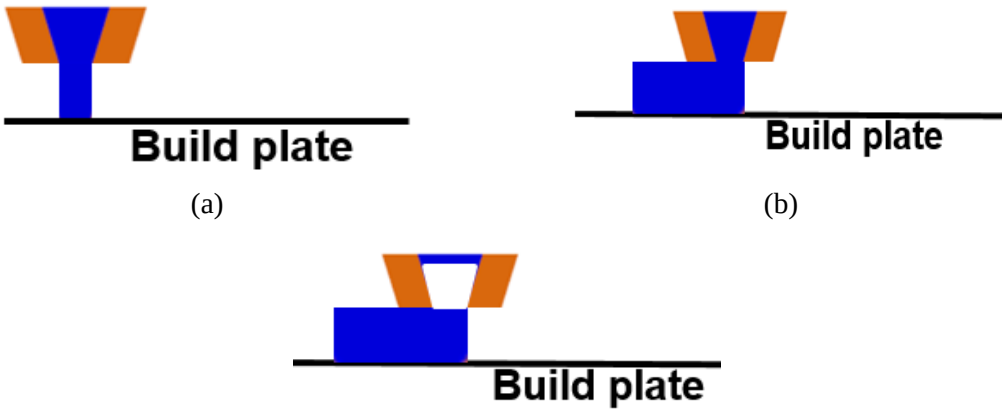

(a) (b)

(c)

Fig. 4-4. Schematic of printing process of an extrusion-based printer: (a) material dispersing in transient start stage; (b) material dispersing in steady-state printing stage; (c) material retraction in transient stop stage.

Proper input of printing parameters during all stages of the printing process are crucial in determining the print quality. Two issues further complicate the process of determining appropriate input parameters: (a) the paste and its container do not strictly form an incompressible system, and (b) the motors have different transient times to turn on and off. To illustrate this point, the relationship between the applied force and time is plotted in Fig. 4-5 for an extrusion motor for a complete printing run. The extrusion force exerted on the paste is likely to rise rapidly from zero to a certain value in a short time period, stabilize at a value during the printing process, and then reverse to a negative value to retract/recapture the paste at the end of a run.

In order to determine the rules for inputting the various parameters during different stages, a theoretical analysis of the printing process was constructed; paste extrusion experiments were also conducted to prove the theory analysis.

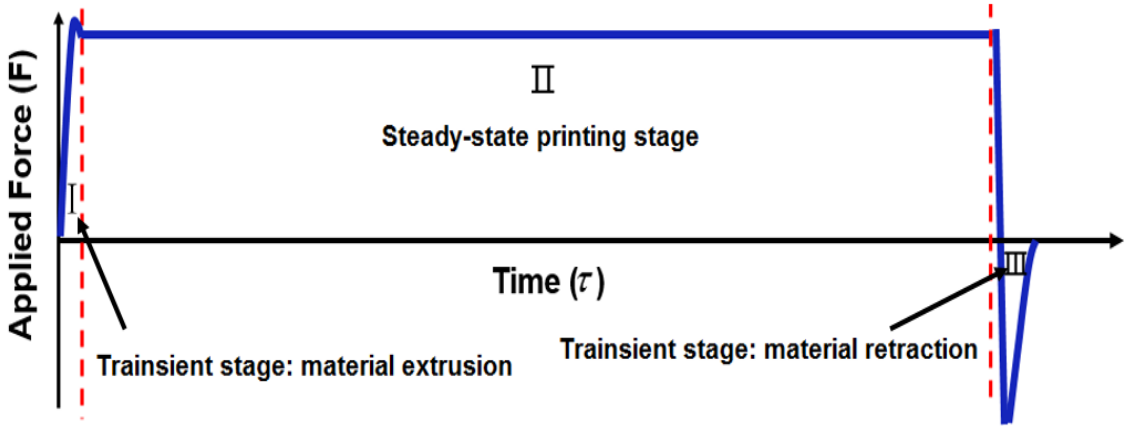

Fig. 4-5. Applied force versus time of extrusion motor from the start to the end of a printing run.

- **Material Extrusion Stage —** In this stage, the only unknown parameter is the moving steps of the extrusion motor system, which applies a force on the dispensing system.

Mathematically, the total volume of the material in the gap can be calculated by the following equation:

$$\pi \times \left(\frac{d_n}{2}\right)^2 \times T_f = Q \times t \tag{4.1}$$

where d_n is the nozzle size and T_f is the first layer thickness, Q is the flow rate of the dispersing system, and t is dispensing time. According to equation (4.1), the dispensing time t can be obtained if the flow rate Q of the dispensing system is known. The step rate ($\dot{s}_t$) of the Hyrel syringe dispensing system in the stationary start stage is a constant. As a result, the moving steps (N) of the dispensing system can be calculated by the following equation:

$$N = \frac{t}{\dot{s}_t} \tag{4.2}$$

Therefore, in order to calculate the dispensing time in the stage, the flow rate must be obtained. In order to proceed, it is assumed that the dispensing of the paste material in the syringe flows in a laminar manner and the paste is an incompressible fluid. According to the Poiseuille's law [150], the flow rate can be expressed by the following equation:

$$Q = \frac{(P(t) - P_0)\pi r^4}{8\eta(t)l} \tag{4.3}$$

Where $P(t)$ and P_0 represent the pressure levels at the two ends of the syringe, r is the radius of the syringe, η is the viscosity of the paste material, and l is the moving distance. As shown in equation (4.3), the flow rate is related to the viscosity of the paste material and the applied force of the lead-screw driver system. However, both the

viscosity of the paste material and the applied force of the lead-screw driver system are functions of time, making the flow rate in the stationary stage indeterminable. The moving steps of the extrusion motor system in the material extrusion stage can only be obtained via a trial-and-error process. Therefore, in this stage, the head effect represents a widespread phenomenon when processing paste materials. As shown in Fig. 4-6, the Hyrel 3D printer was printing the commercial nanosilver paste. The paste was extruded at a high rate at the onset without knowing the exact printing steps, which brings the "head effect" to the printing process.

- **Steady-state Extrusion Stage —** In this stage, the setting parameters are the extrusion width (W_e), the layer thickness (T) and travel speed (ν). For the 10cc syringe dispersing head, one-step movement of the extrusion motor system delivers a constant 0.017mm^3 of material ($V_s = 17 nl/step$). For the Hyrel 3D printer, the step rate ($\dot{s}$) in the steady-state extrusion stage is not a constant. The printer will calculate the $\dot{s}$ automatically based on the input setting parameters. Theoretically, in a certain amount of time, printing a single line on the build plate in the x direction can be expressed by the following equations:

$$\dot{s} \times V_s \times t = W_e \times T \times \nu_x \times t \tag{4.4}$$

$$\dot{s} = \frac{W_e \times T \times \nu_x}{V_s} \tag{4.5}$$

Equation (4.5) demonstrates that the automatically calculated step rate is not related to the material's properties. Therefore, the input parameters dictate how the Hyrel 3D Printer adjusts its step rate in the printing stage to produce the designed structure. As

such, the printing quality in this stage should be much more stable than in the transient stages. However, the inhomogeneity of paste properties, such as the trapped air bubbles in the paste, can be the factor that can cause variations in the steady-state extrusion force for a constant plunger velocity [151]. Fig. 4-7 shows how air bubbles trapped in the paste damaged the printing structure. Therefore, in order to achieve high print quality during this stage, is critical to obtain a homogeneous paste.

- **Material Retraction Stage —** It is during this stage that the moving steps are determined for retracting the material back into the syringe. The number of moving steps for the extrusion motor system in this end stage also requires a trial and error process. Therefore, in this stage, the "tail effect" can be easily found when processing paste materials. As shown in Fig. 4-8, when the Hyrel 3D-printer was retracting the nanosilver paste, "little tails" were left when the syringe raised up.

In summary, the effects of start/stop 3D-printing processes in the transient stages are unpredictable. In contrast, a designed structure that is printed in the steady-state stage with homogeneous paste materials may have a high likelihood of achieving good print quality.

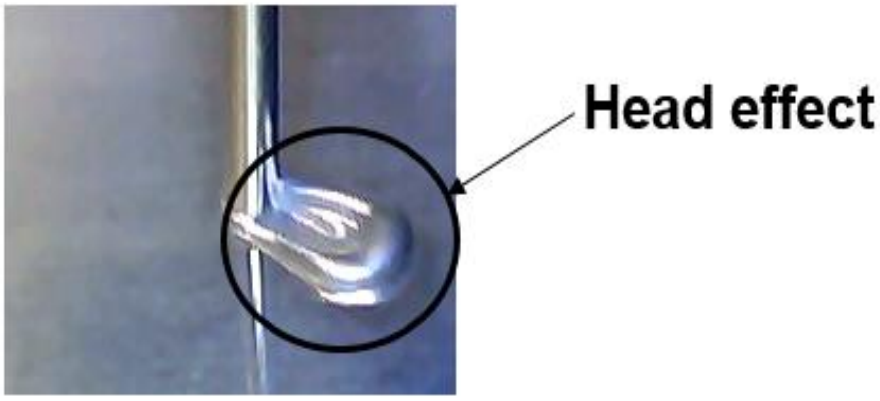

Fig. 4-6. The head effect was generated during the paste printing process.

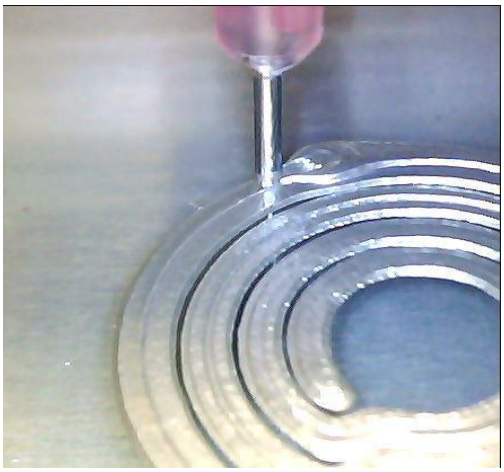

Fig. 4-7. 3D-printing commercial nanosilver paste with trapped air bubbles.

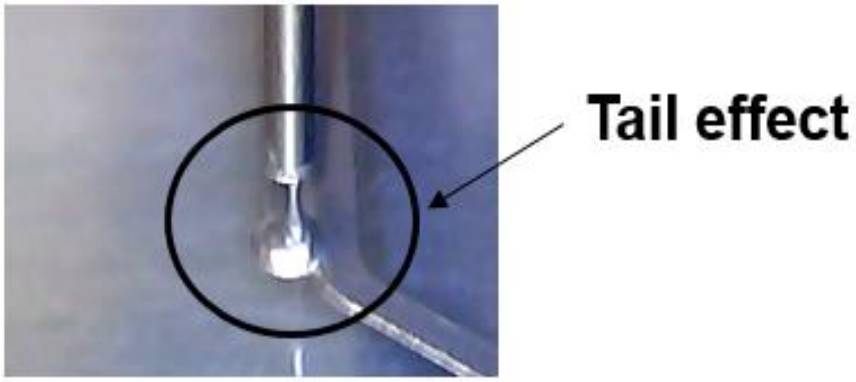

Fig. 4-8. The tail effect was generated during the paste printing process.

4.3.2. Fabrication procedures demonstration

After investigating the extrusion mechanisms of the Hyrel 3D-printer, a magnetic paste with 12.5 wt% Metglas flakes and a commercial nanosilver paste were used to print the as-designed structures for demonstration.

- **Planar Inductor —** Fig. 4-9 shows the process flow for making a 3D-printed planar inductor: (a) printing a magnetic plate layer on the bottom, and a spiral winding on top of the magnetic layer. The thickness of each layer, magnetic or nanosilver paste, was 0.2 mm. During the entire printing process, the build-plate temperature was set at 70^{o}C.

After the structure was printed, it was transferred to a programmable muffle furnace to simultaneously cure the polymer in the magnetic core and sinter the nanosilver winding. The curing profile is shown in Fig. 4-9 (b). Fig. 4-9 (c) illustrates the finished 3D-printed planar inductor. The printed planar inductor had the following dimensions: diameter of the core = 19.75 mm; thickness of the core = 0.38 mm; average winding width = 0.88 mm; average winding thickness = 0.19 mm. The printed dimensions are within 10% error than those of the designed structure. The planar inductor was designed just for testing the compatibility of the two pastes. The head and tail effects in the spiral windings can still be seen in the printed inductor. The print quality of the structure can be further improved by printing the total winding part in the steady-state stage.

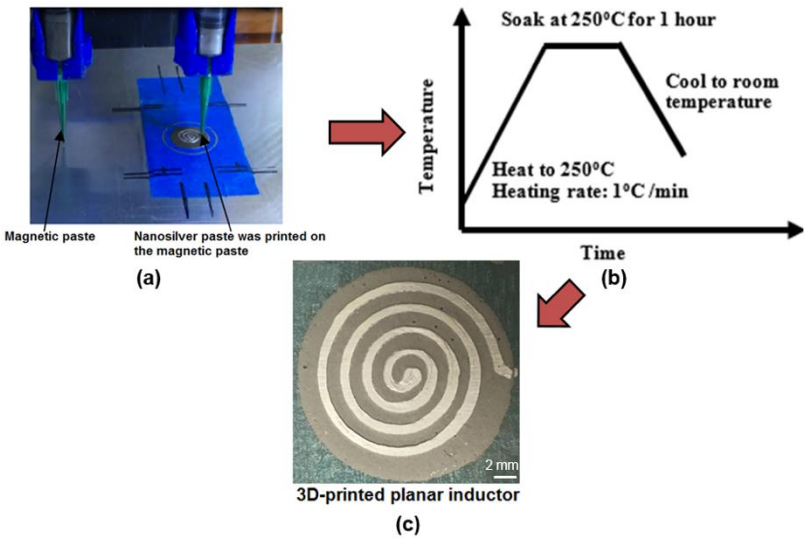

Fig. 4-9. Process of 3D-printing planar inductor.

- **Toroid Inductor —** As mentioned previously, a printing process conducted completely in the steady-state stage may be more conducive to achieving high print-quality. However, some of the structures may be hard to print in the steady-state stage

due to design considerations using multi-material printing in one layer requirement, and the required toroid inductor—which may subsequently require polishing during the post-process. Fig. 4-10 shows the process flow for making a 3D-printed toroid inductor: (a) insertion of the two-paste feedstock, the magnetic and nanosilver paste; (b) printing of a base layer of the magnetic paste with gaps left for winding; (c) the base layer with the silver winding printed to fill the gaps; (d) printing of two more layers of the magnetic paste to achieve a designed thickness; (e) final deposition of the nanosilver paste to connect the winding on the base layer to the top. The thickness of each layer, magnetic or nanosilver paste, was 0.2 mm. During the entire printing process, the build-plate temperature was set at 70^{o}C. After the structure was printed, it was transferred to a programmable muffle furnace to simultaneously cure the polymer in the magnetic core and sinter the nanosilver winding. The curing profile is shown in Fig. 4-10 (f). After curing, the sample had to be polished to eliminate the "tail effect" on the silver connection part. Fig. 4-10 (g) shows the finished 3D-printed toroid inductor after polishing.

The printed toroid inductor had the following dimensions: outer diameter of the core = 19.8 mm; inner diameter of the core = 12.2 mm; thickness of the core = 0.55 mm; average winding width = 0.88 mm; average winding thickness = 0.18 mm. The printed dimensions are within 10% error in comparison to the designed structure.

However, the printed quality of the toroid inductor is not sufficiently high. The tail and head effects can apparently be isolated to the winding connection parts. To further improve the print quality of the toroid inductor, the rheological properties of both the pastes must be modified. The storage modulus should be larger than the loss modulus

of the pastes, which will make the pastes more easily shaped for filamentary printing. Currently, the pastes are still fluid-like, which make the head and tail effects more apparent.

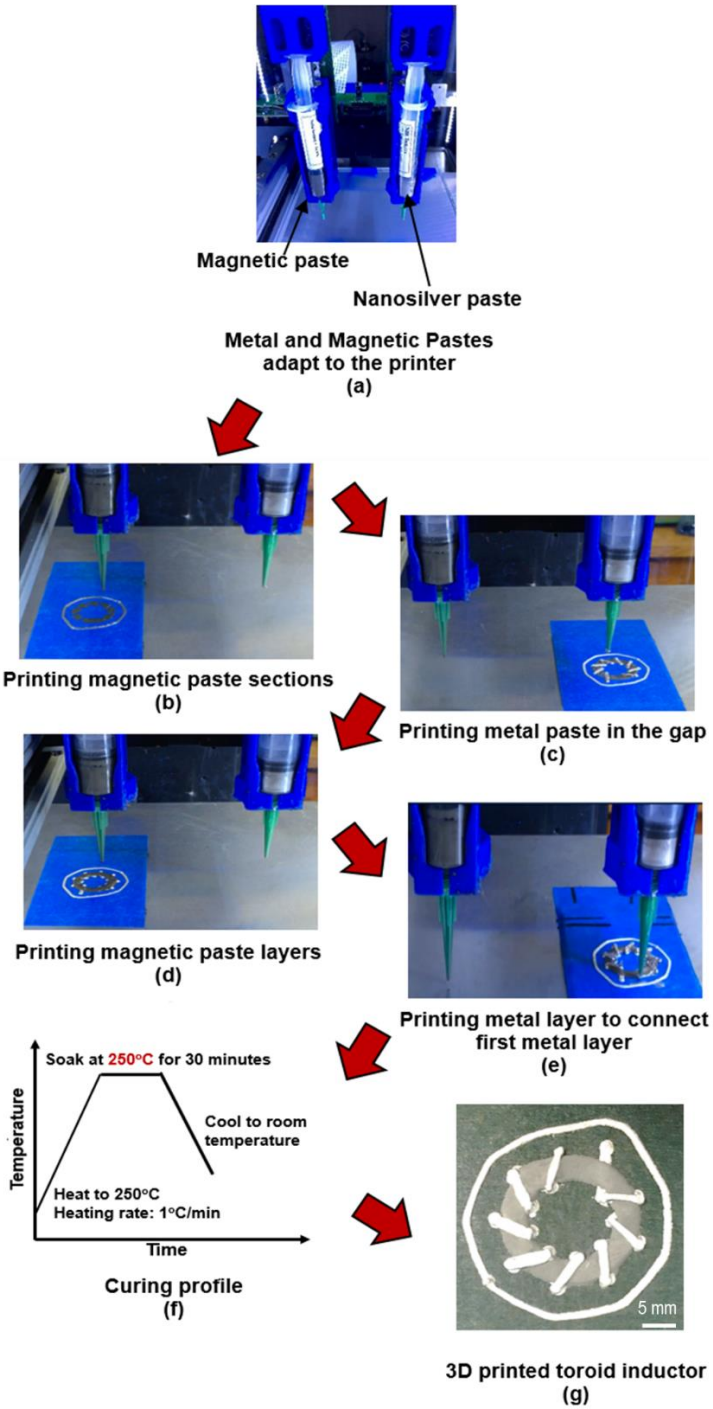

Fig. 4-10. Process of 3D printing a toroid inductor.

- **Constant-flux Inductor —** The accuracy of the winding structures is a key factor in forming constant-flux inductors. Therefore, a viable strategy for fabricating these inductors is to use a 3D printer to fabricate the winding part, and then utilize injection molding to form the core part. A "dump area" is created to avoid any adverse impacts from transient stages, which allows the designed winding structures to be printed entirely in the steady-state stage. Fig. 4-11 (a) and (b) shows the 3D-printed half pieces of spiral and square windings for the constant-flux inductors, respectively. After creating the "dump area," the printed windings did not show any stop/start extrusion effects in the designed part. The dimensions of the printed spiral and square windings are shown in Table 4-3 and Table 4-4, respectively, which are within 10% error than that of the designed winding structures.

(a)

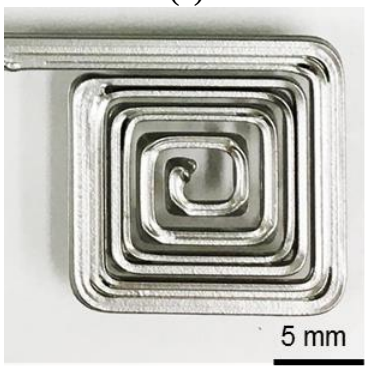

(b)

Fig. 4-11. 3D-printed (a) spiral windings and (b) square windings for constant-flux inductor.

Table 4-3. Dimensions of 3D-printed spiral windings for constant-flux inductor.

Winding number	Outer radius of winding	Inner radius of winding
j = 1	9.1 mm	7.7 mm
j = 2	7.2 mm	5.9 mm
j = 3	5.3 mm	4.2 mm
j = 4	4 mm	3 mm
Winding space	0.35 mm	
Winding thickness	0.6 mm	

Table 4-4. Dimensions of 3D-printed square windings for constant-flux inductor.

Winding number	Winding width
j = 1	2.3 mm
j = 2	1.7 mm
j = 3	1.25 mm
j = 4	1.1 mm
Winding space 1	0.7 mm
Winding space 2	0.35 mm
Winding space 3	0.35 mm
Winding thickness	0.6 mm

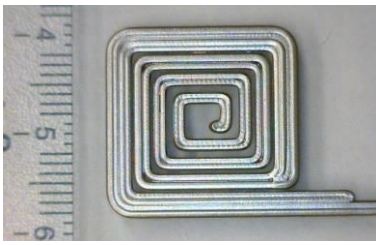

After the winding structures were fabricated in the printer, they were sintered in a programmable muffle furnace based on the sintering profile shown in Fig. 4-12. The sintering temperature was set to 350^{o}C, which is 100^{o}C higher than the preferred temperature (250^{o}C). The reason for this elevated temperature is to achieve a higher

density of windings, thereby reducing the winding resistance of the inductors. In addition, fabricating the magnetic part will utilize the injection molding method, so the high sintering temperature for the windings will not affect the final integration procedures of these inductors. The dimensions of the sintered windings are listed in Table 4-5 and Table 4-6, which are within 20% error compared to those of the designed structures. The sintered windings were polished to be the same thickness as the designed structures—namely 0.5 mm. Two half pieces of sintered windings were soldered together with 60 μm kapton tape as insulator to form the two full size windings, which are shown in Fig. 4-13.

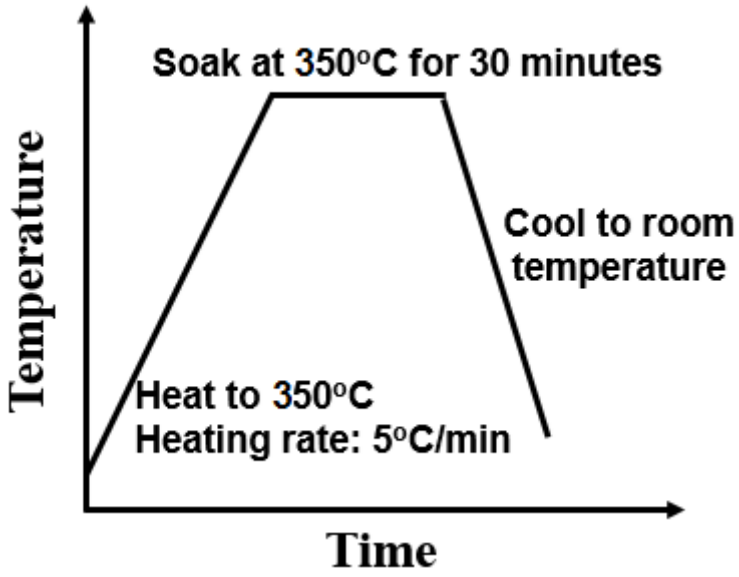

Fig. 4-12. Sintering profile for 3D-printed winding structures.

Table 4-5. Dimensions of 3D-printed spiral windings for constant-flux inductor after sintering

Winding number	Outer radius of winding	Inner radius of winding
j = 1	9.3 mm	7.9 mm
j = 2	7.3 mm	6.4 mm
j = 3	5.0 mm	4.4 mm
j = 4	4.2 mm	3.1mm
Winding space	0.3 mm	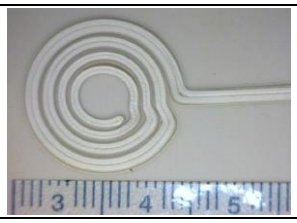
Winding thickness	0.5 mm	

Table 4-6. Dimensions of 3D-printed square windings for constant-flux inductor after sintering

Winding number	Winding width	
j = 1	2.1 mm	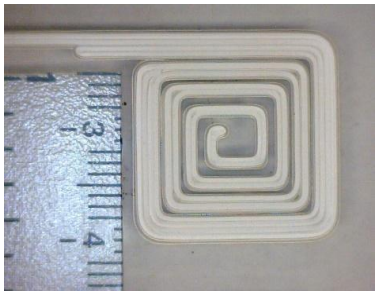
j = 2	1.5 mm	
j = 3	1.1 mm	
j = 4	0.9 mm	
Winding space 1	0.68 mm	
Winding space 2	0.32 mm	
Winding space 3	0.32 mm	
Winding thickness	0.5 mm	

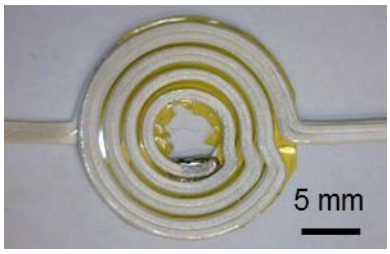

(a)

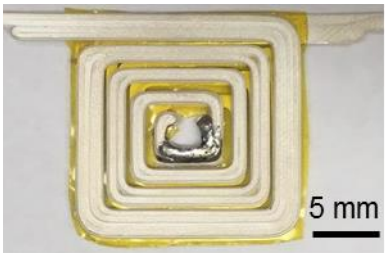

(b)

Fig. 4-13. Full size (a) spiral windings and (b) square windings for constant-flux inductor.

The windings were inserted into the mold for injection molding. The magnetic paste with 12.5 wt% Metglas added was used to fabricate the inductors. The as-fabricated constant-flux inductors are shown in Fig. 4-14. The finished inductors were polished to achieve the same dimensions as designed structures—a core length of 20 mm, and a core thickness of 4.5 mm.

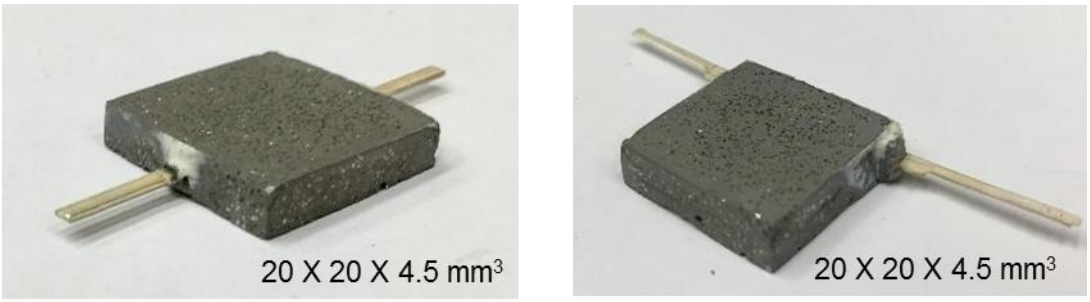

(a) (b)

Fig. 4-14. Constant-flux inductor fabricated assisted by 3D-printing technology: (a) constant-flux inductor with spiral windings and (b) constant-flux inductor with square windings.

4.4. Characterization of additive manufactured magnetic components

In order to evaluate the performance of the 3D-printed magnetic components, two key properties of the printed inductors—namely, inductance and DC winding resistance—were characterized. Additionally, the microstructures of the 3D-printed magnetic components were characterized by SEM for further improvement of magnetic properties.

4.4.1. Inductance and DC winding resistance

For all the 3D-printed magnetic components, FEA was used to simulate its inductance and DC winding resistance. In the FEA simulation, the winding electrical conductivity was set to be three times higher than that of the bulk silver. The relative permeability of the magnetic material used in the simulation was 26. This value was based on the

measurements of the material's complex permeability in the frequency range of 1 KHz to 3 MHz. A high precision impedance analyzer was used to characterize the properties of all the 3D-printed inductors.

Listed in Fig. 4-7 are the measured and simulated inductance and DC winding resistance values for the 3D-printed inductors. The inductance values for all the printed samples at the lower frequency (10 KHz) are in good agreement with simulated results—within 5% error. The measured DC winding resistance values for all the inductors are slightly higher than those obtained via simulation, which is likely due to the contact resistance between the measurement probes and the printed silver.

Table 4-7. FEA simulated and measured inductance at 10 KHz and DC winding resistance of 3D-printed planar, toroid, and constant-flux inductors

Inductance	**FEA simulated**		**Measured**	
	L(nH)	**R_{DC}(mΩ)**	**L(nH)**	**R_{DC}(mΩ)**
	180	115	170	130
	160	80	167	100
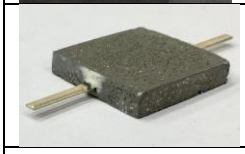	4850	12.5	6250	19
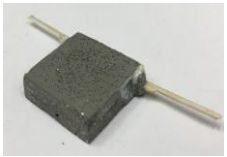	2550	9.86	2500	18.5

4.4.2. Microstructure characterization

It is well known that properties of a material are determined by its microstructure. Examination of the microstructure of the 3D-printed magnetic components can help provide insights for ways to improve magnetic properties. Take the toroid inductor as an example: Fig. 4-15 is a SEM image of the 3D-printed toroid core. The sintered winding is partially densified. One can see the magnetic fillers and voids. The voids, likely created by trapped air bubbles in the magnetic paste, lowered the relative permeability of the core. The other reason for the low relatively permeability is likely due to the random distribution of the Metglas flakes in the sample.

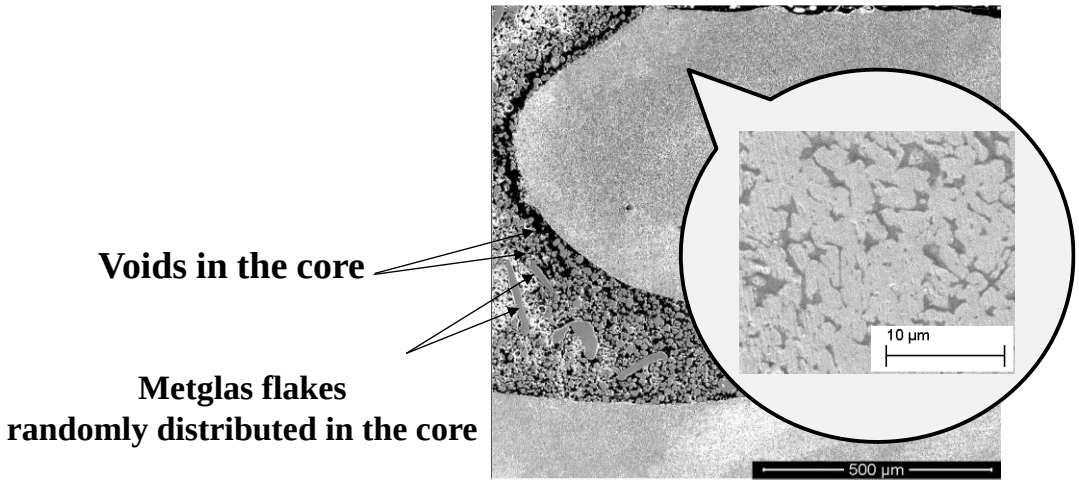

Fig. 4-15. Scanning electron microscope image of the 3D-printed toroid inductor.

Based on our microstructure characterization results, a few approaches are suggested for improving the performance of the printed inductor. For example, the curing profile can be optimized to reduce the void content in the magnetic core and thus increase relative permeability. Aligning the Metglas flakes along the magnetic flux direction can also increase relative permeability [152]. To effectively reduce core-loss density, thinner Metglas flakes should be utilized, which should then be aligned along the flux direction.

To reduce winding loss, either laser- or microwave-assisted sintering techniques can be explored to further densify the sintered microstructure of the printed metal.

4.5. Summary

The feasibility of additive manufacturing of magnetic components by printing both the magnetic core and conductive winding using a commercial multi-extruder paste-extrusion 3D printer was demonstrated. A BCB-matrix-permalloy-Metglas paste, featuring a relative permeability of 26 after curing at 250^{o}C, was used for the magnetic feedstock. This formulation makes it possible to simultaneously cure the magnetic paste and sinter a nanosilver paste, which was used as a feedstock for the winding.

Planar, toroid, and constant flux inductors were designed. In order to facilitate the 3D-printing of the as-designed structures, different fabricating procedures were developed. All of these designed inductors were 3D-printed and characterized for their key properties—most notably inductance at a frequency of 10 KHz, and DC winding resistance. The measured inductance values of all the printed inductors were in good agreement with those simulated by a FEA of the inductor models. For the DC winding resistance measurement, we confirmed that contact resistance between the measurement probes and the printed silver can impact measurement results. The microstructures of the printed inductors were characterized. Results indicate that defects in the printed components should be eliminated to further improve the performance of the 3D-printed magnetic components.

CHAPTER 5. CONCLUSIONS AND FUTURE WORK

5.1 Conclusions

In an effort to increase the power density and simplify the fabrication and integration processes of magnetic components, an additive manufacturing process for fabricating the magnetic components was explored. A process flow chart of 3D-printing magnetic components was developed to guide the research progress. After assessing the known 3D-printing technologies, paste-extrusion was identified as the approach sufficiently flexible to process functional materials in paste form. As such, it became the selected equipment for the fabrication process in this investigation. Currently, the most significant barrier preventing the application of the 3D-printing technology in fabricating power magnetics is that no compatible and efficient magnetic paste has been identified for this platform—thus reinforcing the need to develop a compatible magnetic paste. Based on a literature survey suggesting that a composite made up of soft magnetic particles and a polymer binder in paste form could achieve desired magnetic properties, a series of low-temperature, curable, magnetic pastes were designed, formulated and characterized. The feasibility of 3D-printing magnetic components was demonstrated in this work. This report also describes the essential magnetic properties of these composites, including relative permeability and core-loss density. The principal conclusions of this investigation are summarized in the following sections.

5.1.1. Developing process flow chart of 3D-printing magnetic components

In order to apply the AM technology in processing magnetic components, a process flow chart of 3D-printing magnetic components was developed to guide the progress of

this investigation. Specifically, this research entailed (a) identifying a 3D printer capable of processing multi-materials, (b) selecting metal and magnetic materials for the printer's feedstocks, (c) preparing the materials for the feedstocks, (d) demonstrating the feasibility of 3D-printing magnetic components, and finally, (e) characterizing the 3D-printed magnetic components. This process flow chart can be used as a general reference in any other research area targeting the utilization of AM technology in fabricating functional parts.

5.1.2. Developing low-temperature curable magnetic pastes

Several low-temperature (<250^{o}C), curable, soft magnetic pastes—specifically, Permalloy-BCB paste and Permalloy-Metglas flakes-BCB paste—were formulated for the 3D printer based on the guidance FEA modelling and Maxwell simulation. The pastes consisted of 10 wt% BCB and 90 wt% magnetic fillers—the latter containing varying amounts of Metglas from 0 to 12.5 wt%. The rheological, electrical, and magnetic properties of the magnetic pastes were characterized.

All the pastes displayed shear thinning behavior and were compatible with the AM platform. However, the viscoelastic behavior of the pastes did not resemble that of a solid, indicating that they require layer-by-layer drying to form a thick structure during the printing process. The rheological properties of the pastes were shown to be sensitive to the addition of the Metglas flakes, in that the paste with higher content of Metglas flakes exhibited higher viscosity—more closely approximately that of a solid. The large specific area of the Metglas flakes was considered significant in increasing the friction between the polymer and fillers, thereby reducing the mobility of the host polymer.

The magnetic pastes were cured and then characterized for their key properties. For

example, bulk DC electrical resistivity increased to 10^7 Ω·cm due to the presence of magnetic fillers well encapsulated by the polymer binders. The relative permeability increased with Metglas addition, reaching a value of 26 at 12.5%. However, the core loss data at 1 MHz and 5 MHz showed that the addition of Metglas flakes also increased the core loss density. These characterization data indicate that these magnetic paste composites can be developed for AM platform and PE applications by adjusting their composition, filler properties, and binding properties.

5.1.3. Additive manufacturing of magnetic components

Several inductors with different structural complexities, such as planar, toroid, and constant-flux inductors, were designed to demonstrate the feasibility of fabricating magnetic components by 3D printing technology. By analyzing and understanding the extrusion mechanisms of the Hyrel 3D printer, the as-designed magnetic components were fabricated by utilizing the as-prepared magnetic paste and a commercial nanosilver paste. The dimensions of all the 3D-printed magnetic components were within 20% error when compared to designed structures. Additionally, measured inductance and DC winding resistance findings fell within 10% error in comparison to analogous data for predicted simulations. The microstructures of the 3D-printed magnetic components were characterized by SEM. The trapped air bubbles during paste preparation and/or the printing process, coupled with the random distribution of Metglas flakes, proved to be disadvantageous to the relative permeability of the 3D-printed core part. The partially sintered winding structure should be improved for high frequency applications.

5.1.3. Core-loss mechanisms understanding of the magnetic pastes

Despite the fact that the as-prepared magnetic pastes were shown to be compatible with the 3D-printer, their core-loss properties still need to be improved. The magnetic fillers were well dispersed in the polymer, indicating the presence of distributed "air" gaps between the particles that served to insulate the electrically conductive magnetic particles. Therefore, the bulk DC resistivity of the cured magnetic paste core was calculated to be as high as to 10^7 Ω·cm, which is analogous to commercial soft ferrites. However, the high resistivity magnetic paste still exhibited over 100 times higher core-loss density when compared with soft ferrite cores at high frequency at the same excited flux density.

The intra-eddy current, principally due to the presence of thick Metglas flakes, was considered the reason for the high core-loss of the cured paste cores. For the as-prepared magnetic paste, the polymer "gaps" were shown to reduce the inter-particle eddy-current loss. However, the flakes used in this study were large (> 75 μm in length and width) and thick (25 μm), and were significantly misaligned to the magnetic field direction; nonetheless, the intra-flake eddy-current loss was still a significant contributor to core loss density. Therefore, by using thinner flakes and better aligning them to the magnetic field, it is expected that one could achieve a composite with higher relative permeability and lower core loss density.

5.2. Proposed future work

5.2.1. Altering magnetic and rheological properties to modify magnetic pastes

Currently, the developed magnetic pastes show some promising properties, including low-temperature processability without any external pressure and compatibility with the AM platform and metal paste. These attractive features enhance their potential for use in high frequency power electronics integration. In contrast, the magnetic and rheological properties of the low-temperature curable magnetic pastes can be further improved in following aspects:

- Using thinner or smaller magnetic particles to adjust rheological properties, including viscosity and viscoelastic properties, and further suppress the loss properties of the pastes.
- Selecting other polymer binders or modifying the curing profile to improve the shape-ability and control the void content in the cured magnetic core in order to be more compatible with metal pastes.

5.2.2. Modifying the electrical properties of metal pastes

It should be recognized that the need to drastically reduce the winding resistivity of 3D-printed magnetic components has a range of practical applications. Researchers in additive manufacturing are actively pursuing ways to increase the electrical conductivity of 3D-printed metals. One possible way is to use laser-assisted sintering [153]. In this technique, a laser system is added to a 3D printer. By directing a focused laser beam on the metal as it is being printed, the material can be heated locally to a high temperature to speed up the consolidation of the metal particles, ultimately resulting in higher electrical

conductivity. The local heating prevents possible adverse impacts on the printed magnetic material. Another way to improve electrical conductivity is via microwave-assisted sintering. Using this approach, all the printed parts are heated in an oven using both conventional heat and a microwave. By adjusting the microwave frequency to maximize its absorption by the metal, the metal winding can be heated over a short period of time to a much higher temperature than the magnetic material. Both of these techniques can be explored in future studies to increase the winding conductivity of the sintered nanosilver paste.

5.2.3. Reliability evaluation

Reliability describes the ability of a system or component to function under stated conditions for a specified period of time. The reliability performance of power electronic systems imposes huge challenges in various emerging applications. Currently, both magnetic and metal pastes can be processed simultaneously by a 3D printer. In order to apply this technology more broadly in industry, however, the reliability of the 3D-printed magnetic components must be evaluated. Toward that end, the passive temperature cycling method can be utilized to evaluate the reliability of the printed components. After temperature cycling, the electrical and magnetic properties and microstructure of the parts should all be characterized for enhanced performance.

5.2.4. 3D-printing magnetic components in power converter

Viable demonstrations of the use of a 3D-printed inductor in power converter systems will be essential for advancing this area of research and manufacturing. For this purpose, it is suggested that a prototype of a buck converter be designed, with the goal of integrating

3D-printed magnetic components in it. The power density and efficiency of the converter could then be investigated and characterized.

APPENDIX A – HYREL 30M PRINTER PROCESSES SILICONE PASTES

A-1. Introduction

In theory, a Hyrel System 30M printer equipped with extruding syringes allows users to print any material that can be extruded out of a syringe. Based on the analysis of the mechanisms of the printer in the steady-state stage, the print quality is not related to the material's properties. In the transient stages, however, material properties (e.g., viscosity) will affect print quality. Therefore, in order to confirm the veracity of the analysis of the extrusion mechanisms for the Hyrel paste-extrusion 3D printer, silicone pastes, which are low cost and availability of diverse colors and viscosities, were selected for this experimentation.

A-2. Silicone pastes

Three kinds of silicone pastes with different colors (red, blue and black) and viscosities are used to determine the print quality. Fig. A-1 shows the viscosity (η) measurements of the silicone pastes under different shear rates ($\dot{\gamma}$).

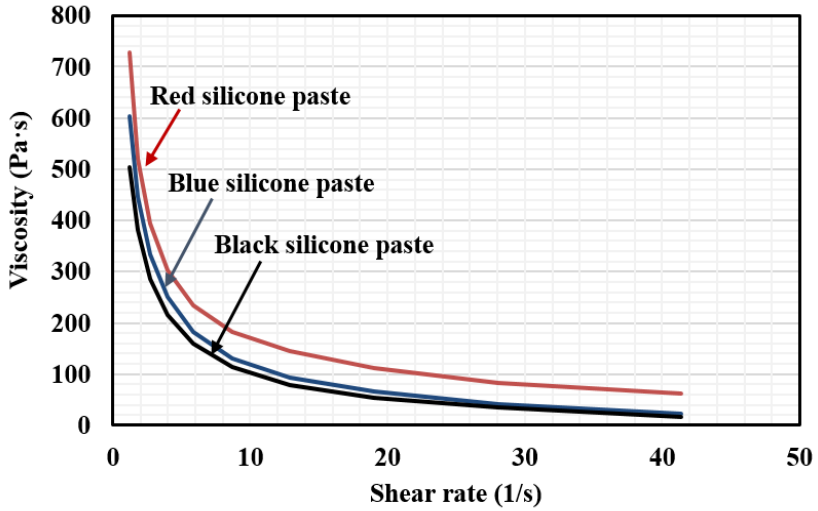

Fig. A-1. Viscosity measurement of silicone pastes under different shear rate.

A-3. Effects of viscosity on print quality in different printing stages

A-3.1. Material extrusion and retraction stages

For materials with different viscosities, the moving steps of extrusion and retraction stages should be different to achieve acceptable print quality. Fig. A-2Fig. A-2 shows an example of printed structures with unacceptable (a) and acceptable (b) print quality. To prove this analysis, the correct moving steps of processing different silicone pastes in both extrusion and retraction stages were determined by using trail-and-error methods. Table 2 lists the moving steps of the extrusion motor system in both the extrusion and retraction stages for silicone pastes with varying viscosities. The silicone paste with higher viscosity will need more moving steps to extrusion or retraction materials for achieving acceptable print quality.

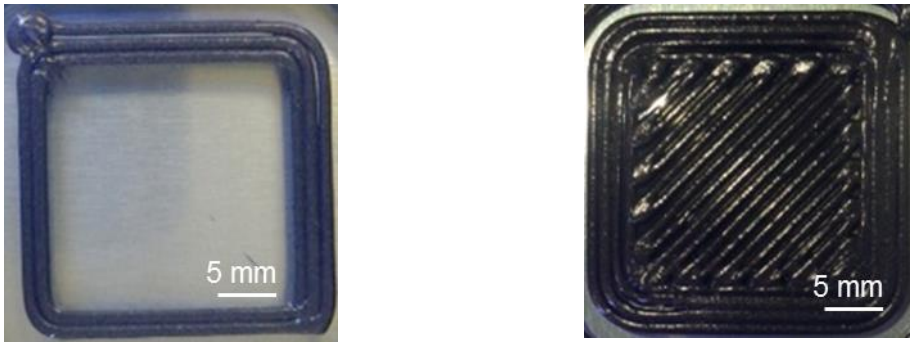

(a) (b)

Fig. A-2. Example of printing structures: (a) incorrect input parameters with unacceptable print quality and (b) correct input parameters with acceptable print quality in material extrusion / retraction stages.

Table A-1. Moving steps of extrusion motor system in both material extrusion and retraction stages.

Material	Nozzle size (mm)	Layer thickness (mm)	Moving steps in extrusion stage	Moving steps in retraction stage
Red silicone paste	0.848	0.5	10500	10500
Blue silicone paste	0.848	0.5	9500	9500
Black silicone paste	0.848	0.5	9000	9000

A-3.2. Steady-state extrusion stage

Theoretically, in this stage the print quality should be the same for the three silicone pastes if the setting parameters for all the pastes are the same. Therefore, for this experiment, the setting parameters, including the extrusion width (W_e), the layer thickness (T) and travel speed (ν), are the same for the three silicone pastes. The travel speed is 20mm/s, extrusion width is 0.9mm, and layer thickness is 0.5mm. Fig. A-3 shows the results of the print thickness and extrusion width of the three silicone pastes. The print thickness and extrusion width are all within 5% error, which is not affected by the viscosity of print materials during the printing stage.

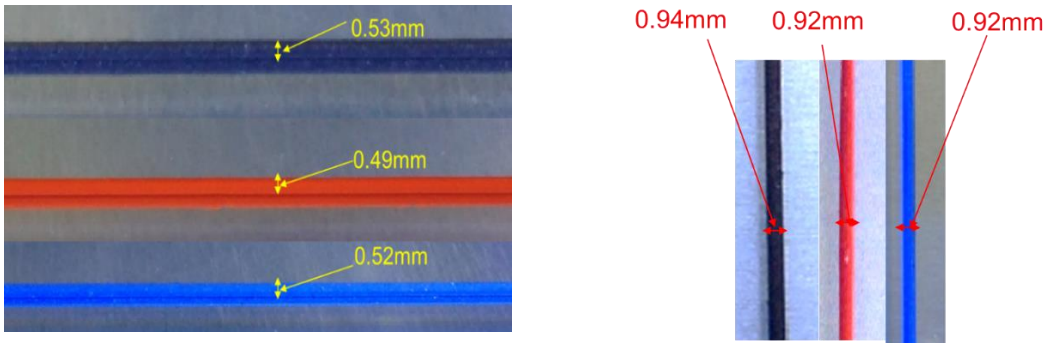

(a) (b)

Fig. A-3. Print thickness and extrusion width of the three silicone pastes under the same input parameters in steady-stage extrusion stage.

A-4. Summary

In order to evaluate and confirm the efficacy of the printing mechanisms of the Hyrel 30M extrusion-systems, three kinds of silicone pastes with different colors (red, blue and black) and viscosities were used to carry out the print quality analysis in different printing stages. In both the material extrusion and retraction stages, the material's properties (e.g., viscosity) will affect the final moving step settings of the 3D printer. This experimental result is consistent with the theoretical analysis of the extrusion mechanisms detailed in Chapter 4. In the steady-stage printing stage, the three silicone pastes can be printed with the same printing quality, and with almost the same printing thickness and width. This experimental result confirms that the material's properties will not affect the print quality in steady-state stage. Therefore, the designed structure that is printed in the steady-state stage may have a high likelihood of achieving good print quality.

APPENDIX B – G-CODE FOR HYREL SYSTEM 30M PRINTER

The Hyrel system 30M printer relies on its own G-Code system to function properly—and this code is different from that of the other open-source 3D printers. The specific G-Codes commands used for printing planar, toroid, and constant-flux inductors are explained in this appendix.

B-1. G-Code for controlling movement, position and offsets

G28	Home position setting: send X, Y, to physical home.
G90	Set absolute coordinates-calculated from the origin (0, 0 point).
G91	Set relative coordinates-calculated from the current position.
G54	Resets the current position to the specified coordinates.
G20	Set units to inches- measurements will be given in inches.
G21	Set units to millimeters- measurements will be given in millimeters.
G0	Rapid positioning move: equipment will not be printing or doing any other active work during a G0 move.
G1	Working move: during which you may be printing or doing other active work - provided an E (extrude) value is given.
G4	Pause for a set number of seconds (S) or milliseconds (P).
M0	Stop until resume command.
M203	Set G0 Speed: redesign the rate at which G0 movements are executed.

B-2. G-Code for controlling motors and extruders

T	Extruder head change: switches from the current head to T0, the head in slot 1. The four extrudes G-code value is: T0, T1, T2, T3.
E	Extruding values settings.
S	Time in second.
P	Time in millisecond.
F	Travelling speed.
M104	Set extruder temperature.
M140	Set build plate temperature, maximum setting temperature is 70^{o}C.
M221	Set flow rate: sends information to the printer about material flow.
M721	Set unprimed values: sends information to the printer about how much material to unprime when a transition from printing move to non-printing move is detected
M722	Set primed values: sends information to the printer about how much material to prime when a transition from non-printing move to printing move is detected.
M756	Set height for flow:
M30	End of program: tells the printer that this job is complete
M84	Disable motors: cut power to all motors (positioning and extruder motors), unlocking them.

REFERENCES

[1] M. Ludwig, M. Duffy, T. O. Donnell, P. McCloskey, and S. C. O. Mathuna, "PCB Integrated Inductors for Low Power DC/DC Converter," *IEEE Transactions on Power Electronics*, vol. 18, no. 4, pp. 937-945, 2003.

[2] J. M. Carrasco, L. G. Franquelo, J. T. Bialasiewicz, E. Galvan, R. C. PortilloGuisado, M. A. M. Prats *et al.*, "Power-Electronic Systems for the Grid Integration of Renewable Energy Sources: A Survey," *IEEE Transactions on Industrial Electronics*, vol. 53, no. 4, pp. 1002-1016, 2006.

[3] W. A. Tabisz, M. M. Jovanovic, and F. C. Lee, "Present and Future of Distributed Power Systems," *Seventh Annual Applied Power Electronics Conference and Exposition(APEC)*, pp. 11-18, 1992.

[4] G. Majumdar, T. Oi, T. Terashima, S. Idaka, D. Nakajima, and Y. Goto, "Review of Integration Trends in Power Electronics Systems and Devices," *9th International Conference on Integrated Power Electronics Systems*, pp. 1-10, 2016.

[5] H. Lu, Y. Guo, J. Zhu, J. Zhong, and J. Jin, "Soft Magnetic Materials for High Frequency High Power Density Transformers in Power Electronic Systems," *Academic Magazine*, 2007.

[6] A. M. Leary, P. R. Ohodnicki, and M. E. McHenry, "Soft Magnetic Materials in High-frequency, High-power Conversion Applications," *Jom*, vol. 64, no. 7, pp. 772-781, 2012.

[7] F. C. Lee, J. D. v. Wyk, D. Boroyevich, L. Guo-Quan, L. Zhenxian, and P. Barbosa, "Technology Trends Toward a System-in-a-Module in Power Electronics," *IEEE Circuits and Systems Magazine*, vol. 2, no. 4, pp. 4-22, 2002.

[8] F. C. Lee, and Q. Li, "High-Frequency Integrated Point-of-Load Converters: Overview," *IEEE Transactions on Power Electronics,* vol. 28, no. 9, pp. 4127-4136, 2013.

[9] Q. Li, "Low-profile Magnetic Integration for High-frequency Point-of-Load Converter," *Doctoral dissertation, Virginia Tech*, 2011.

[10] J. D. v. Wyk, F. C. Lee, D. Boroyevich, L. Zhenxian, and Y. Kaiwei, "A Future Approach to Integration in Power Electronics Systems," *The 29th Annual Conference of the IEEE Industrial Electronics Society,* vol. 1, pp. 1008-1019 2003.

[11] J. Popovic, and J. A. Ferreira, "An Approach to Deal with Packaging in Power Electronics," *IEEE Transactions on Power Electronics,* vol. 20, no. 3, pp. 550-557, 2005.

[12] S. Cheng, W. Chieh-An, C. Po-Chien, C. Wei-Hua, and E. Y. Chang, "All GaN-on-Si High Power Module Design and Performance Evaluation," *IEEE International Conference of Electron Devices and Solid-state Circuits,* pp. 1-2, 2013.

[13] J. He, T. Zhao, X. Jing, and N. A. O. Demerdash, "Application of Wide Bandgap Devices in Renewable Energy Systems: Benefits and Challenges," *International Conference on Renewable Energy Research and Application (ICRERA),* pp. 749-754, 2014.

[14] H. Sarnago, L. Ó, A. Mediano, and J. M. Burdío, "Design and Implementation of a High-Efficiency Multiple-Output Resonant Converter for Induction Heating Applications Featuring Wide Bandgap Devices," *IEEE Transactions on Power Electronics,* vol. 29, no. 5, pp. 2539-2549, 2014.

[15] A. Emadi, Y. J. Lee, and K. Rajashekara, “Power Electronics and Motor Drives in Electric, Hybrid Electric, and Plug-In Hybrid Electric Vehicles,” *IEEE Transactions on Industrial Electronics,* vol. 55, no. 6, pp. 2237-2245, 2008.

[16] J. W. Milligan, S. Sheppard, W. Pribble, Y. F. Wu, G. Muller, and J. W. Palmour, “SiC and GaN Wide Bandgap Device Technology Overview,” *IEEE Radar Conference,* pp. 960-964, 2007.

[17] I. Schmidt, and A. Enders, “Characterization and Concept for Optimization of Planar Spiral High Power High Frequency Coils,” *IEEE International Symposium on Electromagnetic Compatibility,* pp. 24-28, 2009.

[18] C. K. Lee, D. Xu, B. Pong, S. Kiratipongvoot, and W. M. Ng, “A Three-winding Common Mode Inductor,” *IEEE Transactions on Power Electronics,* vol. PP, no. 99, pp. 1-1, 2016.

[19] S. Walder, and X. Yuan, “Effect of Load Parasitics on the Losses and Ringing in High Switching Speed SiC MOSFET Based Power Converters,” *IEEE Energy Conversion Congress and Exposition (ECCE),* pp. 6161-6168, 2015.

[20] M. K. Kazimierczuk, “High-frequency Magnetic Components,” *John Wiley & Sons,* 2009.

[21] M. S. Rylko, K. J. Hartnett, J. G. Hayes, and M. G. Egan, “Magnetic Material Selection for High Power High Frequency Inductors in DC-DC Converters,” *Twenty-Fourth Annual IEEE Applied Power Electronics Conference and Exposition (APEC),* pp. 2043-2049, 2009.

[22] G. E. Fish, “Soft Magnetic Materials,” *Proceedings of the IEEE,* vol. 78, no. 6, pp. 947-972, 1990.

[23] J. Kim, M. Kim, F. Herrault, J. Y. Park, and M. G. Allen, "Electrodeposited Nanolaminated CoNiFe Cores for Ultracompact DC-DC Power Conversion," *IEEE Transactions on Power Electronics,* vol. 30, no. 9, pp. 5078-5087, 2015.

[24] B. Yang, Z. Wu, Z. Zou, and R. Yu, "High-performance Fe/SiO2 Soft Magnetic Composites for Low-loss and High-power Applications," *Journal of Physics D: Applied Physics,* vol. 43, no. 36, pp. 365003, 2010.

[25] S. Egelkraut, M. Maerz, and H. Ryssel, "Polymer Bonded Soft Magnetic Particles for Planar Inductive Devices," *5th International Conference on Integrated Power Electronics Systems*, pp. 1-8, 2008.

[26] J. N. Calata, G.-Q. Lu, and K. Ngo, "Soft Magnetic Alloy–Polymer Composite for High-frequency Power Electronics Application," *Journal of Electronic Materials,* vol. 43, no. 1, pp. 126-131, 2014.

[27] Y. Endo, H. Sato, T. Miyazaki, M. Yamaguchi, H. Kamada, M. Takahashi *et al.*, "Study on the Electric Performances of Planar Inductor With Fe-System Magnetic Flake Composite Integrated for SiP DC-to-DC Converter Applications," *IEEE Transactions on Magnetics*, vol. 51, no. 11, pp. 1-4, 2015.

[28] Y. Sun, C. R. Sullivan, W. Li, D. Kopp, F. Johnson, and S. T. Taylor, "Soft Magnetic Properties of Obliquely Deposited CoZrO Films," *IEEE Transactions on Magnetics,* vol. 43, no. 12, pp. 4060-4063, 2007.

[29] C. G. Oliver, "Advances in Powder Metallurgy of Soft Magnetic Materials," *IEEE Transactions on Magnetics,* vol. 31, no. 6, pp. 3982-3984, 1995.

[30] M. Persson, and P. Jansson, "Advances in Powder Metallurgy Soft Magnetic Composite Materials for Electrical Machines," *IEE Colloquium on Impact of New*

Materials on Design, pp. 4/1-4/6, 1995.

[31] D. Stoppels, "Developments in Soft Magnetic Power Ferrites," *Journal of Magnetism and Magnetic Materials,* vol. 160, pp. 323-328, 1996.

[32] H. Horie, M. Morita, and I. Arima, "Magnetic Core and Method of Producing the Same," *U.S. Patent: 4543208,* 1985.

[33] T. A. Soileau, and L. W. Speaker, "Powdered Iron Core Magnetic Devices," *U.S. Patent: 4601753,* 1986.

[34] L. Zegadi, J. J. Rousseau, B. Allard, P. Tenant, and D. Renault, "Model of Power Soft MnZn Ferrites, including Temperature Effects," *IEEE Transactions on Magnetics,* vol. 36, no. 4, pp. 2022-2032, 2000.

[35] P. J. Van der Zaag, A. Noordermeer, and P. J. Van Der Valk, "Sintered Transformer or Inductor Core of NiZn Ferrite Material," *U.S. Patent: 5871662,* 1999.

[36] A. Barba, C. Clausell, C. Felíu, M. Monzó, L. Nuño, D. Heras, and J. V. Balbastre, "Study of NiZn Ferrite Complex Permeability - Effect of Relative Density and Microstructure," *Journal of the American Ceramic Society,* vol. 87, no. 7, pp. 1314-1318, 2004.

[37] G. E. Schaller, "Ferrite Processing and Effects on Material Performance," *Fairfield, New Jersey, USA: sn págs,* pp. 87-90.

[38] R. M. German, "Powder Injection Molding," *Cambridge Univ Press,* 1990.

[39] R. Zauner, "Micro Powder Injection Moulding," *Microelectronic Engineering,* vol. 83, no. 4, pp. 1442-1444, 2006.

[40] E. Nyberg, M. Miller, K. Simmons, and K. S. Weil, "Microstructure and Mechanical Properties of Titanium Components Fabricated by a New Powder

Injection Molding Technique," *Materials Science and Engineering: C*, vol. 25, no. 3, pp. 336-342, 2005.

[41] H. C. Chau, B. Chao, X. P. Li, and T. S. Low, "Investigation of Core Loss in PM Micro-motor Made using MIM Technology," *IEEE Transactions on Magnetics*, vol. 36, no. 5, pp. 3652-3654, 2000.

[42] R. Hahn, S. Krumbholz, and H. Reichl, "Low Profile Power Inductors Based on Ferromagnetic LTCC Technology," *IEEE Electronic Components and Technology Conference*, pp. PP. 6, 2006.

[43] H. F. M. Lim, "Low Temperature Co-fired Ceramics Technology for Power Magnetics Integration," *Doctoral dissertation, Virginia Tech*, 2008.

[44] A. E. Ostfeld, I. Deckman, A. M. Gaikwad, C. M. Lochner, and A. C. Arias, "Screen Printed Passive Components for Flexible Power Electronics," *Scientific reports*, vol. 5, pp. 15959, 2015.

[45] A. Roesler, J. Schare, and C. Hettler, "Integrated Power Electronics Using a Ferrite-based Low-temperature Co-fired Ceramic Materials System," *Proceedings 60th Electronic Components and Technology Conference (ECTC)*, pp. 720-726, 2010.

[46] G. Slama, "Low-Temp Co-fired Magnetic Tape Yields High Benefits," *Power Electronics*, no. 1, pp. 30-34, 2003.

[47] D. A. Abel, "Multi-layer Transformer Apparatus and Method," *U.S. Patent 6198374*, 2001.

[48] R. Hasegawa, "Advances in Amorphous and Nanocrystalline Magnetic Materials," *Journal of Magnetism and Magnetic materials*, vol. 304, no. 2, pp. 187-191, 2006.

[49] F. Luborsky, "Amorphous Metallic Alloys," *Butterworth and Co (Publishers):*

London, UK, 1983.

[50] T. Mizoguchi, S. Hatta, H. Kato, H. Arai, K. Maeda, and N. Akutsu, "Effects of Annealing and Fabrication Conditions on the Magnetic Properties of Amorphous Ferromagnetic Alloys," *IEEE Transactions on Magnetics,* vol. 16, no. 5, pp. 1147-1149, 1980.

[51] K. Lu, "Nanocrystalline Metals Crystallized from Amorphous Solids: Nanocrystallization, Structure, and Properties," *Materials Science and Engineering: R: Reports,* vol. 16, no. 4, pp. 161-221, 1996.

[52] H. Mihara, S. Murata, and T. Morinaga, "Wire Wound Inductor," *U.S. Patent 6351203*, 2002.

[53] K. D. T. Ngo, R. P. Alley, and A. J. Yerman, "Fabrication Method for a Winding Assembly with a Large Number of Planar Layers," *IEEE Transactions on Power Electronics,* vol. 8, no. 1, pp. 55-61, 1993.

[54] B. Sun, R. Burgos, D. Boroyevich, R. Perrin, C. Buttay, B. Allard *et al.*, "Two Comparison-alternative High Temperature PCB-embedded Transformer Designs for a 2 W Gate Driver Power Supply," *IEEE Energy Conversion Congress and Exposition*, pp. 1-7, 2016.

[55] A. Pot, H. Roehm, R. v. d. Berg, and T. P. Sidiki, "New Packaging Technology Enabling Integration of Magnetics and Semiconductors in One Component," *International Conference on Electronic Packaging Technology & High Density Packaging*, pp. 18-22, 2009.

[56] R. MBK, "Review on magnetic components: Design & consideration in VHF circuit applications," *Journal of Power Electronics,* vol. 9, no. 2, pp. 180-187, 2009.

[57] H. Cui, K. D. T. Ngo, J. Moss, M. H. F. Lim, and E. Rey, “Inductor Geometry With Improved Energy Density,” *IEEE Transactions on Power Electronics,* vol. 29, no. 10, pp. 5446-5453, 2014.

[58] D. Hou, F. C. Lee, and Q. Li, “Very High Frequency IVR for Small Portable Electronics with High-Current Multi-phase 3D Integrated Magnetics,” *IEEE Transactions on Power Electronics,* vol. PP, no. 99, pp. 1-1, 2017.

[59] I. Gibson, D. W. Rosen, and B. Stucker, “Additive Manufacturing Technologies,” *Springer*, 2010.

[60] S. H. Huang, P. Liu, A. Mokasdar, and L. Hou, “Additive Manufacturing and Its Societal Impact: A Literature Review,” *The International Journal of Advanced Manufacturing Technology,* vol. 67, no. 5-8, pp. 1191-1203, 2013.

[61] N. Guo, and M. C. Leu, “Additive Manufacturing: Technology, Applications and Research Needs,” *Frontiers of Mechanical Engineering*, vol. 8, no. 3, pp. 215-243, 2013.

[62] C. C. Kai, L. K. Fai, and L. Chu-Sing, “Rapid Prototyping: Principles and Applications in Manufacturing,” *World Scientific Publishing Co., Inc.*, 2003.

[63] R. L. Sutherland, L. V. Natarajan, V. P. Tondiglia, T. J. Bunning, and W. W. Adams, “Development of Photopolymer/Liquid Crystal Composite Materials for Dynamic Hologram Applications,” *International Society for Optics and Photonics*, pp. 303-313, 1994.

[64] S. M. Peltola, F. P. Melchels, D. W. Grijpma, and M. Kellomäki, “A Review of Rapid Prototyping Techniques for Tissue Engineering Purposes,” *Annals of medicine,* vol. 40, no. 4, pp. 268-280, 2008.

[65] W. E. Frazier, “Metal Additive Manufacturing: A Review,” *Journal of Materials Engineering and Performance*, vol. 23, no. 6, pp. 1917-1928, 2014.

[66] D. Pham, and S. S. Dimov, “Rapid Manufacturing: The Technologies and Applications of Rapid Prototyping and Rapid Tooling,” *Springer Science & Business Media*, 2012.

[67] V. Bhavar, P. Kattire, V. Patil, S. Khot, K. Gujar, and R. Singh, “A Review on Powder Bed FusionTechnology of Metal Additive Manufacturing,” *4th International Conference and Exhibition on Additive Manufacturing Technologies*, pp. 1-2, 2014.

[68] H. Seitz, W. Rieder, S. Irsen, B. Leukers, and C. Tille, “Three-dimensional Printing of Porous Ceramic Scaffolds for Bone Tissue Engineering,” *Journal of Biomedical Materials Research Part B: Applied Biomaterials*, vol. 74, no. 2, pp. 782-788, 2005.

[69] M. Feygin, A. Shkolnik, M. N. Diamond, and E. Dvorskiy, “Laminated Object Manufacturing System,” *U.S. Patent: 5730817*, 1998.

[70] B. Mueller, and D. Kochan, “Laminated Object Manufacturing for Rapid Tooling and Patternmaking in Foundry Industry,” *Computers in Industry*, vol. 39, no. 1, pp. 47-53, 1999.

[71] M. Feygin, and S. S. Pak, “Laminated Object Manufacturing Apparatus and Method,” *U.S. Patent: 5876550*, 1999.

[72] B. K. Tehrani, C. Mariotti, B. S. Cook, L. Roselli, and M. M. Tentzeris, “Development, Characterization, and Processing of Thin and Thick Inkjet-printed Dielectric Films,” *Organic Electronics*, vol. 29, pp. 135-141, 2016.

[73] H. P. Le, “Progress and Trends in Ink-jet Printing Technology,” *Journal of Imaging*

Science and Technology, vol. 42, no. 1, pp. 49-62, 1998.

[74] E. Sachs, M. Cima, and J. Cornie, "Three-dimensional Printing: Rapid Tooling and Prototypes Directly from a CAD Model," *CIRP Annals-Manufacturing Technology,* vol. 39, no. 1, pp. 201-204, 1990.

[75] J.-P. Kruth, "Material Increase Manufacturing by Rapid Prototyping Techniques," *CIRP Annals-Manufacturing Technology,* vol. 40, no. 2, pp. 603-614, 1991.

[76] H. Lipson, and M. Kurman, "Fabricated: The New World of 3D Printing," *John Wiley & Sons,* 2013.

[77] L. Novakova-Marcincinova, and J. Novak-Marcincin, "Testing of the ABS Materials for Application in Fused Deposition Modeling Technology," *Applied Mechanics and Materials Trans Tech Publ,* vol. 309, pp. 133-140, 2013.

[78] B. Trimmer, J. A. Lewis, R. F. Shepherd, and H. Lipson, "3D Printing Soft Materials: What is Possible?," *Soft Robotics,* vol. 2, no. 1, pp. 3-6, 2015.

[79] T. Huang, M. S. Mason, X. Zhao, G. E. Hilmas, and M. C. Leu, "Aqueous Based Freeze-Form Extrusion Fabrication of Alumina Components (Preprint)," *DTIC Document,* 2009.

[80] N. Travitzky, A. Bonet, B. Dermeik, T. Fey, I. Filbert‐Demut, L. Schlier *et al.,* " Additive Manufacturing of Ceramic‐Based Materials," *Advanced Engineering Materials,* vol. 16, no. 6, pp. 729-754, 2014.

[81] K. Vidimče, "A Programmable Pipeline for Multi-material Fabrication," *Doctoral dissertation, Massachusetts Institute of Technology,* 2014.

[82] F. Rengier, A. Mehndiratta, H. von Tengg-Kobligk, C. M. Zechmann, R. Unterhinninghofen, H.-U. Kauczor, and F. L. Giesel, "3D Printing Based on

Imaging Data: Review of Medical Applications," *International journal of computer assisted radiology and surgery,* vol. 5, no. 4, pp. 335-341, 2010.

[83] B. C. Gross, J. L. Erkal, S. Y. Lockwood, C. Chen, and D. M. Spence, "Evaluation of 3D Printing and Its Potential Impact on Biotechnology and the Chemical Sciences," *ACS Publications,* 2014.

[84] M. Chinthavali, C. Ayers, S. Campbell, R. Wiles, and B. Ozpineci, "A 10-kW SiC inverter with a novel printed metal power module with integrated cooling using additive manufacturing," *IEEE Workshop on Wide Bandgap Power Devices and Applications (WiPDA),* pp. 48-54, 2014.

[85] M. Chinthavali, "Additive manufacturing technology for power electronics applications," *Applied Power Electronics Conference and Exposition (APEC),* 2016.

[86] W. Liang, L. Raymond, and J. Rivas, "3D-Printed air-core inductors for high-frequency power converters," *IEEE Transactions on Power Electronics,* vol. 31, no. 1, pp. 52-64, 2016.

[87] Proto pasta. "Composite PLA - Rustable Magnetic Iron," https://www.proto-pasta.com/collections/exotic-composite-pla.

[88] Y. Wang, F. Castles, and P. S. Grant, "3D printing of NiZn ferrite/ABS magnetic composites for electromagnetic devices," *MRS Proceedings,* vol. 1788, pp. mrss15-2116292, 2015.

[89] Kaijyun Jhong, Wei-Chin Huang, and W. H. Lee., "Microstructure and Magnetic Properties of Magnetic Material Fabricated by Seletive Laser Sintering," *Physics Procedia,* vol. 83, pp. 818-824, 2016.

[90] M. E. Cato, and A. B. Mullen, “FDA Issues Much Anticipated Draft Guidance on Additive Manufactured ("3D-printed") Devices,” *http://www.fdalawblog.net/fda_law_blog_hyman_phelps/*, 2016.

[91] R. Oishi, Y. Okajima, S. Noguchi, and K. Akeyoshi, “Method of Forming Patterned Transparent Electro-conductive Film on the Substrate of Liquid Crystal Display,” *U.S. Patent: 4187340*, 1980.

[92] F. P. Melchels, M. A. Domingos, T. J. Klein, J. Malda, P. J. Bartolo, and D. W. Hutmacher, “Additive Manufacturing of Tissues and Organs,” *Progress in Polymer Science*, vol. 37, no. 8, pp. 1079-1104, 2012.

[93] M. Ott, and M. Zaeh, “Multi-material Processing in Additive Manufacturing,” *Proceedings of the Solid Freeform Fabrication Symposium*, pp. 195-203, 2010.

[94] *www.hyrel3d.net*.

[95] J. A. Lewis, “Direct Ink Writing of 3D Functional Materials,” *Advanced Functional Materials*, vol. 16, no. 17, pp. 2193-2204, 2006.

[96] J. A. Lewis, “Direct-write Assembly of Ceramics from Colloidal Inks,” *Current Opinion in Solid State and Materials Science*, vol. 6, no. 3, pp. 245-250, 2002.

[97] E. B. Secor, B. Y. Ahn, T. Z. Gao, J. A. Lewis, and M. C. Hersam, “Rapid and Versatile Photonic Annealing of Graphene Inks for Flexible Printed Electronics,” *Advanced Materials*, vol. 27, no. 42, pp. 6683-6688, 2015.

[98] *http://www.nano-di.com/conductive-inks*.

[99] M. Bulger, “Advances in Powder Metal Technology for High-Performance Soft Magnetic Applications,” *Netshape Technologies, Inc.* , 2016.

[100] A. E. Jakus, S. L. Taylor, N. R. Geisendorfer, D. C. Dunand, and R. N. Shah, “

Metallic Architectures from 3D-Printed Powder-Based Liquid Inks," *Advanced Functional Materials,* vol. 25, no. 45, pp. 6985-6995, 2015.

[101] D. A. Roberson, R. B. Wicker, L. E. Murr, K. Church, and E. MacDonald, "Microstructural and Process Characterization of Conductive Traces Printed from Ag Particulate Inks," *Materials,* vol. 4, no. 6, pp. 963-979, 2011.

[102] G.-Q. Lu, G. Lei, and J. Calata, "Nanoscale Metal Paste for Interconnect and Method of Use," *U.S. Patent 8257795*, 2012.

[103] *http://www.gwent.org/home.html*.

[104] *http://www.voxel8.co/*.

[105] J. G. Bai, Z. Z. Zhang, J. N. Calata, and G.-Q. Lu, "Low-temperature sintered nanoscale silver as a novel semiconductor device-metallized substrate interconnect material," *IEEE Transactions on components and packaging technologies,* vol. 29, no. 3, pp. 589-593, 2006.

[106] P. M. Raj, H. Sharma, G. P. Reddy, N. Altunyurt, M. Swaminathan, R. Tummala *et al.*, "Novel Nanomagnetic Materials for High-frequency RF Applications," *Electronic Components and Technology Conference (ECTC),* pp. 1244-1249, 2011.

[107] G. Roberts, A. Davidson, S. Gair, and J. Hajto, "An overview of the Powder Processing of Soft Magnetic Composites," *Engineering Science and Education Journal,* vol. 10, no. 6, pp. 237-240, 2001.

[108] H. Shokrollahi, and K. Janghorban, "Soft Magnetic Composite Materials (SMCs)," *Journal of Materials Processing Technology*, vol. 189, no. 1, pp. 1-12, 2007.

[109] C.-W. Chen, "Magnetism and Metallurgy of Soft Magnetic Materials," *Courier Corporation,* 2013.

[110] Y. S. Kang, S. Risbud, J. F. Rabolt, and P. Stroeve, "Synthesis and Characterization of Nanometer-size Fe3O4 and γ-Fe2O3 Particles," *Chemistry of Materials,* vol. 8, no. 9, pp. 2209-2211, 1996.

[111] P. Jansson, and L.-Å. Larsson, "Phosphate Coated Iron Powder and Method for the Manufacturing Thereof," *U.S. Patent: 6348265,* 2002.

[112] R. He, X. You, J. Shao, F. Gao, B. Pan, and D. Cui, "Core/shell Fluorescent Magnetic Silica-coated Composite Nanoparticles for Bioconjugation," *Nanotechnology,* vol. 18, no. 31, pp. 315601, 2007.

[113] J. M. BRANDT, "Rheological and Abrasion Resistant Properties of Transparent Polymer/silicate Nanocomposite Coatings," *Doctoral dissertation, University of Florida,* 2005.

[114] M. Anhalt, and B. Weidenfeller, "Magnetic Properties of Polymer Bonded Soft Magnetic Particles for Various Filler Fractions," *Journal of applied physics,* vol. 101, no. 2, pp. 023907, 2007.

[115] H. Song, "Soft Magnetic Composites for High Frequency Applications," *Doctoral dissertation, Oregon State University,* 2015.

[116] S. Hariharan, and J. Gass, "Superparamagnetism and Magneto-caloric Effect (MCE) in Functional Magnetic Nanostructures," *Rev. Adv. Mater. Sci,* vol. 10, no. 5, pp. 398-402, 2005.

[117] A. Taghvaei, H. Shokrollahi, M. Ghaffari, and K. Janghorban, "Influence of Particle Size and Compaction Pressure on the Magnetic Properties of Iron-phenolic Soft Magnetic Composites," *Journal of Physics and Chemistry of Solids,* vol. 71, no. 1, pp. 7-11, 2010.

[118] T. Hanemann, and D. V. Szabó, "Polymer-nanoparticle Composites: from Synthesis to Modern Applications," *Materials,* vol. 3, no. 6, pp. 3468-3517, 2010.

[119] Y. Pittini-Yamada, E. Périgo, Y. De Hazan, and S. Nakahara, "Permeability of Hybrid Soft Magnetic Composites," *Acta Materialia,* vol. 59, no. 11, pp. 4291-4302, 2011.

[120] H. S. Göktürk, T. J. Fiske, and D. M. Kalyon, "Effects of Particle Shape and Size Distributions on the Electrical and Magnetic Properties of Nickel/Polyethylene Composites," *Journal of applied polymer science,* vol. 50, no. 11, pp. 1891-1901, 1993.

[121] Z. Hashin, and S. Shtrikman, "A Variational Approach to the Theory of the Effective Magnetic Permeability of Multiphase Materials," *Journal of applied Physics,* vol. 33, no. 10, pp. 3125-3131, 1962.

[122] T. J. Fiske, H. Gokturk, and D. M. Kalyon, "Enhancement of The Relative Magnetic Permeability of Polymeric Composites with Hybrid Particulate Fillers," *Journal of applied polymer science,* vol. 65, no. 7, pp. 1371-1377, 1997.

[123] D. Burdeaux, P. Townsend, J. Carr, and P. Garrou, "Benzocyclobutene (BCB) Dielectrics for the Fabrication of High Density, Thin Film Multichip Modules," *Journal of Electronic Materials,* vol. 19, no. 12, pp. 1357-1366, 1990.

[124] J. J. Licari, "Coating Materials for Electronic Applications: Polymers, Processing, Reliability, Testing," *William Andrew,* 2003.

[125] T. Stokich, W. Lee, and R. Peters, "Real-time FT-IR Studies of the Reaction Kinetics for the Polymerization of Divinyl Siloxane bis-Benzocyclobutene Monomers," *MRS Proceedings,* vol. 227, pp. 103, 1991.

[126] W. Sun, “Microstructure-based FE Modeling and Measurements of Magnetic Properties of Polymer Matrix-Metal Composites,” Virginia Tech, 2017.

[127] K. H. J. Buschow, “Handbook of Magnetic Materials,” *Elsevier,* vol. 15, 2003.

[128] Metglas®, “2705M Magnetic Alloy Application Note,” http://www.metglas.com.

[129] A. Brockmeyer, “Experimental Evaluation of the Influence of DC-Premagnetization on the Properties of Power Electronic Ferrites,” *Eleventh Annual Applied Power Electronics Conference and Exposition (APEC),* vol. 1, pp. 454-460 1996.

[130] Y. Han, and Y. F. Liu, “A Practical Transformer Core Loss Measurement Scheme for High-Frequency Power Converter,” *IEEE Transactions on Industrial Electronics,* vol. 55, no. 2, pp. 941-948, 2008.

[131] V. J. Thottuvelil, T. G. Wilson, and H. A. Owen, "High-frequency Measurement Techniques for Magnetic Cores," *IEEE Power Electronics Specialists Conference*, 1985, pp. 412-425.

[132] V. C. Valchev, and A. Van den Bossche, “Inductors and Transformers for Power Electronics,” 2005.

[133] F. D. Tan, J. L. Vollin, and S. M. Cuk, “A Practical Approach for Magnetic Core-loss Characterization,” *IEEE Transactions on Power Electronics,* vol. 10, no. 2, pp. 124-130, 1995.

[134] Z. Zhong, Q. Wang, L. Tao, L. Jin, X. Tang, F. Bai, and H. Zhang, “Permeability Dispersion and Magnetic Loss of Fe/NixZn1-xFe2O4 Soft Magnetic Composites,” *IEEE Transactions on Magnetics,* vol. 48, no. 11, pp. 3622-3625, 2012.

[135] A. J. Hanson, J. A. Belk, S. Lim, C. R. Sullivan, and D. J. Perreault, “Measurements

and Performance Factor Comparisons of Magnetic Materials at High Frequency," *IEEE Transactions on Power Electronics,* vol. 31, no. 11, pp. 7909-7925, 2016.

[136] M. Mu, "High Frequency Magnetic Core Loss Study," *Doctoral dissertation, Virginia Tech*, 2013.

[137] M. Mu, F. C. Lee, Q. Li, D. Gilham, and K. D. T. Ngo, "A High Frequency Core Loss Measurement Method for Arbitrary Excitations," *Twenty-Sixth Annual Applied Power Electronics Conference and Exposition (APEC)*, pp. 157-162, 2011.

[138] D. Hou, M. Mu, F. C. Lee, and Q. Li, "New High-Frequency Core Loss Measurement Method With Partial Cancellation Concept," *IEEE Transactions on Power Electronics,* vol. 32, no. 4, pp. 2987-2994, 2017.

[139] J. Adams, "Particle Size and Shape Effects in Materials Science: Examples from Polymer and Paper Systems," *Clay Minerals*, vol. 28, no. 4, pp. 509-530, 1993.

[140] Y. Yan, K. D. Ngo, D. Hou, M. Mu, Y. Mei, and G.-Q. Lu, "Effect of Sintering Temperature on Magnetic Core-loss Properties of a NiCuZn Ferrite for High-frequency Power Converters," *Journal of Electronic Materials,* vol. 44, no. 10, pp. 3788, 2015.

[141] R. Ramprasad, P. Zurcher, M. Petras, M. Miller, and P. Renaud, "Fundamental Limits of Soft Magnetic Particle Composites for High Frequency Applications," *physica status solidi (b),* vol. 233, no. 1, pp. 31-38, 2002.

[142] P. Kollár, Z. Birčáková, J. Füzer, R. Bureš, and M. Fáberová, "Power Loss Separation in Fe-based Composite materials," *Journal of Magnetism and Magnetic Materials,* vol. 327, pp. 146-150, 2013.

[143] T. D. Shen, U. Harms, and R. B. Schwarz, "Bulk Fe-based Metallic Glass with

Extremely Soft Ferromagnetic Properties," *Metastable and Nanocrystalline Materials,* vol. 13, pp. 441-446, 2002.

[144] H. Chiriac, N. Lupu, and M. Tibu, "Design and Preparation of New Fe-based Bulk Amorphous Alloys Toroids," *IEEE transactions on magnetics,* vol. 39, no. 5, pp. 3040-3042, 2003.

[145] A. Taghvaei, H. Shokrollahi, K. Janghorban, and H. Abiri, "Eddy Current and Total Power Loss Separation in the Iron–Phosphate–Polyepoxy Soft Magnetic Composites," *Materials & Design,* vol. 30, no. 10, pp. 3989-3995, 2009.

[146] A. H. Taghvaei, A. Ebrahimi, K. Gheisari, and K. Janghorban, "Analysis of the Magnetic Losses in Iron-based Soft Magnetic Composites with MgO Insulation Produced by Sol–gel Method," *Journal of Magnetism and Magnetic Materials,* vol. 322, no. 23, pp. 3748-3754, 2010.

[147] M. Li, L. Tang, R. G. Landers, and M. C. Leu, "Extrusion Process Modeling for Aqueous-Based Ceramic Pastes—Part 1: Constitutive Model," *Journal of Manufacturing Science and Engineering,* vol. 135, no. 5, pp. 051008, 2013.

[148] M. Li, L. Tang, R. G. Landers, and M. C. Leu, "Extrusion Process Modeling for Aqueous-Based Ceramic Pastes—Part 2: Experimental Verification," *Journal of Manufacturing Science and Engineering,* vol. 135, no. 5, pp. 051009, 2013.

[149] L. Jianping, and D. Guiling, "Technology Development and Basic Theory Study of Fluid Dispensing-A Review," *IEEE Proceeding of the Sixth IEEE CPMT Conference on High Density Microsystem Design and Packaging and Component Failure Analysis.* , pp. 198-205, 2004.

[150] W. McEwen, "Application of Poiseuille's Law to Aqueous Outflow," *AMA*

archives of ophthalmology, vol. 60, no. 2, pp. 290-294, 1958.

[151] M. S. Mason, T. Huang, R. G. Landers, M. C. Leu, and G. E. Hilmas, "Freeform Extrusion of High Solids Loading Ceramic Slurries, Part I: Extrusion Process Modeling," *17th Annual Solid Freeform Fabrication Symposium, Austin, TX, Aug*, pp. 14-16, 2006.

[152] Y. Zheng, Y. Wang, and G. Xia, "Amorphous Soft Magnetic Composite-cores with Various Orientations of the Powder-flakes," *Journal of Magnetism and Magnetic Materials*, vol. 396, pp. 97-101, 2015.

[153] T. Kumpulainen, J. Pekkanen, J. Valkama, J. Laakso, R. Tuokko, and M. Mäntysalo, "Low Temperature Nanoparticle Sintering with Continuous Wave and Pulse Lasers," *Optics & Laser Technology*, vol. 43, no. 3, pp. 570-576, 2011.